

Aalto University
School of Science
Degree Programme in Industrial Engineering and Management
Degree Programme in Engineering Physics and Mathematics

Arttu Tuomiranta

**PERFORMANCE MODELLING OF
PHOTOVOLTAIC POWER STATIONS FOR
AN INTERACTIVE SOLAR ENERGY ATLAS
OF THE ARABIAN PENINSULA**

Master's Thesis

Abu Dhabi, November 21, 2014

Supervisor: Professor Peter Lund

Instructor: Dr. Hosni Ghedira

Author:

Arttu Tuomiranta, M.Sc.

Subject of the thesis:

Performance Modelling of Photovoltaic Power Stations for an Interactive Solar Energy Atlas of the Arabian Peninsula

Number of pages:

116

Date:

November 21, 2014

Library location:

TU

Professorship:

Energy Sciences

Code of professorship:

Tfy-56

Supervisor:

Peter Lund, D.Sc.(Tech.)

Instructors:

Hosni Ghedira, Ph.D.

Research Center for Renewable Energy Mapping and Assessment (ReCREMA) at Masdar Institute, Abu Dhabi is working towards becoming a centre of know-how in solar energy development under hot desert climates. In accordance with this mission, this thesis study was initiated with an objective to develop a performance model for solar photovoltaic power stations specifically operating in the Arabian Peninsula. The thesis study is tightly linked to ReCREMA's plans to extend their current web-based solar resource mapping tool to solar technology assessment, for which reason the model's web integrability is important.

In order to meet the project's objective, an extensive review of the relevant physics and available modelling tools was conducted. Special attention was paid to the dependence of PV performance on the phenomena typical of hot desert climates. The optimal thermal model was found through cross-validation based on test field data collected in Masdar City. Additionally, the particular requirements related to web integration were investigated.

The primary objective of the thesis project was met by developing a PV performance simulator that is optimised for ReCREMA's purposes. Calibration potential and computation speed were some of the main factors behind the model selection.

Keywords:

photovoltaic, modelling, desert, WebGIS

Publishing language:

English

Tekijä: Arttu Tuomiranta, M.Sc.		
Työn nimi: Aurinkosähkövoimalaitosten tuotannon mallintaminen vuorovaikutteisessa Arabian niemimaan aurinkoenergiakartastossa		
Sivumäärä: 116	Päiväys: 21.11.2014	Työn sijainti: TU
Professuuri: Energiatieteet		Koodi: Tfy-56
Työn valvoja: Peter Lund, TkT		
Työn ohjaaja: Hosni Ghedira, Ph.D.		
<p> Masdar Institutessa, Abu Dhabissa toimiva Research Center for Renewable Energy Mapping and Assessment (ReCREMA) pyrkii kuumissa aavikko-olosuhteissa tuotettuun aurinkoenergiaan liittyvän osaamisen keskuiseksi. Tämä diplomityöprojekti aloitettiin ReCREMAN tahtotilan tukemana tavoitteenaan aurinkosähkövoimalaitosten tuotannon mallinnustyökalun kehittäminen huomioiden etenkin Arabian niemimaan erityispiirteet. Projekti on vahvasti yhteydessä ReCREMAN suunnitelmiin laajentaa keskuksen aurinkoenergiakartaston toiminnallisuus aurinkoenergiateknologioiden potentiaalin arviointiin. Tästä syystä kehitettävän mallinnustyökalun verkkoyhteensopivuus on tärkeää. </p> <p> Projektiin liittyvä kattava kirjallisuuskatsaus keskittyi keskeisiin fysiikan teorioihin ja kirjallisuudesta löytyviin mallinnustyökaluihin. Aurinkosähkövoimalaitosten tuotannon riippuvuus aavikko-olosuhteissa oli erityishuomion kohteena. Ristiinvalidoimalla haarukoitiin optimaalinen lämpötilamalli eri aurinkopaneelimateriaaleille Masdar Cityssä, Abu Dhabissa. Lisäksi verkkointegrointiin liittyviä erityisvaatimuksia tutkittiin. </p> <p> Diplomityöprojektin päätavoite täytettiin kehittämällä aurinkosähkövoimalaitosten tuotannon mallinnustyökalu, joka on optimoitu ReCREMAN tarpeiden näkökulmasta. Laskenta-aika ja mahdollisuus kalibrointiin olivat tärkeimpiä tekijöitä mallien sopivuuden arvioinnissa. </p>		
Asiasanat: aurinkosähkö, mallinnus, aavikko, WebGIS		Julkaisukieli: englanti

Contents

Acknowledgements	4
Nomenclature	5
1. Introduction	8
2. Photovoltaic Power Production	9
2.1 Photovoltaic Effect	9
2.2 Photovoltaic Power Stations	10
2.2.1 Solar Cell	11
2.2.2 Solar Array	14
2.2.3 Electric Power Converter	16
2.3 Determinants of Output	17
2.3.1 Irradiance	19
2.3.2 Optical Losses	21
2.3.3 Thermalisation	25
2.3.4 Recombination	26
2.3.5 Parasitic Losses	30
3. Performance Modelling of Photovoltaic Power Stations	36
3.1 Optical Modelling	36
3.1.1 Irradiance Transposition	36
3.1.2 Angular Reflection and Soiling Losses	40
3.2 Spectral Modelling	41
3.3 Thermal Modelling	42
Validation of Thermal Models for Photovoltaic Cells under Hot Desert Climates	43
3.4 Electrical Modelling	48
3.4.1 Power Generation	48
3.4.2 Power Transmission	52
3.4.3 Power Conversion	52
4. Proposed Performance Model	54
4.1 PV Performance Assessment in WebGIS Environment	54
4.2 Algorithmic Architecture and Scope	55
4.3 System Configuration	57
4.4 Optical Model	63
4.5 Spectral Model	64

4.6	Thermal Model	64
4.7	Electrical Model	65
4.8	Output Processing	65
5.	Case Study – PV Performance in the Arabian Peninsula	67
5.1	Spatiotemporal Input Variables.....	67
5.2	Assessment of PV Performance.....	73
5.2.1	Effective Irradiance.....	73
5.2.2	Effect of PV Material.....	76
5.2.3	Effect of Mounting Method.....	83
5.2.4	Effect of Capacity.....	98
5.2.5	Effect of Loading Ratio.....	101
5.3	Discussion	103
6.	Conclusion	104
	Bibliography.....	105

Acknowledgements

First of all, I want to thank my thesis instructor Dr. Hosni Ghedira and the Research Center for Renewable Energy Mapping and Assessment at Masdar Institute for giving me the opportunity to simultaneously pursue my thesis research while working for the centre and for all the support and flexibility during the thesis writing process.

I also want to thank my thesis supervisor Dr. Peter Lund for the flexibility regarding the thesis scheduling and the valuable advice during the course of the project.

Of course, I would also like to thank Mrs. Anne-Mari Johansson who has been of tremendous help to me since my junior year.

Nomenclature

Latin symbols

A	surface area
A_{act}	module active area
A_{ap}	module aperture area
A_{mod}	module total surface area
A_{ofc}	surface area of opaque front contact
C	heat capacity
CF	capacity factor
E (vector)	electric field
E (scalar)	energy
E_g	band gap energy
E_{g,0}	band gap energy at absolute zero
e	elementary charge
FF	fill factor
h	Planck constant
ħ	reduced Planck constant
I	electric current
I₀	reverse saturation current
I_{0,1}	reverse saturation current due to interband recombination
I_{0,2}	reverse saturation current due to SRH recombination in SCR
I_d	diode current
I_{dc}	DC input current to inverter
I_{dc,max}	maximum DC input current to inverter
I_{mpp}	maximum power point current
I_{ph}	photocurrent
I_{rec}	recombination current
I_{sc}	short circuit current
I_{th}	thermal generation current
J	electric current density
k	Boltzmann constant
N	number/concentration
N_c	effective density of states in conduction band
N_s	number of cells in series
N_v	effective density of states in valence band
n_e	concentration of electrons in the conduction band
n_h	concentration of holes in the valence band
n_d	diode ideality factor
P	power
P_{ac}	AC output power
P_{ac,0}	Inverter power rating
P_{dc}	DC input power to inverter
P_{dc,0}	DC input power to inverter operating at P _{ac,0}
P_{il}	Power lost in power conversion
P_{stc}	plant capacity
P_{tl}	Power lost in transmission
q	electric charge
q	heat transfer rate
q_{conv}	convective heat transfer rate
q_{rad}	radiant heat transfer rate

PR	performance ratio
R	resistance
R_p	shunt resistance i.e. parallel resistance
R_s	series resistance
R	transposition factor
R_d	diffuse transposition factor
R_r	ground-reflected transposition factor
r	array-to-inverter loading ratio
T	temperature
T_a	ambient air temperature
T_c	cell temperature
T_{ls}	land surface temperature
T_S	temperature of the Sun
T_{sky}	sky temperature
t	time
v	velocity
v_w	wind velocity
V	voltage
V_{dc}	DC input voltage to inverter
V_{dc,0}	DC input voltage to inverter operating at P _{ac,0}
V_{dc,max}	maximum DC input voltage to inverter
V_{oc}	open circuit voltage
W	irradiance
W_{abs}	irradiance absorbed by a PV material
W_{b,n}	direct normal irradiance
W_{d,h}	diffuse normal irradiance
W_{eff}	effective irradiance
W_{g,h}	direct normal irradiance
W_{poa}	plane of array irradiance
W_{toa,n}	direct normal irradiance on the top of the atmosphere
Y	yield

Greek symbols

α	temperature coefficient
α_{isc}	temperature coefficient of short-circuit current
β	tilt angle with respect to the horizontal
β_{axis}	tilt angle of an axis with respect to the horizontal
ε	emissivity
ε_{ls}	land surface emissivity
ε_{mod}	module surface emissivity
ε_{sky}	sky emissivity
η	efficiency
η_c	efficiency of a Carnot cycle
η_c	conversion efficiency of a solar cell
η_{emit}	photon emission efficiency
θ	angle of incidence
θ_z	solar zenith angle
μ	chemical energy
μ_{ehp}	free energy per an electron-hole pair
ν	frequency
ρ	albedo

Φ	flux
Φ_{rad}	incident radiant flux
φ	potential difference
$\Delta\varphi$	built-in potential of a solar cell
φ	azimuth angle
φ_s	solar azimuth angle
ω	angular frequency
ω	angle of rotation
ω_{axis}	angle of axis rotation
Ω	solid angle
Ω_{abs}	solid angle of absorption

Subscripts

0	absolute zero
0	inverter rating conditions
0	thermal equilibrium
1	interband recombination
2	SRH recombination in SCR
a	ambient air
abs	absorption/absorbed
ac	alternating current
act	photoactive
ap	aperture
axis	axis
b	beam
C	Carnot cycle
c	conduction band
c	solar cell
conv	convective
d	diffuse
d	diode
e	electron
eff	effective
ehp	electron-hole pair
emit	emission
g	band gap
g	global
h	hole
h	horizontal
il	inverter losses
ls	land surface
max	maximum
mod	solar module
mpp	maximum power point
n	normal to beam propagation
oc	open circuit
ofc	opaque front contact
out	output
p	in parallel
ph	photogenerated
poa	incident on the plane of an array
r	reflected
rad	radiant
rec	recombination
rot	rotation

S	the Sun
s	in series
sky	sky
sc	short circuit
stc	standard test conditions
th	thermally generated
tl	transmission losses
toa	top of atmosphere
v	valence band
w	wind
z	zenith

Abbreviations

AC	alternating current
AM	air mass
AOD	aerosol optical depth
ARC	anti-reflection coating
a-Si	amorphous silicon
a-Si/μc-Si	micromorphous silicon
BOS	balance of system
CF	capacity factor
CIGS	copper indium gallium diselenide
CIS	copper indium diselenide
c-Si	monocrystalline silicon
DC	direct current
DHI	diffuse horizontal irradiance
DNI	direct normal irradiance
EHP	electron-hole pair
EVA	ethylene-vinyl acetate
FCA	free carrier absorption
FLH	full load-equivalent operating hours
FF	fill factor
GHI	global horizontal irradiance
GIS	geographic information system
HIT	heterojunction with intrinsic thin layer
IAM	incidence angle modifier
I-V	current-voltage
LFM	Loss Factor Model
mc-Si	polycrystalline silicon
MD	manufacturer data
MPP	maximum power point
NREL	National Renewable Energy Laboratory
OFC	opaque front contact
POA	plane of array
PR	performance ratio
PV	solar photovoltaic
rBIAS	relative mean bias error
ReCREMA	Research Center for Renewable Energy Mapping and Assessment
RMSE	root mean square error
rRMSE	relative root mean square error
SAPM	Sandia PV Array Performance Model
SCR	space charge region
SG2	Solar Geometry 2 algorithm
SIPM	Sandia Inverter Performance Model

SNL	Sandia National Laboratories
SRH	Shockley-Read-Hall
STC	standard test conditions
TCO	transparent conducting oxide
TPFT	third-party field test
μc-Si	microcrystalline silicon

1. Introduction

Solar power does not have a long history in the United Arab Emirates (UAE) or Arabian Peninsula in general. The region's first utility-scale PV power station was inaugurated in Masdar City, Abu Dhabi, UAE in 2009, after which the expansion of the total capacity has been modest. Since the utilisation of the region's immense solar potential largely depends on political will, awareness creation and information dissemination play the key role in kicking off the growth. In 2013, the Research Center for Renewable Energy Mapping and Assessment at Masdar Institute (ReCREMA) initiated the development of the centre's own PV performance simulation tool for this purpose – building and sharing knowledge about solar photovoltaic (PV) performance under hot desert climates. Since its inception, the PV performance simulator has been an essential part of the UAE Solar Atlas project. The main objective of the centre's PV performance assessment efforts is to develop a web-based geographic information system (WebGIS) portal that dynamically maps the performance of solar power plants based on a set of user-defined parameters for plant design and spatiotemporal scope. The portal is the first of its kind worldwide and is hoped to help the region's nascent PV market grow.

The development of ReCREMA's PV performance simulation tool has been partially carried out in the context of this Master's thesis. The primary objective of this thesis study is practical: the development of a PV performance model that is particularly well suited to the WebGIS environment as well as the main region of interest, the Arabian Peninsula. The primary objective involves the following research questions:

1. What are the particularities of the Arabian Peninsula from the viewpoint of PV performance?
2. What are the particularities of the WebGIS environment from the viewpoint of PV performance modelling?
3. What PV performance models are the most suitable for the simulator considering the primary objective of the project?

The modelling project focuses on the technical performance simulation of established commercially available PV technologies and, therefore, does not aim to address novel technological advances of any sort. Due to the technical perspective, economic factors are not taken into consideration at this stage, either. This model is also limited only to utility-scale power plants with central power conditioning. Hence, neither rooftop PV systems nor string inverters or other decentralised power converters are considered. The geographical scope of the study is the Arabian Peninsula and therefore, the analysis of hot desert conditions from the PV performance point of view is emphasised.

A comprehensive overview of PV power generation is presented in chapter 2. The chapter's particular focus lies on the loss processes involved in PV power generation. The chapter also aims to answer the first research question by discussing the impact of the ambient conditions typical of hot desert climates. The third chapter reviews the most common PV performance modelling tools and, thereby, paves the way for the model development-related discussion in chapter 4. Chapter 4 addresses both the second and third research question. Finally, in chapter 5, the sensitivity of different input variables is tested by inputting actual data to the model developed. Unfortunately, due to the lack of measured PV performance data, the validation of the model is not possible in the context of this thesis.

2. Photovoltaic Power Production

This chapter lays the foundation of the discussion in the subsequent chapters by explaining the rudiments of the direct conversion of sunlight into electricity. The first section briefly discusses the photovoltaic effect, which is the fundamental phenomenon for the operation of solar cells. How the effect is exploited in modern PV power production is explained in the second section. The third section focuses on the determinants of the power output of an operational PV power station.

2.1 Photovoltaic Effect

The photovoltaic effect is the basis of the direct conversion of light into electricity in that it generates mobile electron-hole pairs (EHP) in a condensed, photovoltaic material exposed to radiant energy. In order for the effect to occur, the radiation quanta i.e. photons interacting with the material need to have energies higher than the band gap of the material E_g , which is dependent on the crystal structure and the temperature of the material. In this case, it is assumed that the absorption of photons leading to EHP generation i.e. interband absorption is a step function over photon energy and the absorber is discrete in that the thicknesses of its energy levels (valence and conduction bands) are indefinitely narrow i.e. 0 eV. This simplified approach has been illustrated in Figure 2-1. In Figure 2-1 (a), photons are not absorbed due to their low energy but they are reflected off or transmitted through the material. In a situation where the photon energy is greater than or equal to E_g (Figure 2-1 b & c), absorption is possible. When a photon is absorbed, its energy is transferred to a valence electron, which now has a sufficient energy to cross the band gap to the conduction band. These excited electrons are no longer bound in covalent bonds, which makes it possible for them to diffuse freely in the conduction band. Therefore, in the presence of an electrochemical potential difference in the material, electric energy is generated. The difference between E_g and the photon energy is converted into vibration quanta i.e. phonons within the material. In other words, the remaining energy is dissipated as heat.

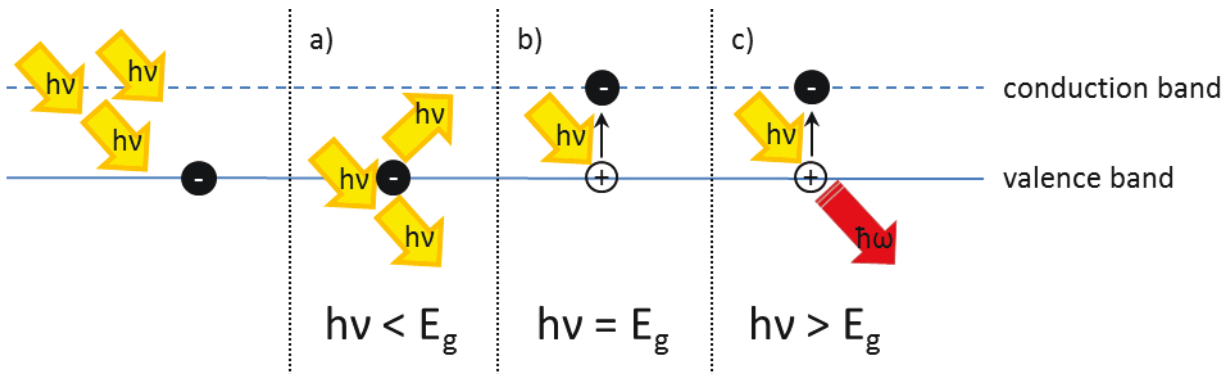


Figure 2-1. Photon-electron interaction: a) photon energy $h\nu$ less than the band gap E_g , absorption not possible b) photon energy equal to E_g , absorption possible c) photon energy higher than E_g , absorption possible with the remainder converting into phonon energy $\hbar\omega$.

In reality, the absorption of sunlight does not follow a step function but it is a continuous function over photon energy. In other words, the probability of the interband absorption of sub-band gap photons cannot be exactly zero (uncertainty principle) and, on the other hand, photons colliding with electrons are not necessarily absorbed even with energy levels higher than E_g . Interband absorption and the consequent charge carrier generation only occur in collisions that allow for the conservation of energy and crystal momentum, as in Figure 2-1 (b & c). The step function approach is a reasonably good approximation with materials with a direct band gap. The electrons of such a material have equivalent crystal momenta in both

valence and conduction bands, whereas the opposite is true for materials with indirect band gaps. Since photons do not have crystal momentum, absorption in indirect band gap materials requires a three-particle collision involving a phonon in addition to an electron and a photon. Furthermore, in order for absorption to occur, the momentum of the phonon involved needs to equal to the momentum difference between the valence band and the conduction band. Thus, absorption is less probable in the case of an indirect band gap than in that of a direct one. The most widely used photovoltaic material, crystalline silicon, has an indirect band gap. The band gap types and levels of the seven photovoltaic materials considered in this study are presented in Table 2-1.

Table 2-1. Characteristics of the photovoltaic materials under consideration.

Photovoltaic material & junction structure	Typical cell structure	Band gap type	Typical E_g at 300 K
c-Si, monocrystalline silicon Si:P/Si:B	wafer	indirect	1.12 eV (Sze and Ng, 2006, p. 179)
mc-Si, polycrystalline silicon Si:P/Si:B	wafer	indirect	1.12 eV (Sze and Ng, 2006, p. 179)
a-Si, amorphous silicon Si:H/B/Si:H/Si:H:P	thin-film	direct	1.72 eV/1.67 eV (Tucci et al., 2011, p. 337)
a-Si/ μ c-Si, micromorphous silicon SiC:H/B/Si:H/Si:H:P/Si:H/B/Si:H/Si:H:P	thin-film	direct /indirect	2 eV/1.72 eV/1.67 eV/1.12 eV (Tucci et al., 2011, p. 337)
CdTe CdS/CdTe	thin-film	direct	2.42 eV/1.45 eV (Chu and Chu, 1995)
CIS ZnO:Al/CdS/CuInSe ₂	thin-film	direct	3.2 eV/2.42 eV/1.04 eV (Chu and Chu, 1995)
CIGS ZnO:Al/CdS/Cu(In,Ga)Se ₂	thin-film	direct	3.2 eV/2.42 eV/1.04-1.68 eV (Chu and Chu, 1995; Contreras et al., 2003)

It follows from the assumption of discrete absorber energy levels that interband absorption is the only possible way photons can be absorbed in a photovoltaic material. In actual fact however, the energy levels are degenerate within a quantum system such as the conduction band of the material. This means that the band actually consists of several states, which can be occupied or unoccupied. Therefore, absorption may also occur through the excitation of a conduction electron from an occupied state of the conduction band to a higher unoccupied one in a so called n-type material (see section 2.2.1). Analogously, the same phenomenon may happen among holes in the valence band of a p-type material (see section 2.2.1). The phenomenon is known as free carrier absorption (FCA). It is a function of the charge carrier concentration of an absorber material i.e. the concentration of electrons in the material's conduction band (n-type) or that of holes in the valence band (p-type). In addition, FCA has an inverse power law dependence on photon energy. This sort of absorption does not produce another free EHP and therefore, it does not directly contribute to the output of a cell. However, when an excited electron descends to a lower energy state through lattice interaction in so called phonon-assisted relaxation, heat is dissipated in the lattice thus increasing the temperature of the material.

2.2 Photovoltaic Power Stations

This section describes a typical structure of a utility-scale PV system with a focus on components influencing performance in normal operating conditions. In addition to power generation components, the form involved in the balance of system (BOS) such as mounting, electrical transmission, and power conditioning is discussed.

2.2.1 Solar Cell

Today, the most common device configuration applied in PV electricity generation is a solar cell comprising a p-n junction of two different semiconductor materials, each connected to a metal contact. Throughout this thesis, the term solar cell will be used to refer to a device based on such a junction. As can be seen from Table 2-1, there are two main categories of solar cells: crystalline silicon wafer-based and thin-film devices. The fabrication processes of the two cell types significantly differ from each other. While the former are based on wafers cut from ingots of bulk silicon, the latter is fabricated by means of thin-film deposition on a glass substrate. Both cell types are normally equipped with an anti-reflection coating (ARC) that is deposited on the textured top semiconductor layer of a cell. Charge carriers are usually transported out of a wafer-based solar cell through a grid of thin metal wires on the top of the cell and a full-area metal contact on the rear surface. In the case of thin-film cells, also the ohmic contacts are usually deposited as thin films on the substrate and therefore, the top conducting film needs to be transparent and is normally made up of a transparent conducting oxide (TCO).

Through doping i.e. introducing impurities into a semiconductor material, the charge carrier concentration of the material can be modified. A p-n junction is an interface between two types of a semiconductor: one doped with an impurity adding to the concentration of holes (p) and the other with an impurity adding to that of electrons (n). In case a junction consists of two materials with distinct band gaps, it is called a heterojunction, whereas a junction with a homogenous E_g is known as a homojunction. In most cell designs, the n-type material is placed on the top and referred to as the emitter (wafer) or window (thin-film) layer, whereas the p-type material is known as the base (wafer) or absorber (thin-film) layer. The different junctions considered in this study are listed in Table 2-1. Due to the different carrier concentrations, the majority carriers (holes on the p-doped side and electrons on the n-doped side) in the

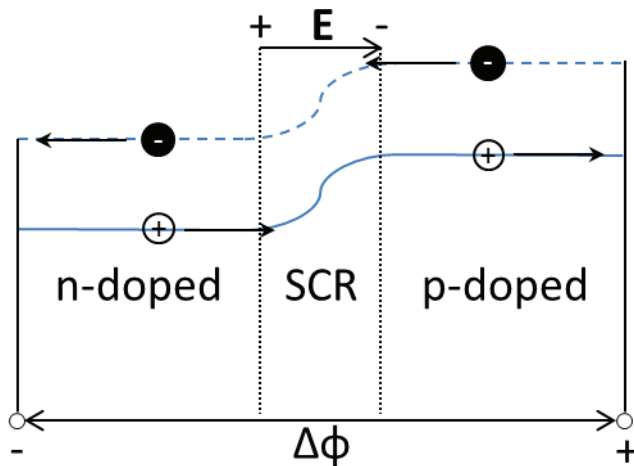


Figure 2-2. Simplified band structure of a solar cell.

regions near the junction on both sides diffuse across the junction and recombine on the other side. Consequently, the regions near the junction become charged and an inner potential difference $\Delta\phi$ corresponding to the displaced carrier concentrations is created, thus, enabling the photovoltaic effect. The resulting electric field E drifts carriers in the opposite direction to that of the diffusion process. This charged region on both sides of the junction is called a space charge region (SCR) and the equilibrium between drift and diffusion determines its width. A simplified band structure of a solar cell is presented in Figure 2-2.

The equivalent circuit of a solar cell presented in Figure 2-3 illustrates the electronic behaviour of a solar cell. As for its structure, a solar cell can be viewed as a large-area p-n diode. The net current across the p-n junction I_d i.e. diode or dark current consists of two opposite components: recombination current I_{rec} , the diffusion of minority carriers from the SCR into the quasi-neutral regions, and thermal generation current I_{th} , the drift of minority carriers across the SCR. In its operating conditions, under illumination, the dynamics generally associated with diodes are changed by the photovoltaic effect, however. When exposed to solar radiation, the solar cell rather behaves like a current source connected in parallel with a diode. The

photogenerated charge carriers separated by the built-in potential of the cell and collected by an external circuit constitute the photogenerated current I_{ph} , which flows in the same direction as I_{th} . When I_{ph} exceeds I_d , the cell output current I changes its direction and becomes negative as per the circuit diagram. This

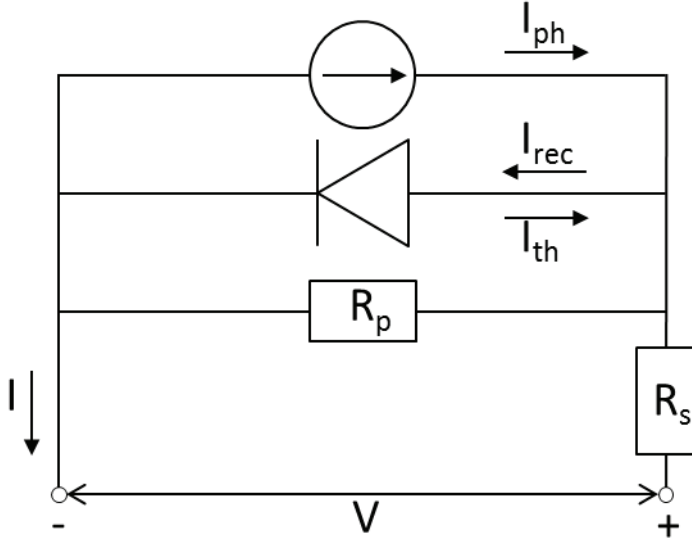


Figure 2-3. Equivalent circuit of a solar cell.

superposition approximation is expressed mathematically in Eq. 2.1.

$$I = I_d - I_{ph} = I_{rec} - I_{th} - I_{ph} \quad (2.1)$$

The current source and diode symbols of Figure 2-3 represent an ideal solar cell. The simulation of the behaviour of a solar cell also requires the consideration of the parasitic resistances within the cell. The series resistance R_s represents the resistance of the parts of the cell that are supposed to provide carriers with a pathway (ideally zero), whereas the parallel resistance R_p or the shunt resistance stands for the resistance of all other parts of the cell (ideally infinite).

When a p-n junction is under thermal equilibrium, I_d is equal to zero due to the balance between I_{rec} and I_{th} . In spite of $\Delta\phi$, there is no electrochemical potential difference across the junction and, hence, no current flowing through the circuit. Under illumination however, the balance between drift and diffusion is disturbed. In relative terms, absorbed photons increase the concentrations of minority carriers on both sides more than those of majority carriers and consequently, an electrochemical potential difference i.e. photovoltage V_{ph} is created. V_{ph} together with an external load can be considered as a forward-bias voltage applied to the junction. This voltage drives photoexcited minority carriers through the load where they do work before recombining on the other side of the junction. Rising V_{ph} drives more minority carriers across the p-n junction, which leads to more diffusion of minority carriers back to the quasi-neutral regions, thus, increasing I_{rec} and reducing $\Delta\phi$. The change in I_{rec} with increasing V_{ph} is normally approximated by the Boltzmann approximation as follows:

$$I_{rec}(V_{ph}) = I_{rec}(0) \exp\left(\frac{qV_{ph}}{kT_c}\right), \quad (2.2)$$

where q stands for the electric charge of carriers, k for the Boltzmann constant, and T_c for the temperature of the junction. I_{th} is significantly less dependent on V_{ph} than I_{rec} and conventionally, I_{th} is assumed not to be a function of V_{ph} . Since it is known that I_{rec} equals I_{th} when the junction is not exposed to light, I_d can be approximated as follows:

$$I_d(V_{ph}) = I_{rec}(0) \exp\left(\frac{qV_{ph}}{kT_c}\right) - I_{th} = I_0 \left[\exp\left(\frac{qV_{ph}}{kT_c}\right) - 1 \right] \quad (2.3)$$

Eq. 2.3 describes the relation between current and voltage in an ideal diode. It is known as the Shockley equation. Instead of I_{rec} or I_{th} at zero voltage, the term reverse saturation current I_0 is often used in the equation. I_0 is highly dependent on temperature and semiconductor material quality.

When considering the Boltzmann approximation and the parasitic losses of a solar cell, I in Eq. 2.1 can be expressed as an implicit function of the voltage V across the terminals of the cell as follows:

$$I(V) = I_0 \left[\exp \left(\frac{e(V - IR_s)}{n_d k T_c} \right) - 1 \right] - I_{ph} + \frac{V - IR_s}{R_p}, \quad (2.4)$$

where e stands for the elementary charge i.e. the absolute value of the electric charge of a single charge carrier and n_d for the ideality factor of a diode ranging from 1 (ideal) to 2. Eq. 2.4 is referred to as the single diode model of a solar cell, based on the equivalent circuit presented in Figure 2-3. At a high V_{ph} and in the case of a thin SRC relative to the thickness of the entire cell, the assumption of an ideal diode is valid as then, I_{rec} mainly consists of minority carriers diffusing from the SRC to the quasi-neutral regions as explained above. With a reducing V_{ph} however, more carriers already recombine in the SCR thus increasing I_d more than the Shockley equation (Eq. 2.3) implies. In order to take the voltage dependence of n_d into consideration, the so called double diode model is often used. This model corresponds to an equivalent circuit in which the one in Figure 2-3 is connected parallel to a pair of series-connected diodes. Hence, instead of one exponential diode current term, the model contains two such terms: one for minority carrier diffusion between the SCR and the quasi-neutral regions and the other for recombination within the SCR. Both terms contribute to I_d but with different ideality factors and saturation current levels. While the diffusion term has an ideality factor equal to unity, the factor of 2 is normally used in the SCR recombination term. The saturation current of the SCR recombination term is approximately two orders of magnitude higher than that of the diffusion term.

If I is measured at different levels of V and plotted, the resulting current-voltage (I-V) characteristic curve will resemble the ones presented in Figure 2-4. There are two curves in the figure: the blue one showing I plotted against an externally applied forward-bias voltage in dark and the orange one showing I plotted against V under illumination. As implied by the superposition principle (Eq. 2.1), the vertical distance between the points of the curves represents I_{ph} at each level of V_{ph} since the blue curve corresponds to the respective values of I_d .

The open circuit voltage of a cell V_{oc} is the forward-bias voltage across the junction at which I becomes zero. Hence, an analytical solution for V_{oc} can be obtained based on Eq. 2.4 in the case of an ideal solar cell ($R_p = \infty$):

$$V_{oc} = \frac{n_d k T_c}{q} \ln \left(\frac{I_{ph}}{I_0} + 1 \right) \quad (2.5)$$

With the above ideality assumptions, short circuit current I_{sc} can be approximated to be equal to I_{ph} based on Eq. 2.4.

On the I-V characteristic curve, there is a point at which the product of I and V i.e. the power output of the cell reaches its maximum P_{mpp} . This point is known as the maximum power point (MPP) of the operating condition in question. By adjusting the voltage drop across the load, MPP trackers keep the operating point of the solar cell near the MPP in changing conditions. The fill factor FF relates the MPP performance of a solar cell to the product of I_{sc} and V_{oc} :

$$FF = \frac{I_{mpp} V_{mpp}}{I_{sc} V_{oc}} \quad (2.6)$$

FF is used to express the conversion efficiency of a solar cell η_c based on I_{sc} , V_{oc} , and the radiant flux incident on the cell Φ_{rad} :

$$\eta_c = \frac{I_{sc} V_{oc} FF}{\Phi_{rad}} \quad (2.7)$$

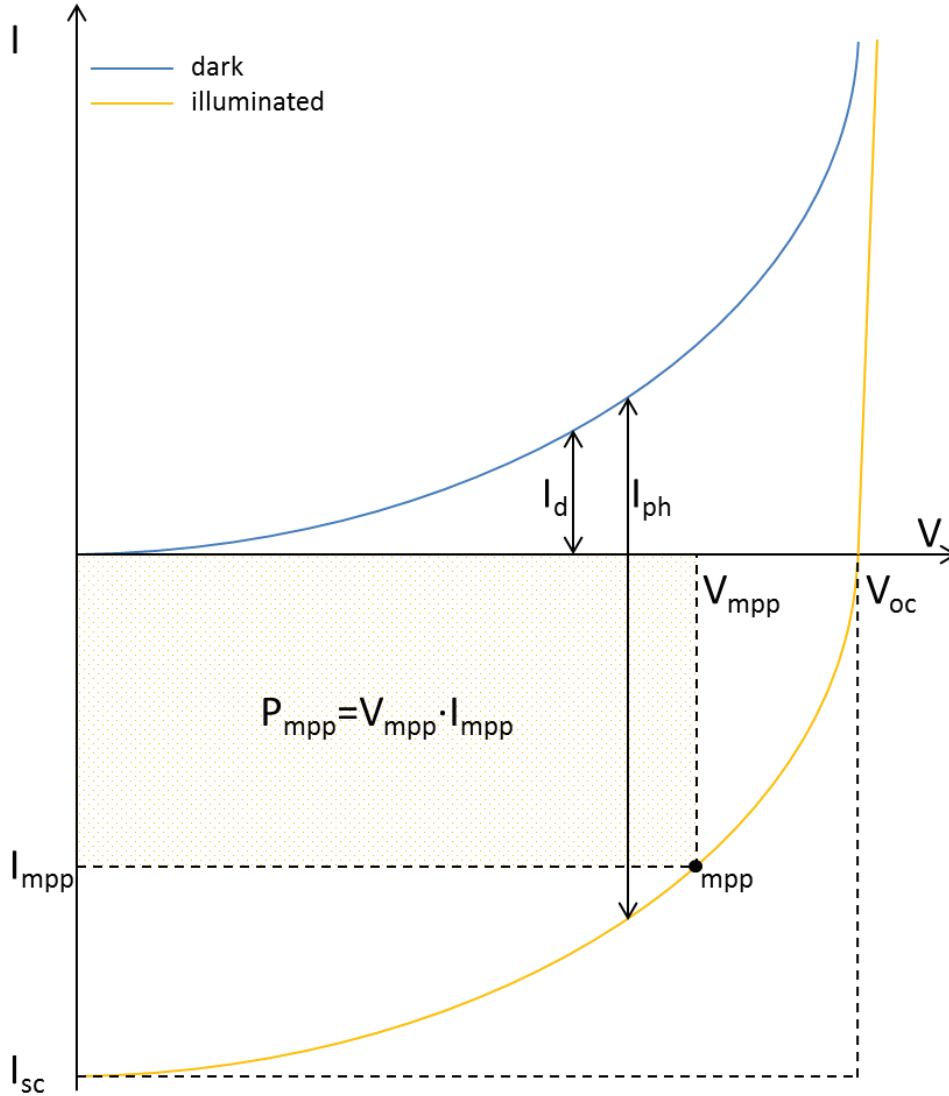


Figure 2-4. I-V characteristics of a solar cell in dark (in blue) and under illumination (in orange).

2.2.2 Solar Array

The output voltage of an individual single-junction solar cell is generally in the order of hundreds of millivolts. Such a voltage level is often insufficient for practical applications and therefore, cells are connected in series forming modules of dozens of cells. In the case of wafer-based technologies, solar cells are fabricated individually and assembled into solar modules, whereas thin-film cells are manufactured monolithically and separated from each other through scribing at the end. In module assembly, cells are bonded to each other through wires connecting the front and back contacts of adjacent cells and encapsulated between glass and ethylene-vinyl acetate (EVA) layers. In utility-scale PV systems, the voltage levels required for efficient power conversion are created by further connecting several modules into

strings and arrays. In strings, modules are connected in series while arrays consist of either one string or several strings connected in parallel.

In a string, an equivalent current flows through every cell and hence, the cell with the lowest output current determines the current of the entire string. If the output current of one cell drops due to shading or surface damage, V_{ph} over the other cells increases in order for the current level to decrease. In the case of a constant load, this increasing forward bias of the other cells reversely biases the low current cell and consequently, the low current cell heats up and may be damaged. This hot spot heating phenomenon is partially avoided through using bypass diodes in parallel with cells. In the reverse bias conditions described above, these diodes create an alternative current path thus limiting the current passing through the low current cell. In the case of strings connected in parallel, partial shading may also cause current to flow to a low current string from other strings. This can be avoided by connecting blocking diodes in series with strings.

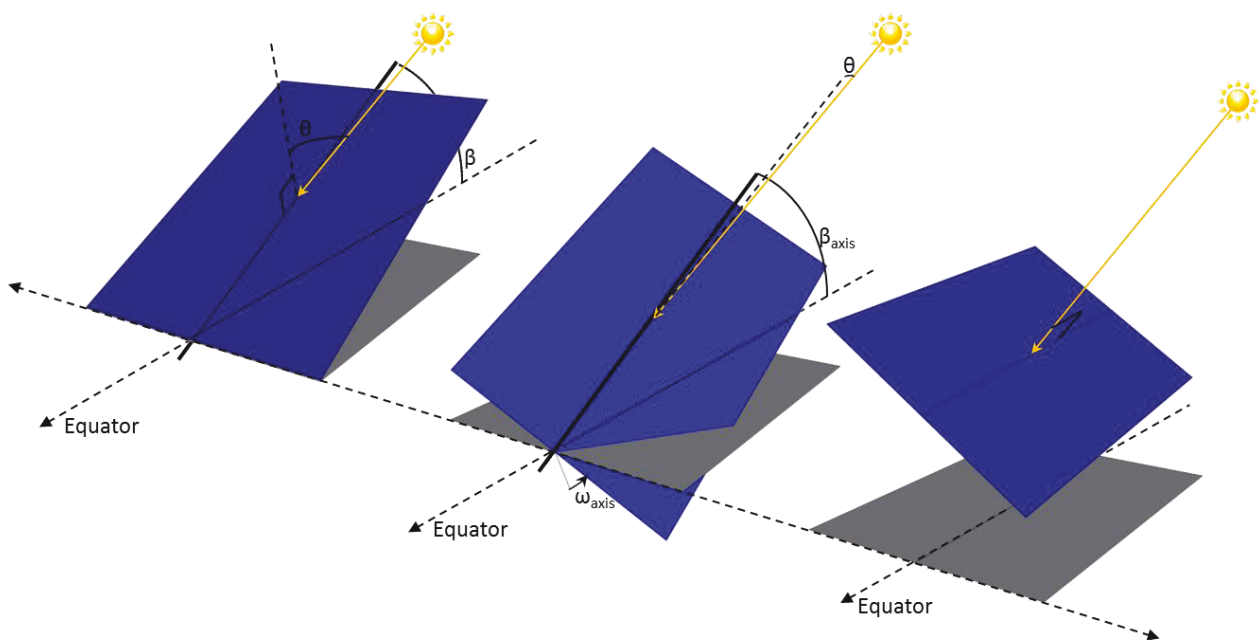


Figure 2-5. Geometry of fixed mount, single axis tracking and dual axis tracking systems.

Based on their inclination i.e. tilt angle, mounting systems can be divided into three categories: fixed mount, single axis tracking, and dual axis tracking systems. The geometry of the three different mounting options is illustrated in Figure 2-5. A fixed mount system has a fixed tilt angle β with the plane of the array ideally orientated towards the Equator. The optimum tilt of a PV array depends on local solar geometry and weather conditions. At low latitudes, it is a common practice to tilt arrays at an angle equal to the latitude of the site. In this way, the annual mean of the angle of the Sun's rays incident on the plane of the array at solar noon can be minimised. This is an effective method in areas close to the Equator and with a low seasonal variability in weather conditions. In most site locations however, the optimal inclination is highly dependent on seasonal changes in weather and in shading due to the Earth and the array itself. Consequently, the latitude tilt is not a recommendable method to be used universally for the optimal inclination of PV arrays.

A single axis tracking system has an axis with a fixed tilt angle β_{axis} orientated towards the Equator. As in the case of fixed mount, β_{axis} can be set to an angle ranging from 0 to 90 degrees. With single axis

tracking, vertical ($\theta_{\text{axis}} = 90^\circ$) and horizontal ($\theta_{\text{axis}} = 0^\circ$) geometries are widely used at high and low latitudes, respectively and, therefore, they are far more common than with fixed mount. When θ_{axis} equals the site latitude, a system is known as polar aligned. Over the day, the plane of the array rotates around the axis at an axis rotation angle ω_{axis} in order to minimise the angle of incidence ϑ , thus, maximising Φ_{rad} . In the case of a dual axis tracking system, ϑ is ideally kept fixed at 0° . The array is orientated towards the Sun by constantly changing the tilt angles of the two axes of its tracking system.

2.2.3 Electric Power Converter

The charge carriers generated in a PV array only flow in one direction driven by relatively low voltage levels. By contrast, electric power is normally delivered to consumers through high or medium voltage transmission lines using alternating current (AC) i.e. current reversing its direction in a fixed frequency range. Therefore, a power conditioner is required to feed the variable low voltage direct current (DC) power produced by a PV system into the grid. Such DC-AC converters are commonly known as solar inverters. In this thesis, the term solar inverter is used to refer to a utility-scale central inverter with an internal transformer. Decentralised concepts also exist, such as string inverters and micro-inverters integrated in individual modules, but currently, most utility-scale power plants are equipped with central power conditioning units. Since the electrochemical potential difference over the series-connected modules of each array determines the voltage of the entire system, central inverters are connected in parallel with several arrays to reach optimal input power levels. In order to reduce cabling, so called generator junction boxes i.e. DC combiner boxes are usually placed between arrays and the inverter. They combine the solar cables from up to two dozens of arrays into a DC main cable whose current level is the sum of the combined array currents. DC main cables connect junction boxes to the inverter and an AC main cable connects the inverter to the grid. The most common conductor material used in PV power stations is copper due to its high conductivity and robustness. In the case of DC and AC main cables, aluminium is also used owing to its relatively low price.

In utility-scale power plants, solar inverters have three main functions: MPP tracking, power conditioning, and anti-islanding protection. MPP tracking is done through estimating the MPP of an entire operational power plant based on periodic current and voltage measurements. The system voltage is adjusted to the prevailing MPP by a DC-DC switching converter inside the inverter. Since I-V characteristics vary between modules due to manufacturing tolerance and different ambient conditions in different parts of the power station, the MPP of the entire plant is likely not to be the same as the MPPs of individual modules or arrays in the case of a centrally operating MPP tracker. Therefore, P_{mpp} of an operational centrally controlled plant cannot be expected to reach the combined P_{mpp} of individual modules.

Power conditioning involves alternating, filtering, and stepping down the DC current generated by PV cells. Some utility-scale inverters perform all these functions whereas sometimes, separate transformers are used for stepping down current. Inverters first alternate the input DC current by means of a solid state switch circuit. The resulting approximated sine wave is smoothed and filtered in a resonant circuit consisting of magnetic components. A transformer finally steps down the low voltage AC current to reach the grid voltage, and the output power is fed into the grid.

The third important function of a grid-tied inverter is to ensure that the system is disconnected from the grid if the grid voltage goes outside the acceptable range. In an extreme case where the grid has been locally disconnected, a grid-connected PV system causes a severe hazard to utility personnel unless disconnected from the grid. A situation where an operational distributed generator is connected to a

disconnected grid is known as islanding. Through anti-islanding algorithms, an inverter constantly checks for the presence of the grid and stops injecting AC power in case it detects an island.

2.3 Determinants of Output

The output of an operational PV power station is determined by prevailing ambient conditions and the properties of selected PV and BOS technologies. The most important determinant is obviously the level of solar radiation, which dictates the ultimate limit for the output of any solar energy converter. The factors influencing incident irradiance are discussed in the first subsection. According to the second law of thermodynamics, the ultimate limit (η_c of 100 %) cannot be achieved in any circumstances. This is due to the loss pathways intrinsic to the photovoltaic conversion process. These intrinsic losses are caused by two phenomena fundamentally associated with the operation of semiconductor-based solar cells with a finite number of p-n junctions: spectral mismatch and recombination. The spectral mismatch-induced loss processes are discussed in the second and third subsections addressing optical losses and carrier thermalisation. The fourth subsection deals with recombination. The optical and recombination losses also involve extrinsic processes, which, in theory, can be avoided through design optimisation in ideal conditions. In the case of operational PV stations however, the extrinsic processes cause a major share of the total losses. These losses also include parasitic mechanisms discussed in subsection 2.3.5. Figure 2-6 illustrates the aforementioned loss processes as a sequence following the absorption of sunlight. The processes depicted in Figure 2-6 are explained in detail in the following subsections.

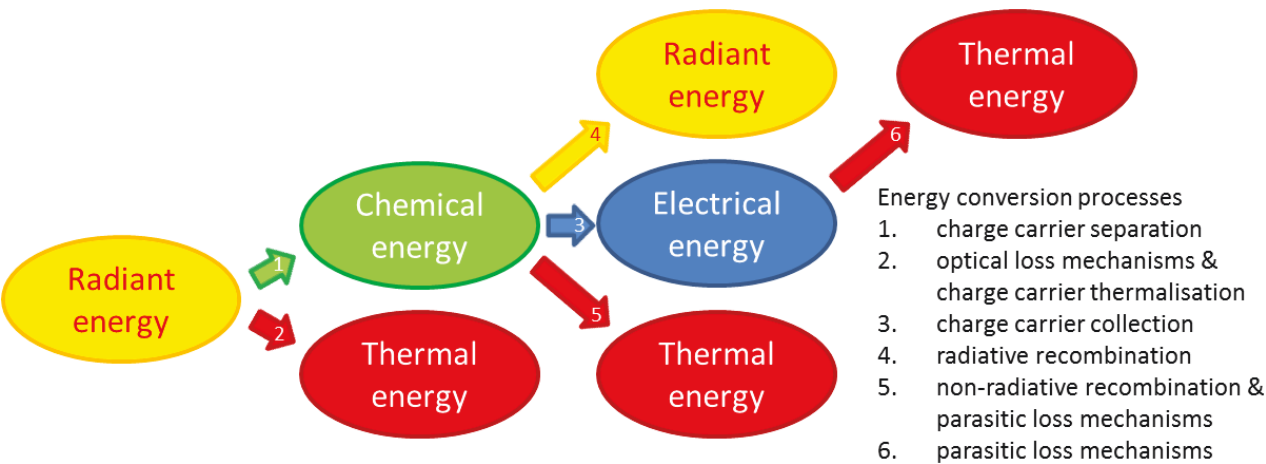


Figure 2-6. Loss pathways involved in the photovoltaic energy transformation process.

Table 2-2 elucidates the relationship between the loss mechanisms and various PV performance factors. In addition to the ambient and technological parameters directly influencing performance, there are technology-dependent processes that indirectly affect the losses through changing the technological parameters. The three most important such processes are the heat transfer energy exchange between a solar cell's p-n junction and its ambient environment, time-dependent degradation, and MPP tracking (see section 2.2.3). The fundamentals of heat transfer energy exchange are discussed in association with optical losses in subsection 2.3.2.

Table 2-2. Ambient and technological determinants of the loss mechanisms involved in the photovoltaic process.

Loss mechanism	Ambient determinants	Technological determinants
Optical losses Intrinsic and extrinsic pathways Occurrence as current and voltage drops at cell level	<ul style="list-style-type: none"> • solar position (ϑ_z, φ_s) • incident solar spectrum • dust deposition <ul style="list-style-type: none"> ○ concentration per unit area ○ chemical composition • heat transfer energy exchange <ul style="list-style-type: none"> ○ W_{poa} ○ T_a ○ \mathbf{v}_w ○ T_{sky} ○ ϵ_{sky} ○ T_{ls} ○ ϵ_{ls} 	<ul style="list-style-type: none"> • β • $E_{g,\text{stc}}$ • absorptivity • reflectivity • A_{act} • time-dependent degradation • heat transfer energy exchange <ul style="list-style-type: none"> ○ module heat capacity ○ $A_{\text{ap}} (A_{\text{act}} + A_{\text{ofc}})$ ○ absorptivity ○ reflectivity ○ ϵ_{mod} ○ η_c (coupled relationship)
Thermalisation Intrinsic pathway Occurrence as voltage drop at cell level	<ul style="list-style-type: none"> • incident solar spectrum • heat transfer energy exchange (see the row “Optical losses”) 	<ul style="list-style-type: none"> • $E_{g,\text{stc}}$ • heat transfer energy exchange (see the row “Optical losses”)
Recombination Intrinsic and extrinsic pathways Occurrence as current and voltage drops at cell level	<ul style="list-style-type: none"> • heat transfer energy exchange (see the row “Optical losses”) and its variability between modules connected to a single inverter MPP input • W_{abs} and its variability between modules connected to a single inverter MPP input 	<ul style="list-style-type: none"> • $E_{g,\text{stc}}$ • doping • material purity • surface passivation • reversible lattice meta-stabilities due to light soaking • time-dependent degradation • heat transfer energy exchange (see the row “Optical losses”) • MPP tracking <ul style="list-style-type: none"> ○ inverter operating range ○ $V_{\text{oc,stc}}$ ○ MPP tracking algorithm accuracy ○ performance variability between modules ○ time-dependent degradation variability between modules
Parasitic losses Extrinsic pathway Occurrence as current and voltage drops at cell, module, and system levels	<ul style="list-style-type: none"> • W_{abs} and its variability between modules connected to a single inverter MPP input • heat transfer energy exchange (see the row “Optical losses”) and its variability between modules connected to a single inverter MPP input • grid voltage 	<ul style="list-style-type: none"> • $R_{p,\text{stc}}$ • $R_{s,\text{stc}}$ • $V_{\text{oc,stc}}$ • conductor resistivity • wire run lengths • time-dependent degradation • heat transfer energy exchange (see the row “Optical losses”) • MPP tracking (see the row “Recombination”) • power conditioning efficiency • BOS self-consumption

Symbols: ϑ_z = solar zenith angle, φ_s = solar azimuth angle, W_{poa} = plane-of-array irradiance, T_a = ambient air temperature, \mathbf{v}_w = wind velocity vector, T_{sky} = sky temperature, ϵ_{sky} = sky emissivity, T_{ls} = land surface temperature, ϵ_{ls} = land surface emissivity, β = array inclination angle, $E_{g,\text{stc}}$ = band gap energy at standard test conditions (STC), A_{act} = module active area, A_{ap} = module aperture area, A_{ofc} = surface area of opaque front contact, ϵ_{mod} = module surface emissivity, η_c = conversion efficiency of a solar cell, W_{abs} = irradiance absorbed by the PV material, $V_{\text{oc,stc}}$ = module open-circuit voltage at STC, $R_{p,\text{stc}}$ = shunt resistance at STC, $R_{s,\text{stc}}$ = series resistance at STC.

Given a fixed level of irradiance incident on the plane of an array W_{poa} , the output can be decreased either through reduced flux of photons and charge carriers or reduced carrier energies. A mechanism influencing the flux of photons and carriers has an impact on the output current, whereas the output voltage is dependent on carrier energy. Whether the loss mechanism results in a current drop, a voltage drop, or

both is also specified in Table 2-2. The current drops due to different loss mechanisms can be illustratively presented by plotting the change in cumulative photon or carrier flux density reduced by the mechanism of interest when proceeding from the high energy side of the solar spectrum towards lower energy levels. Similarly, voltage drops can be shown as shifts in the utilisable carrier energy. Such an approach is illustrated in Figure 2-7 for two different PV materials with very different spectral responses, c-Si and a-Si. Depending on the loss process, the photon flux density can be used interchangeably with the cell output current density. Also, the levels of photon energy in eV can be directly translated to volts in the context of cell output voltage. This approach is subject to the assumption that each photon has the potential to generate only one EHP. The loss processes included in Figure 2-7 comprise the losses occurring on the DC side of the power station under the standard test conditions (STC) of PV devices.

The spectra shown in Figure 2-7 are based on the standards for extraterrestrial beam irradiance, ASTM E-490-00 (E21 Committee, 2014), and terrestrial global irradiance ($\theta = 37^\circ$, ϑ_z of 48.2°), ASTM G173-03 (G03 Committee, 2012). The optical losses are estimated based on Santbergen's (2008) measurements of the absorptivity of different layers of c-Si wafer-based and a-Si thin-film solar cells. In order to compute the electrical performance-related losses with the chosen materials, the reference module types are selected: Canadian Solar CS6X-320M for c-Si and NexPower NH-100AT 5A for a-Si. The required parameters are obtained from the module database of the software PVsyst V6.26 (PVsyst SA, 2014a). The operating power point of the power station can be found in the top-right corner of the red rectangle representing the power output. The operating point is slightly deviated from the I-V characteristic curve of the cell because of the assumed DC transmission losses resulting in an additional voltage drop of 2%. Furthermore, the cell itself is assumed to operate slightly below its MPP due to array mismatch and MPP tracking inaccuracy leading to a power loss of approximately 2% as well. The following subsections further discuss each of the loss processes and their dependence on the different ambient and technological parameters given in Table 2-2.

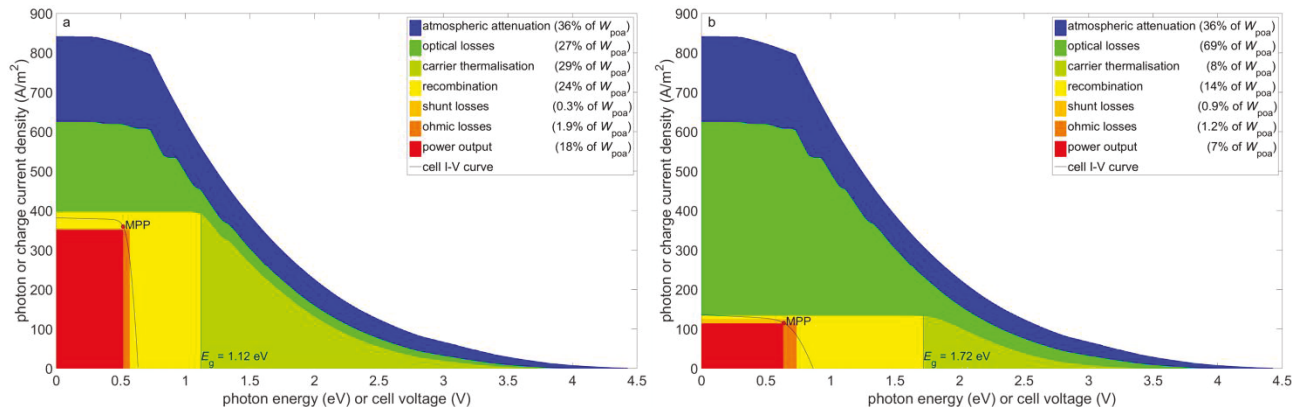


Figure 2-7. Loss processes involved in the utilisation of solar energy under the standard test conditions through PV power stations equipped with (a) Canadian Solar CS6X-320M c-Si wafer-based solar modules or (b) NexPower NH-100AT 5A a-Si thin-film solar modules.

2.3.1 Irradiance

Beam normal irradiance on the top of the Earth's atmosphere currently ranges approximately from 1320 W/m^2 to 1410 W/m^2 during a year. The fluctuation is due to the elliptical shape of the Earth's orbit and the consequently changing distance from the Sun. The irradiance at the mean distance is referred to as the solar constant, whose value has recently been found to fluctuate between 1361 W/m^2 and 1362 W/m^2

depending on solar activity (Kopp and Lean, 2011). The Sun-Earth distance affects the number of photons per unit area but does not have a significant impact on the probability distribution of photon energy i.e. the shape of the solar spectrum. The slight shifts in the spectrum due to the Doppler effect can be neglected in this context. The impacts related to changes in the shape of the incident spectrum are referred to as the spectral effects in this thesis.

Atmospheric attenuation outplays the extraterrestrial phenomena as the cause of irradiance variability on terrestrially installed PV arrays. Solar radiation is scattered, absorbed, and reflected by the atmosphere and consequently, the transmitted spectrum can be significantly different from the spectrum on the top of the atmosphere as can be seen from Figure 2-7. This attenuation process is dependent on the atmospheric conditions as well as the length of photons' path from the top of the atmosphere to the array. The atmospheric variables relevant for the process are cloudiness, and atmospheric aerosol content and gas composition.

Thick clouds have been found to bring global irradiance down to a minimum of 3 % of its top-of-atmosphere value (Geiger et al., 2002). This extinction is not spectrally completely neutral being usually slightly concentrated on low-energy photons ($h\nu < 2.5$ eV) (Bartlett et al., 1998; Siegel et al., 1999). In the visible part of the spectrum, the phenomenon is caused by the spectrally sensitive reflection properties of water droplets and ice crystals (Kokhanovsky, 2004). According to Bartlett et al. (1998), the spectral effect is intensified by increasing ground reflectance i.e. albedo. Therefore, clouds on the snowy or arid terrains characterised by comparatively high and spectrally neutral albedo levels (Stammes et al., 2004) can be expected to lead to a notable blueshift in the spectrum incident on arrays shaded by them. This impact favours high-band gap PV materials.

In most arid regions such as the Arabian Peninsula, the contribution of aerosols to the total atmospheric attenuation of solar radiation is usually higher than that of clouds. During clear sky events with heavy aerosol loading, an irradiance drop of a magnitude similar to that due to an overcast sky is possible as per observations performed by ReCREMA in the UAE (Beegum, 2014). In contrast to clouds however, aerosol-induced extinction in the visible part of the solar spectrum mostly occurs via scattering (Dubovik et al., 2002). Because the size distribution of typical desert dust aerosols is concentrated on large particles with radii longer than $0.6\text{ }\mu\text{m}$, scattering increases with wavelength due to intensified Mie scattering (Dubovik et al., 2002). Therefore, the wavelength dependence of the attenuation via desert dust leads to a blueshift as in the case of clouds. However, this only applies to conditions where aerosols mostly consist of pure desert dust particles. In the Persian Gulf area for instance, a typical aerosol particle size distribution has two peaks: one for desert dust and the other for finer aerosols of urban and industrial origin (Gherboudj and Ghedira, 2014; Smirnov et al., 2002). As per Smirnov's et al. (2002) measurements in Bahrain in 1998-1999, the peak representing desert dust was significantly higher from March to September whereas in winter and late autumn, the fine aerosol peak was either comparable to or higher than the desert dust peak. The findings of Gherboudj and Ghedira (2014) show similar seasonal variation in the UAE, Bahrain, and Riyadh Region, Saudi Arabia for a time period from 2004 to 2007. The increased role of absorption via urban and industrial aerosols actually inverts the wavelength dependence of desert-type scattering-oriented aerosol extinction from late summer to early spring. The resulting redshift in the visible part of the spectrum favours low-band gap PV materials.

Cloudiness and atmospheric aerosol content are parameters that experience significant variability in space and time. To less extent, so do some of the atmospheric gases, most notably water vapour and

ozone. These gases influence the incident spectrum by absorbing photons with specific energy levels resulting in deep drops in irradiance at certain wavelengths. While water vapour absorbs photons in the infrared and near-infrared regions of the spectrum, the absorption via ozone is concentrated in the ultraviolet region. Water vapour does not only affect the spectrum via direct absorption but also influences the optical properties of atmospheric aerosols (Dubovik et al., 2002). Atmospheric attenuation occurs even in a clean atmosphere only consisting of air molecules (O_2 , N_2 , and trace gases). The air-induced absorption and scattering shave the peak of the extraterrestrial spectrum in the near ultraviolet region and, hence, represent an important attenuation mechanism. This pathway chiefly accounts for the atmospheric attenuation between the standard spectra used in Figure 2-7. The mechanism does not experience significant spatial or temporal variation.

As mentioned above, also the optical path length traversed by light in the atmosphere has a major impact on the irradiance incident on an array. The path length depends mainly on the Sun's position relative to the plant site and, to much less extent, on the site's elevation. The longer the path length, the stronger is the attenuating effect of the atmosphere. The optical path has also spectral effects as the absorption and scattering via air molecules and fine aerosols concentrate on the high energy part of the solar spectrum. That is why the colour of sunlight often appears to turn from blue to red while the Sun is setting. A common measure used for the optical path length is air mass (AM), which, in this context, is defined as the ratio of the path length to the height of the atmosphere i.e. the zenith path length at sea level. AM is zero on the top of the atmosphere and one at sea level when the Sun is at the zenith. The maximum AM, which is reached at sunrise and sunset, is approximately 38. AM of 1.5 ($\vartheta_z = 48.2^\circ$) is one of the parameters used in defining the light source for PV module testing at STC.

Finally, the incident irradiance can also be affected by changing the orientation of the plane of the array as discussed in section 2.2.2. The different parts of the sky and the ground radiate photons at varying intensities. In the case of a clear and clean atmosphere with no shading, the part of the sky with the highest irradiance is the sun disk. In such conditions, the power output of a PV plant can be optimised by inclining the plane of the array towards the Sun and, hence, bringing ϑ to its minimum. In this way, the cosine effect is minimised. Though, the sun disk part of the sky is not always the brightest region due to cloud coverage, heavy aerosol loading, or shading. In the case of a clear and clean sky, the angular distribution of irradiance has a well-known pattern characterised by circumsolar and horizon brightening. Both phenomena are reinforced by atmospheric aerosols when distributed with no azimuthal dependence (Perez et al., 1987). In addition to the sky, the land surface around the array is a source of radiation. The extent and variability of this ground-reflected irradiance is naturally dependent on the albedo of the surface.

2.3.2 Optical Losses

When a solar module is exposed to light, part of the light is absorbed through interband absorption in the semiconductor layers thus generating charge carriers. The rest is either reflected or absorbed by the other layers of the module or by free carriers in the semiconductor layers. In this thesis, the term optical losses is used to refer to the fraction of the incoming irradiance that does not generate charge carriers. The term therefore comprises not only extrinsic optical losses such as surface reflection and contact shadowing but also the loss of sub-band gap photons, which is a fundamentally unavoidable, intrinsic loss mechanism.

As can be seen from Figure 2-7, optical losses cause a current drop in that they restrict the number of photons generating charge carriers. The loss mechanism is affected by the spectral mismatch between the spectrum of incoming light and the interband absorption of the single band gaps of a solar cell's

semiconductor layers. Since the photons with energies higher than E_g will be far more likely to be absorbed through interband absorption than the sub-band gap photons, optical losses drastically drop as photon energy approaches and exceeds E_g . Hence, the materials with wider band gaps intrinsically incur higher optical losses. In the case of supra-band gap photons, optical losses mostly consist of reflection and absorption in the glass surface, the top contact, and the ARC of the cell. The loss of sub-band gap photons depends on the cell technology in question. In the case of wafer-based solar cells, most of the sub-band gap optical losses consist of FCA in the heavily doped emitter (Santbergen, 2008). By contrast, in thin-film cells, only a small fraction of sub-band gap irradiance reaches the semiconductor and the rear contact layers as most of it is absorbed through FCA in the heavily doped TCO layer (Santbergen, 2008). Despite the fact that the contribution of sub-band gap photons to charge carrier generation is insignificant even in an ideal solar cell, their absorption mechanism is of great interest. This is due to their effect on the operating temperature of the cell T_c (see section 2.1), which affects cell output in various ways. From the power output point of view, the impact of rising T_c is negative (see sections 2.3.3 and 2.3.4) although optical losses actually decrease with rising temperature.

T_c is determined by processes both internal and external to the cell. As discussed above, all incident sunlight absorbed is not converted into electricity but most of it produces heat within a module. This internal heating process depends on the conversion efficiency of the cells. Due to the process, an evenly illuminated solar module is warmer than the surrounding air in the case of a stable ambient air temperature. The module cools down through the three main heat transfer mechanisms. Conduction is, however, often regarded as negligible when using ground mount racking systems. Adapted from the formulation of Jones and Underwood (2001), Eq. 2.8 expresses the thermal energy exchange between a module and its environment:

$$C_{\text{mod}} \frac{dT_{\text{mod}}}{dt} = q_{\text{rad}} + q_{\text{conv}} - P_{\text{mpp}}, \quad (2.8)$$

where C_{mod} stands for the module heat capacity, T_{mod} for the module operating temperature, t for time, q_{rad} for the radiant heat transfer rate, q_{conv} for the convective heat transfer rate, and P_{mpp} for the power output of the module. C_{mod} is a combination of the heat capacities of the different layers the module is made of. q_{rad} consists of the radiant fluxes between the module and the Sun, the sky, and the land surface. Therefore, it depends on W_{poa} as well as the temperature gradients between the module and its surroundings. q_{conv} is a function of the temperature difference between the module and the air encapsulating it as well as the flow rate of the air close to the module surface. Thus, q_{conv} is directly proportional to wind speed at the module surface. Finally, P_{mpp} is contingent upon W_{poa} and η_{mod} . The temperature of the p-n junction being a determinant of η_{mod} via various mechanisms, P_{mpp} and T_{mod} have a coupled relationship. Should the thermal properties of the different layers of the module be known, T_c can be estimated based on T_{mod} .

The band gap itself is a function of temperature as can be seen from Figure 2-9. The band gap levels given in the figure have been estimated based on Weiser and Mell (1989) in the case of silicon-based materials and by means of the Manoogian-Woolley equation (Manoogian and Woolley, 1984) with fitting parameters obtained from the literature (Fonthal et al., 2000; Lárez et al., 1994; Powalla et al., 2011) in the case of the three other. As can be seen from the figure, rising temperature narrows the band gap of a semiconductor material and therefore decreases the current drop due to intrinsic optical losses as shown in Figure 2-8.

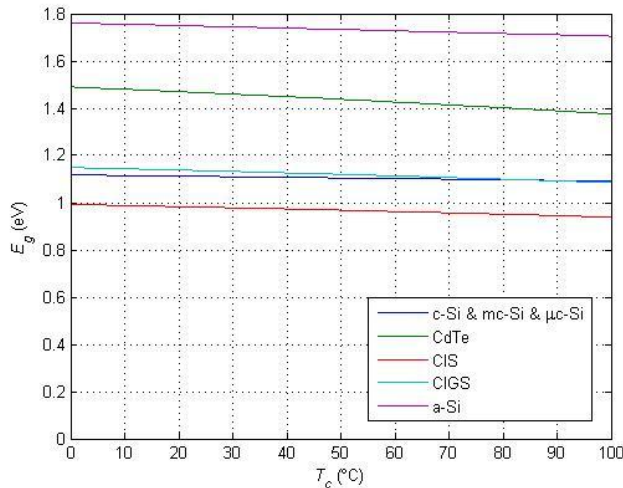


Figure 2-9. Temperature dependence of the band gaps of the photovoltaic materials under consideration.

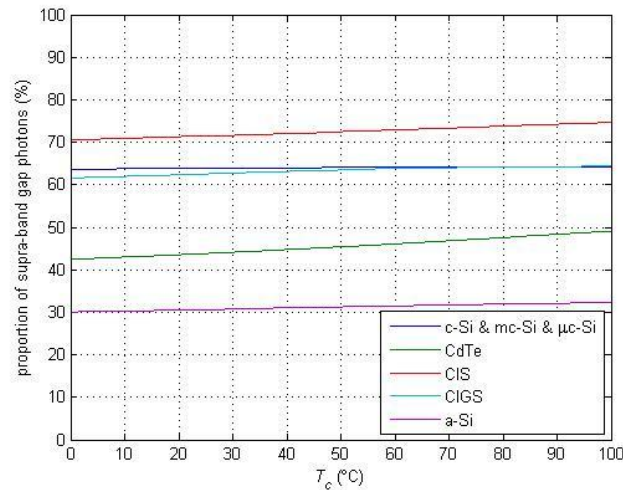


Figure 2-8. Temperature dependence of the proportion of supra-band gap photons to the entire global ASTM G173-03 reference spectrum.

Martín et al. (2012) and Khoo et al. (2014). Due to its mitigating effect on angular reflection losses, surface texturing is particularly beneficial in site locations characterised by high levels of diffuse irradiation such as those under hot desert climates.

In addition to texturing, the top surface is often layered with ARC. At a certain wavelength, the light reflected at the top surface of such a coating is in the opposite phase to the light reflected by the rear surface. As a result, the two wavefronts destructively interfere with each other and effectively eliminate reflection. The wavelength at which reflection is minimised is determined by the thickness and the refractive index of the coating. Therefore, the two are important design parameters in the maximisation of charge carrier generation. The parameters are chosen to concentrate the impact of destructive interference on the supra-band gap part of the spectrum. In an ideal case, the entire sub-band gap part of the spectrum would, in turn, be reflected in order to minimise the heat dissipated through FCA and absorption in the non-active layers of a module such as the rear metal contact. In order to minimise the

The intrinsic optical losses can be influenced only by modifying either the spectrum of the incoming light or the active materials' band gaps. Therefore, they cannot be even theoretically avoided in the conventional flat-plate design of a solar cell with a limited number of p-n junctions. By contrast, significant reductions in extrinsic optical losses have been achieved through improving the optical characteristics of solar modules. The most significant extrinsic loss mechanism is reflection, which accounts for the entire non-absorbed part of incoming irradiance as solar modules are assumed to be opaque. Reflectance is influenced by the angle of incidence ϑ and the difference in refractive indices between the two interfacing media. Furthermore, the rougher the surface is, the less light is reflected off. This is due to on average higher optical path lengths and the higher probability of light being reflected back to the surface. The longer optical path lengths are achieved by the randomised directions of incident rays and the resulting increase in total internal reflection. That is why surface texturing is commonly used to improve light trapping i.e. optical confinement inside the cell. Despite cell surface texturing however, absorption probability typically drops with angles of incidence (POA) higher than 70° (Martín and Ruiz, 2001). However, the angular reflection losses can be significantly reduced by using textured glass surfaces as demonstrated by

absorption of light in the rear contact, also the rear surface is typically textured for the reasons discussed above. Apart from the breakage of the module top glass surface, the most important reason for the long-term degradation of the optical performance of a solar cell is the ingress of water into the cell and the subsequent oxidation process in ARC (Honsberg and Bowden, 2014). Also, encapsulant discolouration has been identified as a cause of optical degradation (Meyer and Van Dyk, 2004).

The third component of extrinsic optical losses, in addition to reflection and absorption in the non-active layers, is shading due to the top metal contact in the case of wafer-based cells. The opaque metal grid on the top surface of a cell prevents light from entering the cell while transferring heat into the cell through thermal conduction. From the viewpoint of optical losses, it makes sense to minimise the area covered by the contact. In fact, there are commercial examples of the entire top contact having been placed on the back side of a cell (Swanson, 2009). Alternatively, the contact can be made transparent as in the case of most thin-film modules.

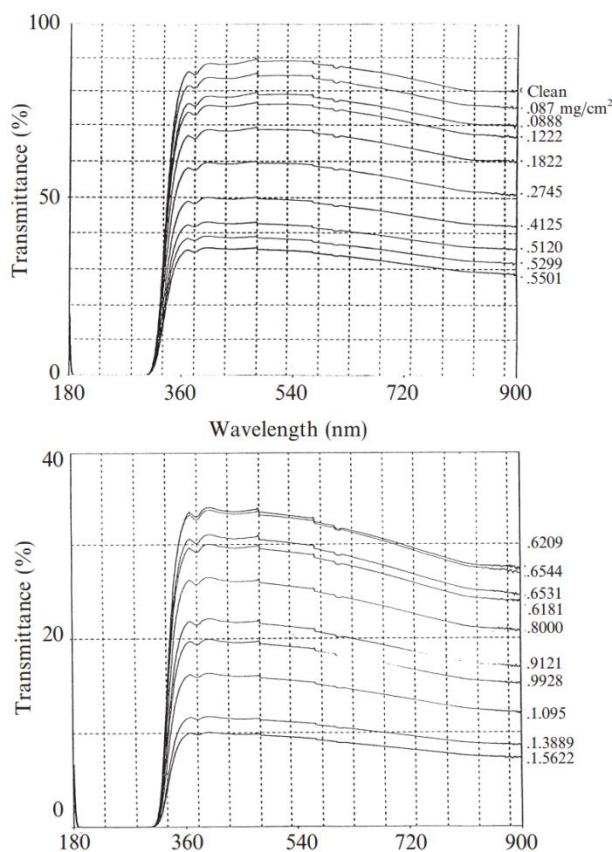


Figure 2-10. Spectral transmittance of a module surface with different concentrations of deposited sand dust. (Al-Hasan, 1998).

In addition to the cell design parameters, the operating environment has a major impact on the optical characteristics of a module surface. Under desert climates, the primary environmental factor is dust deposition. Dust and dirt deposited on a module surface absorb and reflect light and therefore cause a drop in output current. The current drop is obviously a function of dust accumulation as shown e.g. by Al-Hasan (1998) and Mailutha et al. (1994). Figure 2-10 presents the results of a controlled laboratory study on the effect of sand dust accumulation on the spectral transmittance of a glass surface layer (Al-Hasan, 1998). As per the figure, it seems that the effect of dust concentration on transmittance does not have considerable wavelength dependence. However, since dust morphology and size distribution significantly vary by season and location, more measurements in actual operating conditions are required for any general conclusions about the spectral distribution of the losses.

The current drop due to dust deposition has also been proven to have a strong dependence on ϑ (e.g. Martín and Ruiz, 2001; Martín et al., 2012). Martín and Ruiz showed that reflectance is

exponentially proportional to ϑ with a slope depending on the amount of dust deposited on the module surface. The exponential relationship is demonstrated in Figure 2-11 where the normalised transmittances of a clean surface and a soiled surface are plotted against ϑ . As can be inferred from the figure, a high incidence angle of incoming light increases dust deposition-related optical losses compared to a beam that is normal to the surface but has the same intensity. Mailutha's et al. (1994) and Wilson and Ross's (1983) earlier findings support Martín's et al. (2012) results. Hence, modules installed in site locations with a high diffuse irradiation component can be expected to suffer from higher optical losses than modules in

locations with a lower diffuse component but similar soiling conditions and total irradiation. The effect of dust deposition on the output current of a solar cell is not dependent on the active material of the cell according to Martín's et al. findings.

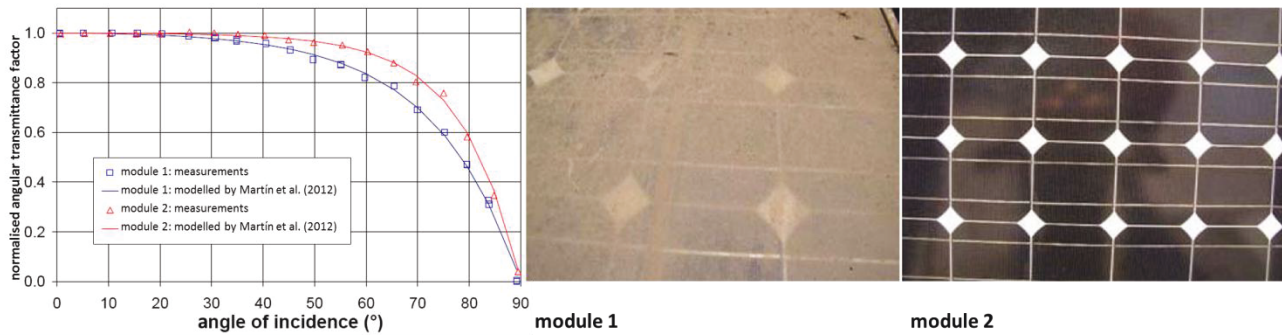


Figure 2-11. Effect of dust deposition on the angular reflectance factor of the module top surface. Adapted from Martín et al. (2012).

2.3.3 Thermalisation

As discussed in section 2.3.2, the spectral mismatch between the spectrum of incoming light and the interband absorption of the single band gaps of a solar cell's semiconductor layers causes the fundamental loss of sub-band gap photons. Due to the same mismatch, the difference between E_g and the energy levels of absorbed supra-band gap photons is lost through heat dissipation as explained in section 2.1. In this process of carrier thermalisation, the excess energy of photons is released as heat into the lattice of the semiconductor material as excited electrons cool down to the edge of the conduction band and holes to that of the valence band. Since the loss mechanism restricts the energy that can be transferred from photons to charge carriers, it causes an intrinsic, fundamentally unavoidable drop in the output voltage of a solar cell as can be seen from Figure 2-7. In contrast to the loss of sub-band gap photons, thermalisation is reduced with an increasing E_g and, therefore, the resulting losses are directly proportional to T_c (see Figure 2-9).

The spectral mismatch-related loss processes, thermalisation and non-absorption of sub-band gap photons, are the two most important loss mechanisms in PV energy conversion. As shown in Figure 2-12, these losses cover more than half of the energy of incoming light in the case of a solar cell that is operated at STC and incurs no extrinsic optical losses. In such ideal conditions, the optimum band gap is approximately 1.1 eV and therefore, the lowest total spectral mismatch amongst the seven materials considered can be achieved by CIGS. The band gap of crystalline silicon is close to that of typical CIGS devices but because it is indirect, the c-Si step function absorbance given in Figure 2-12 is actually overestimated near the band edge. Thus, the spectral mismatch of CIGS is lower than that of crystalline silicon.

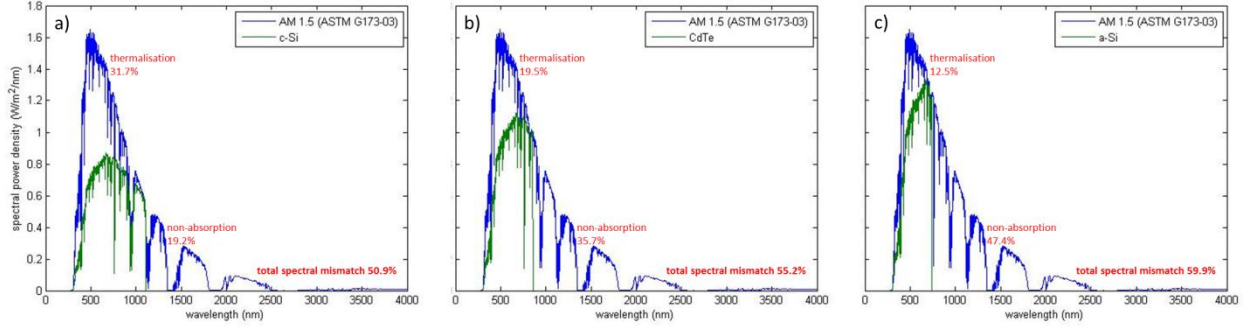


Figure 2-12. Spectral mismatch between the global ASTM G173-03 reference spectrum (G03 Committee, 2012) and the step function interband absorbances of three different semiconductors: a) c-Si b) CdTe c) a-Si.

2.3.4 Recombination

In thermal equilibrium, the valence band and the conduction band of a semiconductor material have an equivalent chemical potential, the so called Fermi level. In other words, carriers' energy levels follow a single equilibrium probability distribution both in the valence band and in the conduction band. Due to the light-induced excitation of electrons, carrier concentrations change in the two bands and consequently, the chemical potential for electrons is deviated from its thermal equilibrium and two separate distributions evolve. The excitation changes the chemical potentials of both bands and the resulting electrochemical potential difference between the new quasi Fermi levels translates to the entropy free energy per an EHP μ_{ehp} . This electrochemical potential difference is the source of the voltage across an operational solar cell. The charge carriers, electron-hole gas, can be assumed to behave like ideal gas under radiation of moderate intensity i.e. for concentration ratios of less than approximately 1000 (Markvart, 2010, p. 57). In these conditions as in Eq. 2.9, μ_{ehp} can be expressed as a function of E_g , the effective densities of states in the conduction band N_c and the valence band N_v , and the carrier concentrations n_e and n_h in the bands, respectively (Würfel, 2005, p. 57).

$$\mu_{\text{ehp}} = eV_{ph} = E_g - kT_c \left[\ln \left(\frac{N_c}{n_e} \right) + \ln \left(\frac{N_v}{n_h} \right) \right] \quad (2.9)$$

As can be seen from Eq. 2.9, the quasi Fermi level separation μ_{ehp} is the wider, the higher the concentration of the photogenerated charge carriers is. Based on Eq. 2.9, it can be noted that μ_{ehp} reaches E_g in absolute zero ($T_c = 0$ K) or when all the valence electrons have been excited into the conduction band ($N_v = n_h$) and the conduction band is fully occupied ($N_c = n_e$). According to the third law of thermodynamics, absolute zero cannot be reached by any procedure (Guggenheim, 1949, p. 157). On the other hand, Kirchhoff's law of thermal radiation indicates that any body with a nonzero absorptivity is also an emitter. In other words, if the transition of an electron from the valence band to the conduction band due to photon absorption is possible, the probability of photon emission due to the opposite transition cannot be zero, either. Hence, the latter process cannot be avoided in solar cells even in theory. Consequently, the second condition of fully occupied bands is thermodynamically impossible and μ_{ehp} can, therefore, not reach E_g .

The second law of thermodynamics, too, indicates that thermalisation is not the only loss mechanism associated with charge carrier generation. Carrier generation through interband absorption can be understood as a thermodynamic cycle in which thermal energy of the Sun radiated to the Earth's surface is converted into chemical energy in a solar cell. Solar cells can be thought of as heat engines with electron-hole gas as the working substance. Carrier thermalisation is the first step of the process. The hot carriers

excited by photons cool down to the band edge through transferring their excess energy to lattice vibrations. As illustrated in Figure 2-1, thermalisation does not occur in the case of a photon with an energy level equivalent to E_g . If the entire energy of the photon was converted into chemical energy, the process would be in contradiction with the second law of thermodynamics. The law implies that not all of the heat input to a heat engine can be converted into work. The maximum is determined by the Carnot cycle efficiency η_C , which can be formulated in this context as follows:

$$\eta_C = 1 - \frac{T_c}{T_s}, \quad (2.10)$$

where T_s stands for the temperature of the Sun.

In addition to the inevitable loss of thermal energy to the surroundings, μ_{ehp} is reduced by the irreversible entropy generation involved in the conversion process. As implied by Eq. 2.9, these losses are dependent on the concentration of charge carriers. Both the Carnot factor-related loss of thermal energy and the loss of free energy due to increased entropy generation occur through two fundamentally unavoidable processes reducing the concentration of EHPs in operational solar cells. One is known as recombination, which is introduced in the context of the Shockley equation in section 2.2.1, and the other one is due to charge carrier collection leading to the generation of charge current. As thermodynamically interdependent processes, both absorption and recombination together with current generation need to be considered in order to understand the entropy generation leading to the loss of free energy created through light-induced carrier thermalisation. Adapted from Markvart (2008a), Eq. 2.11 expresses μ_{ehp} as a linear combination of E_g and the changes in the thermal energy and the entropy of the carrier distribution.

$$\mu_{ehp} = E_g - E_g \frac{T_c}{T_s} + kT_c \left[\ln\left(\frac{T_s}{T_c}\right) - \ln\left(\frac{\Omega_{emit}}{\Omega_s \cos \theta_z}\right) + \ln(\eta_{emit}) - \ln\left(\frac{I_{ph} + I_0}{I_{ph} + I_0 - I}\right) \right], \quad (2.11)$$

where Ω_s and Ω_{emit} stand for the solid angles of the Sun and emission, respectively, and η_{emit} the photon emission efficiency. The second term accounts for the Carnot cycle loss i.e. the unavoidable loss of thermal energy to the surroundings. The third term, which comprises four logarithmic components, represents the increase in entropy due to the irreversible processes involved in photovoltaic conversion. The first component of the third term is positive and, therefore, involves reduction in the entropy of the carrier distribution. This increase in the free energy per carrier is due to the transfer of entropy to the lattice during thermalisation. As Eq. 2.9, the formulation of the component is an ideal gas simplification for incident radiation of moderate intensity (Markvart, 2008b). The second component represents the increase of entropy due to increasing availability of photon states during the conversion of radiant energy into chemical energy through carrier generation and back to radiant energy through radiative recombination. The reason is the discrepancy between the solid angles of heliocentric absorption and hemispherical emission that are typical of PV conversion in conventional flat-plate modules. The third component of the entropy generation term addresses the annihilation of charge carriers through non-radiative recombination. The resulting reduction in carrier concentration narrows μ_{ehp} as implied by Eq. 2.9. Similarly, the fourth component expresses the impact of the drop in carrier concentration due to the separation of the charge carriers and the consequent generation of charge current.

As discussed above, either charge carriers can be separated and collected at the opposite contacts of the cell thus generating charge current or they recombine before reaching the contacts. As shown in Figure 2-7, recombination causes a drop in voltage through reducing μ_{ehp} as well as a drop in current through the annihilation of charge carriers. Recombination mechanisms are classified according to the

process through which the energy of an EHP is dissipated. In radiative recombination, charge carriers are destroyed through a process opposite to excitation. In practice, a conduction electron is relaxed to the valence band and the energy approximately corresponding to the band transition is emitted as a photon. Radiative recombination is a significant loss process in the case of thin-film devices as they consist of semiconductor layers with direct band gaps. In the case of indirect band gap materials such as crystalline silicon however, radiative recombination is less probable since relaxation that is synchronously assisted by several phonons is required for the emission to occur. The photons generated by radiative recombination may be reabsorbed and hence, increasing cell thickness (up to a certain limit) reduces the proportion of the losses caused by the process (Brendel and Queisser, 1993). Current and voltage losses are only incurred in case photons are emitted through the top surface.

In silicon wafer-based solar cells, recombination mainly occurs through a non-radiative pathway (Green, 1984). In this process, the energy of EHPs is transferred to free carriers and phonons. The free carrier-assisted recombination mechanism is referred to as Auger recombination whereas the mechanism based on heat dissipation to the lattice solely via trap energy levels is known as multi-phonon recombination or, more commonly, Shockley-Read-Hall (SRH) recombination. In Auger recombination, the energy released by recombining carriers is captured by free carriers, which are first excited to a higher energy level but eventually lose the absorbed energy through phonon-assisted relaxation as in the case of FCA. As radiative recombination, Auger recombination is an intrinsic loss mechanism and, thus, practically unavoidable. Auger recombination is particularly significant at high levels of carrier concentration. By contrast, SRH recombination is typically dominant in all industrial solar cells when the carrier concentration is low. Its probability is determined by a trap energy level caused by an impurity or a material interface such as a surface or a grain boundary. SRH recombination reaches its maximum when the trap level is located in the middle of the band gap and sharply decreases as the level approaches either of the band edges. This is due to the shapes of the energy distribution of the electrons in the conduction band and that of the holes in the valence band. Since the impurities of industrial solar cells mostly consist of dopants whose energy levels are near the band edges in the quasi-neutral regions, SRH recombination mostly occurs within the SCR or at the material interfaces. Since SRH recombination occurs via impurities or surface states, it can be, in theory, avoided for the most part when using highly pure semiconductor materials and surface passivation. Therefore, it is an extrinsic loss pathway. Also, the long-term degradation in PV performance through increased recombination is mostly due to a growing number of defect states caused by cell cracking and water ingress-induced oxidation (Honsberg and Bowden, 2014). In contrast to the radiative pathway, non-radiative recombination rates are directly proportional to cell thickness (Brendel and Queisser, 1993).

The recombination current in an operational solar cell can be approximated by Eq. 2.2. This equation, however, applies to an ideal solar cell where only interband recombination takes place. In the double diode equivalent circuit model already mentioned in section 2.2.1 and expressed in Eq. 2.12, it is assumed that recombination occurs in two different ways and accordingly, the different recombination mechanisms are modelled through two different sets of diodes connected in parallel.

$$I(V) = I_{0,1} \left[\exp \left(\frac{e(V - IR_s)}{kT_c} \right) - 1 \right] + I_{0,2} \left[\exp \left(\frac{e(V - IR_s)}{2kT_c} \right) - 1 \right] - I_{ph} + \frac{V - IR_s}{R_p} \quad (2.12)$$

In Eq. 2.12, the diode current term of Eq. 2.4 (single diode model) has been replaced by two current terms representing two different carrier transition mechanisms. The first term stands for the diode current component caused by interband recombination and interband thermal generation $I_{0,1}$. Interband

recombination can occur through the radiative or the Auger mechanisms and, with much less probability, via impurities (SRH) in the quasi-neutral regions where the trap levels are close to the band edges. Hence, the diode current component can be modelled by means of a single diode parallel to the source of I_{ph} and with the entire V_{ph} ($V - IR_s$) across its terminals.

The second term represents the diode current component arising from multi-phonon recombination and generation $I_{0,2}$ (SRH) within the SCR. In the model, all SCR recombination is assumed to take place via trap levels right in the middle of the band gap so that individual carrier transitions involve energy corresponding to $V_{ph}/2$. Accordingly, in the equivalent circuit diagram, two series-connected diodes with the reverse saturation current $I_{0,2}$ are connected parallel to the current source and to the single diode with the saturation current $I_{0,1}$ in order to make the voltage across the diode terminals equal to $V_{ph}/2$. Alternatively, the concept of diode ideality factor n_d is often used. In this case, the equivalent circuit diagram has simply two single diodes, one with n_d of 1 and the other with n_d of 2, connected parallel to each other and the current source.

In open circuit, recombination reaches its maximum as then, it roughly equals generation (see section 2.2.1). Conversely, minimal recombination occurs in short circuit conditions where in the case of an ideal solar cell, I_d is zero. Although in real solar cells, recombination also reduces I_{sc} , its effect on V_{oc} is much stronger as can be seen from Figure 2-7. Consequently, V_{oc} is usually expressed as a function of I_0 (Eq. 2.5) while I_{sc} is commonly assumed to be mostly dependent on optical parameters. As mentioned in section 2.2.1, I_0 is influenced by T_c . This is due to the link between T_c and intrinsic carrier concentration n_i , which in turn determines thermal generation (I_0) together with material quality-related parameters. Increasing temperature results in higher I_0 and, consequently, in more recombination as shown in Shockley equation (Eq. 2.3). As a result, μ_{ehp} is narrowed thus reducing V_{ph} . In spite of the rather complex temperature dependence of I_0 , μ_{ehp} has been found to have a negative, approximately linear relationship with T_c (Wu and Chen, 1982). The slope of this dependence is contingent upon the difference between E_g and μ_{ehp} , which, in fixed ambient conditions, is mainly affected by doping and material purity. This temperature dependence is the most important impact that T_c has on PV performance in all semiconductor-based PV devices. As discussed in section 2.3.1, rising temperature decreases optical losses due to reducing E_g . The positive effect on current is outweighed, however, by the negative effect on voltage through increasing I_0 and, to a less extent, recombination-induced current drop and higher thermalisation losses. The temperature dependence of a PV material is mostly dependent on E_g and material quality and therefore, the performances of solar cells made of different materials decrease at different rates with increasing T_c . Intrinsic carrier concentration is inversely exponentially proportional to E_g . Consequently, the higher E_g a PV material has, the lower voltage drop is incurred due to increasing T_c unless worse material quality compensates the effect.

Irradiance influences recombination via two pathways. The primary one is expressed in the Boltzmann approximation (Eq. 2.2). It follows from the equation that via I_{ph} , V_{ph} is logarithmically proportional to the part of W_{poa} that is absorbed by the PV material, W_{abs} . According to Eq. 2.9, this means that with increasing W_{abs} , I_{rec} is reduced relative to I_{ph} leading to the growth of carrier concentrations and higher V_{ph} . I_{ph} and I_{rec} become comparable only at irradiance levels too low to be observed with conventional instruments (Würfel, 2005, p. 151). Accordingly, the recombination-incurred voltage drop is reduced in spite of the fact that I_{rec} increases. In Eq. 2.11, this phenomenon is attributed to a reduction in entropy generation due to the lowered discrepancy between the solid angles of heliocentric absorption and hemispherical emission. The second pathway, light soaking, is highly material-dependent and depends on

the duration of light exposure. Light soaking effects refer to the generation or annihilation of metastable trap energy levels due to the heat dissipated through increased I_{rec} . In the case of the silicon-based materials, c-Si, a-Si, and a-Si/ $\mu\text{c-Si}$, light soaking is known to increase the number of trap levels and, consequently, intensify SRH recombination. Perhaps, the best-known light-induced degradation mechanism is the Staebler-Wronski effect (Staebler and Wronski, 1980). The effect involves the recombination-induced breakage of weak Si-Si bonds in amorphous silicon. A similar process has been identified with boron-oxygen bonds in boron-doped monocrystalline silicon (Schmidt, 2004). In the case of the non-silicon-based PV materials, CdTe, CIS, and CIGS, light soaking tends to improve performance. The exact mechanism how light soaking reduces recombination in these materials is not known. The metastable selenium-copper divacancies are currently considered as the most likely pathway in the case of CIS and CIGS materials (Igalson et al., 2009). The light soaking effects have been shown to be mostly reversible in that dark exposure or thermal annealing normally reverses the effects. For instance, the performance of a-Si cells is commonly known to improve when exposed to very high operating temperatures because of the reverse Staebler-Wronski effect. However, some authors have identified light-induced long-term degradation through permanently increased recombination via trap levels in CdTe devices. This effect has been linked to the diffusion of copper ions from the back contact into the absorber (Corwine et al., 2004).

The impacts of T_c and W_{abs} on carrier recombination are highly dependent on ambient conditions. When the conditions experience variability within the site, also performance varies between modules and arrays. As per Kirchhoff's circuit laws however, an equivalent current flows through series-connected modules and voltage has to be the same across all parallel-connected strings or arrays. Consequently, the modules exposed to more favourable conditions suffer from an additional recombination-induced current drop relative to their MPP conditions in order to reach the current level of the modules affected by less favourable conditions. This phenomenon can also occur between the cells of a single module and even the different photovoltaic layers of multijunction solar cells due to variation in the solar spectrum. In the case of a severe discrepancy between the conditions, the poorly performing modules can also be bypassed in order to avoid the detrimental heating due to the strong negative bias caused by the other modules (Meyer and Van Dyk, 2004). This, too, leads to a recombination-induced current drop in the other modules because both affected and unaffected strings or arrays have to run at a single voltage due to the parallel connection. Similarly to ambient conditions, inherent differences between the performance parameters of installed modules cause mismatch effects. Small discrepancies in the parameters of industrially manufactured and deployed solar modules are practically unavoidable. The mismatch losses can be fully avoided only if MPP tracking is performed separately for every p-n junction. However, the imperfect accuracy of MPP trackers contributes to the relative recombination losses to a small extent even in the complete absence of mismatch effects.

2.3.5 Parasitic Losses

In this thesis, the term parasitic loss processes is used to refer to all the losses involved in PV power generation that cannot be regarded as optical losses, carrier thermalisation, or recombination. These losses comprise four loss categories: ohmic losses, leakage currents i.e. shunt losses, power conversion-related losses, and the self-consumption of the power station. Ohmic losses and leakage currents have a direct impact on recombination because they influence the concentration and energy distribution of charge carriers (see Eq. 2.9 and Eq. 2.12). Furthermore, they indirectly affect also optical losses and carrier thermalisation as they influence E_g via T_c . As discussed in section 2.2.1 however, parasitic losses are not considered when modelling an ideal solar cell. The parasitic loss processes included in Figure 2-7 comprise only the ones occurring on the DC side of the power station: ohmic losses and leakage currents.

Ohmic losses stand for the voltage drop processes caused by Joule heating in conductors due to flow of current. The effect of conductor Joule heating is often quantified by means of two resistance parameters: the series resistance of solar cells or modules, R_s , and the resistance of the conductors that further transmit current via power conversion units to the grid. A single lumped R_s is normally used to account for the combined resistance of all parts of the cell that are located on the current path from the p-n junction to the contact terminals: SCR, quasi-neutral regions, and rear and front contacts, as well as wiring in the case of modules. The resistivities of the above cell elements differ from each other and experience even local variability within the elements (Breitenstein and Rißland, 2013). This variation has been found to cause problems particularly in the estimation of the temperature dependence of R_s . As per Sabry and Ghitas's (2007) measurements, the different methods having been used to estimate the temperature dependence based on measured data give widely scattered and even contradicting results – even among modules representing a single PV material (Arora et al., 1986; Ding et al., 2005; Singh et al., 2008). Probably, that is one of the main reasons why the temperature dependence of R_s is not considered in most models. The studies on the irradiance dependence of R_s have produced more consistent results implying that R_s is inversely proportional to W_{abs} in the case of most PV devices (Arora et al., 1986; Bätzner et al., 2001; Khan et al., 2010; Li et al., 2014; Priyanka et al., 2007; Reich et al., 2009; Van Dyk and Meyer, 2004; Virtuani et al., 2003). Arora et al. (1986) link the dependence to the increase of carrier concentrations with irradiance and the consequent improvement in conductivity. However, as the voltage drop caused by R_s quadratically increases with current, rising irradiance normally increases the share of the ohmic loss processes of the total parasitic losses. Some of the most common long-term degradation mechanisms influencing solar modules are related to increasing R_s . These mechanisms are mostly related to water ingress-induced electrochemical corrosion and the weakened adherence of contact elements due to thermo-mechanical fatigue (Carlsson and Brinkman, 2006; Honsberg and Bowden, 2014).

The resistivity of metallic conductors can be modelled in a more straightforward way than that of semiconductor and TCO materials. Rising temperature, for instance, is normally assumed to cause a linear relative decrease in the resistance of metals. However, as the temperature of a conductor is an outcome of rather complex heat transfer exchange with its surroundings, the resistivity of wires and cables is commonly assumed not to have dependence on temperature or any other ambient parameter in the context of PV power stations. The two most important factors influencing Joule heating in wires are actually the array configuration and scale of the power station. As ohmic losses increase quadratically with current, the high-band gap PV materials characterised by low currents and high voltages would be more optimal from the viewpoint of transmission losses. With the current range of commercially available module types however, this advantage is compensated by the lower efficiencies typically obtained with these materials. Module types with lower efficiencies lead to higher ohmic losses because transmission losses depend linearly on the length of the wire run. Through cable selection, voltage drops across cable runs are normally limited to a few percent in today's power stations. The cabling optimisation is strongly influenced by the plant's cost structure.

The other parasitic loss mechanism occurring at the cell level is the leakage current caused by shunts present in real solar cells. Shunts are manufacturing defects that provide charge carriers with a path alternative to the one through the p-n junction. The resulting leakage current does not contribute to the power output of the cell and leads to a current drop. In general, thin-film modules suffer from higher leakage currents than the wafer-based ones due to the scribing-based cell structuring. They are more prone to shunt formation also because the contacts are much nearer each other than in wafer-based cells. As shown in Figure 2-7, the sample a-Si modules are estimated to incur shunt losses three times higher than

those of the c-Si modules in spite of the almost 60% lower W_{abs} . In contrast to R_s , shunt conductance ($1/R_p$) has consistently been identified to have a positive temperature dependence (Banerjee and Anderson, 1986; Dongaonkar et al., 2010; Singh et al., 2008). Although the dependence has been found to be weak compared to that of I_0 (see section 2.3.4) (Dongaonkar et al., 2010; Singh et al., 2008), Singh et al. (2008) suggest that in the case of materials with low R_p and high E_g levels such as a-Si, shunt conductance is likely to have a notable impact on the temperature dependence of the overall power output of the cell. The irradiance dependence of shunt conductance is found to be positive by many authors (e.g. Bätzner et al., 2001; Virtuani et al., 2003) but is not supported by as concordant evidence as the temperature dependence. Khan et al. (2010) suggest that the reason for discrepancies might lie in the different light soaking properties of PV materials. The trap energy levels causing the light soaking effects in some materials may effectively act as shunts and, thereby, deviate the irradiance dependence of shunt conductance from its generally expected pattern. Nevertheless, irrespective of the sort of the irradiance dependence, the shunt losses' share of the total losses tends to increase at low irradiance levels. This is due to the fact that decreasing irradiance reduces I_{sc} linearly but V_{oc} logarithmically (see section 2.3.4) and, as a result, the ratio of V_{mpp} to I_{mpp} i.e. the characteristic resistance of a solar cell increases. When the characteristic resistance is equal to R_p , leakage current represents half of I_{ph} . In such a situation, η_c has experienced a dramatic drop and the I-V characteristic curve of the cell looks like a straight line. Accordingly, the lower R_p is, the higher irradiance levels are required to keep the solar cell in the diode mode instead of the shunt mode (Bunea et al., 2006). Hence, as shown e.g. by Rummel and McMahon (1996) and Bunea et al. (2006), shunt conductance has a significant impact on the low light performance of solar cells. The metal migration discussed in association with recombination losses also increases shunt losses in the long run. The metal ions diffusing from the front and back contacts change the effective doping levels locally and thereby offer alternative paths for charge carriers (Dongaonkar et al., 2011). Module short circuits through which current flows to the grounded module frame can also develop through delamination, cracking, or corrosion (Honsberg and Bowden, 2014). According to Hacke et al. (2011), high system operating voltages contribute to the probability of such shunt formation.

Figure 2-13 presents the variation of I_{mpp} , V_{mpp} , and η_{mpp} of four different module types with changing cell temperature and irradiance. The curves are modelled by means of Photovoltaic Array Performance Model of Sandia National Laboratories (SNL) (King et al., 2004) (hereafter referred to as the Sandia PV Array Performance Model) based on parameters derived from SNL's and Photon Magazine's own field measurements (PVsyst SA, 2014a; Sandia National Laboratories, 2014a). Being based on real measurements, Figure 2-13 helps to understand how the aforementioned ambient effects on PV loss processes work together in the determination of module performance in actual operating conditions. The operating conditions particularly relevant for power generation in Abu Dhabi, UAE have been highlighted in the figure.

In the PV industry, it is a common practice to approximate the overall effect of T_c on module output by means of the temperature coefficient of P_{mpp} or η_{mpp} . The coefficient is based on the assumption that the relative difference between P_{mpp} and the STC power output $P_{\text{mpp,STC}}$ is linearly dependent on the absolute difference between T_c and the STC cell temperature $T_{c,\text{STC}}$. This coefficient is supposed to account for all effects that changing T_c poses on module performance – most importantly the resulting changes in I_0 (recombination), E_g (optical losses and thermalisation), and R_p (shunt losses). The performances of the module types analysed in Figure 2-13 show a strong linear dependence on T_c . This implies that in the case of all four modules, the temperature dependence is dominated by recombination closely following the Boltzmann approximation (Eq. 2.2). Potential curvature due to the inverse light soaking effect, for instance,

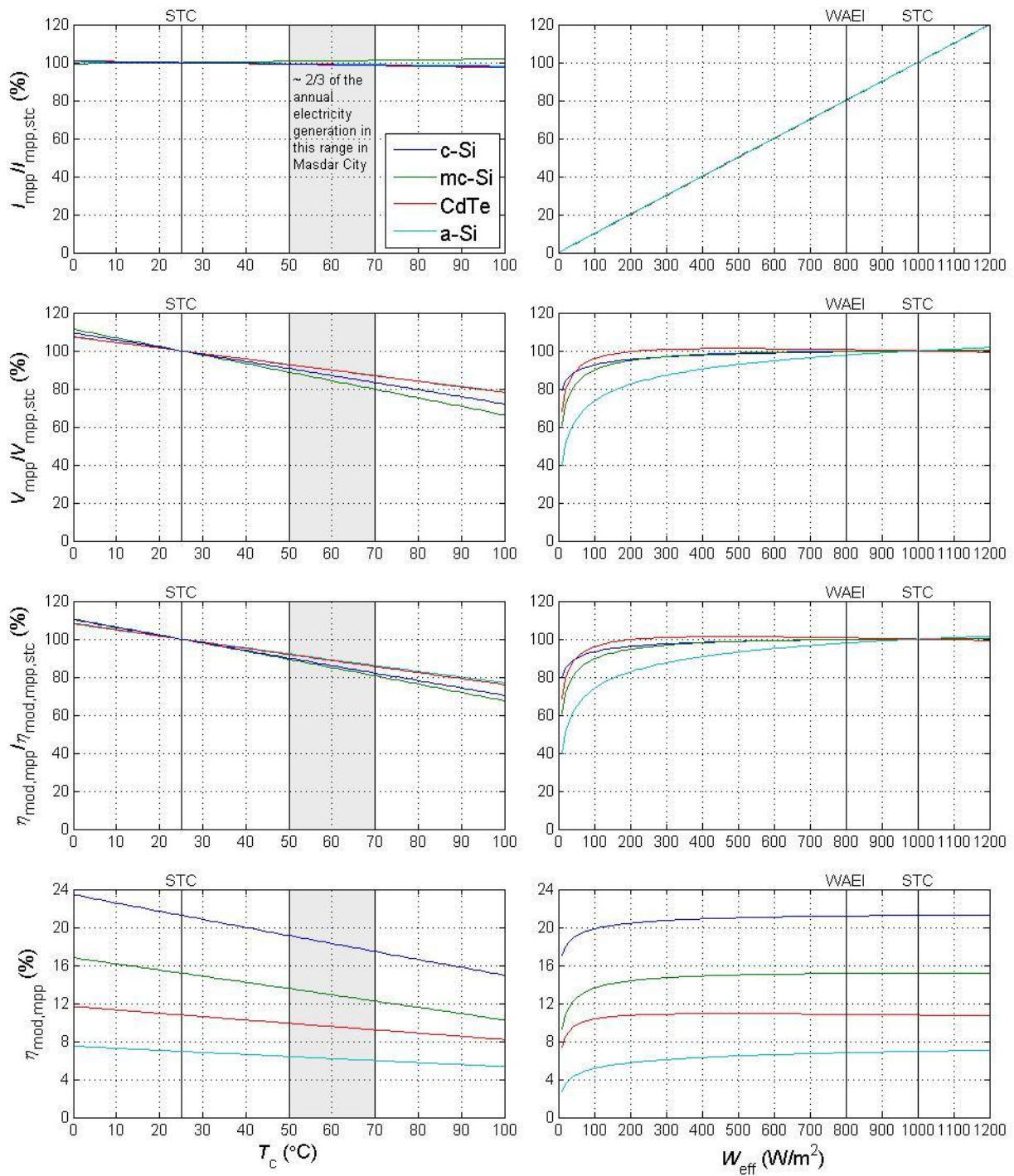


Figure 2-13. Temperature and irradiance dependences of the performance parameters of four sample modules included in the Sandia Modules library (Sandia National Laboratories, 2014a) or PVsyst’s module database (PVsyst SA, 2014a): SunPower SPR-305-WHT (c-Si), Suntech Power STP200S-18-ub-1 (mc-Si), First Solar FS-272 (CdTe), and Kaneka TSC120 (a-Si). Simulated using Photovoltaic Array Performance Model (King et al., 2004) of Sandia National Laboratories (SNL) based on field-measured performance data collected by SNL (c-Si, mc-Si, and CdTe) and Photon Magazine (a-Si) (PVsyst SA, 2014a). WAEI stands for the approximate output power-weighted hourly average effective irradiance in Masdar City.

cannot be identified even in the case of the a-Si module. This can be explained by the comparatively poor cell material quality of the a-Si module in question. While the CdTe module’s cell-specific V_{oc} is 56% (0.82 V/1.45 V) of the band gap voltage, the percentage is only 44% (0.77 V/1.72 V) in the case of the a-Si

module. As a result, the a-Si module's negative temperature dependence is higher than the dependence implied by its E_g . This leads to a performance pattern only slightly better than that of the CdTe module. The direct proportionality of the STC normalised I_{mpp} to T_c in the case of the mc-Si module implies a stronger positive temperature dependence of R_s than in the case of the other modules. This would explain the module's solely voltage-driven power degradation due to rising T_c .

The irradiance dependence of module performance is analysed in Figure 2-13 by plotting the performance parameters against effective irradiance W_{eff} . W_{eff} is adapted from W_{poa} such that I_{sc} is always linearly dependent on it. As discussed in section 2.3.2, a change in the electromagnetic spectrum incident on a module alters the performance of the module – even if W_{poa} remains constant. Similarly, conditions with equivalent POA intensities result in higher optical losses with increasing ϑ due to intensified reflection. In W_{eff} , the effects of changing spectrum, angular losses, and soiling are isolated by normalising $W_{poa,STC}$ by the ratio of I_{sc} to $I_{sc,STC}$. Accordingly, W_{eff} is equal to W_{poa} at STC. The modules analysed in Figure 2-13 experience a linear increase also in I_{mpp} with increasing W_{eff} . This implies that the effect of increasing I_{rec} is negligibly low compared to the increase in I_{ph} . Also, the shunt conductance of all the modules seems to be sufficiently low not to cause I_{mpp} to deviate from the linear pattern at low W_{eff} levels. The low material purity level of the a-Si module and the resulting short carrier lifetime are probably the reasons for the module's poor low light performance. The other three modules retain their voltage levels well down to 100 W/m². V_{mpp} of the mc-Si module drops first probably due to the module's higher shunt conductance. The reason for the CdTe module performing better at 500 W/m² than at 1000 W/m² is likely to be related to a relatively high R_s , which results in a voltage drop at irradiance levels exceeding 600 W/m² due to the quadratically increasing ohmic losses. Amongst the four module types, the CdTe module appears to represent the most suitable technology for the hot desert conditions of Abu Dhabi due to its weaker temperature dependence and good low light performance.

The equipment used for power conversion and conditioning, solar inverters and transformers, represents a small share of the total losses involved in PV power generation in normal operating conditions. In extreme conditions however, they might become a significant loss factor. Under hot desert climates, such conditions are typically caused by high T_c levels. Apart from technological parameters, inverter performance is generally influenced by instantaneous power levels and DC input voltage. High T_c may reduce V_{mpp} so much that the minimum system voltage level for the inverter to run is not reached. In such a situation, the modules are first forced down on their I-V characteristic curves in order to increase system voltage levels. In the most severe cases, the plant stops feeding electricity to the grid and is actually consuming power regardless of the irradiance levels incident on arrays. In order to minimise the number of daylight hours spent outside the operational range of the inverter, the number of modules in an array should be maximised within the range defined by the inverter's maximum voltage requirements. Another possible remedy is a DC-AC loading ratio higher than 100%, in which case inverters are dimensioned so that their capacity is lower than the combined module capacity connected to it. From the inverter performance point of view, the problem involved in the above design choices is the inverse proportionality of inverter efficiency to system voltage. Inverter performance can be described by an efficiency curve. An example of such a curve is shown in Figure 2-14. As can be seen from the curve, the performance of the inverter has been optimised for an instantaneous array-to-inverter power ratio of 30%-50% depending on the system voltage. The lower the voltage level, the better is the performance of the inverter. Therefore, a high loading ratio would ensure steadier plant performance but concentrate most of the hours of high generation out of the inverter's highest-efficiency range. On the other hand, with a low loading ratio, the dramatic drop in

inverter efficiency becomes more probable also during the day although the inverter would operate at a higher efficiency on average.

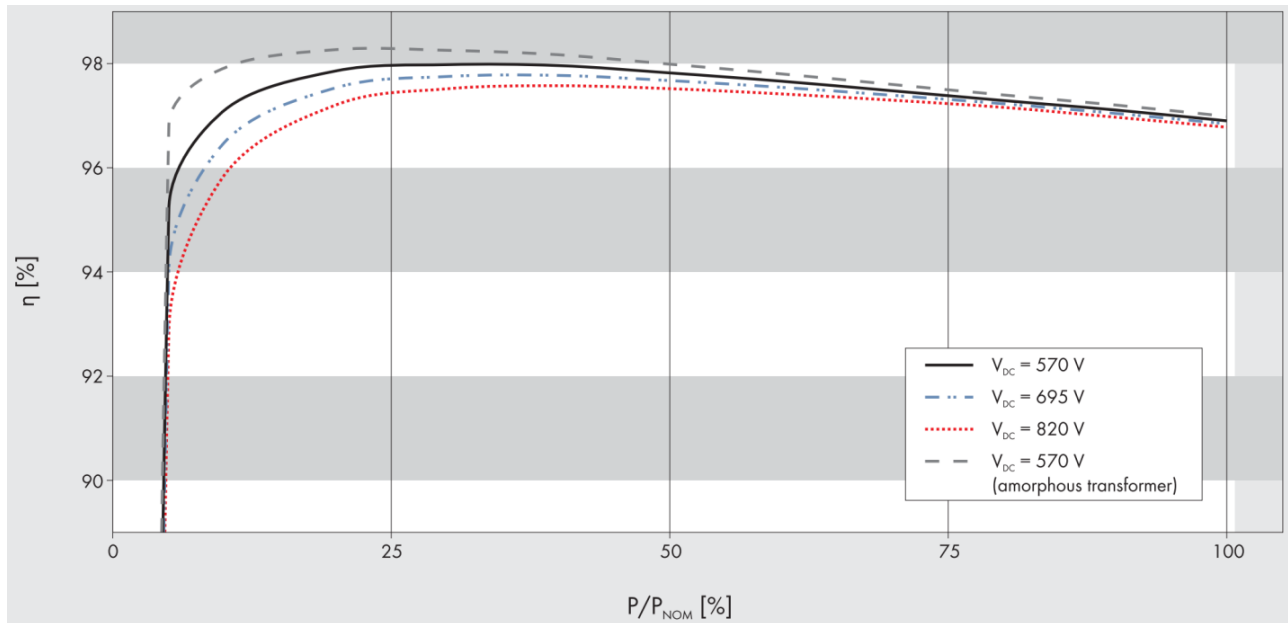


Figure 2-14. Efficiency curve of SMA SUNNY CENTRAL 1600 MV. (SMA Solar Technology AG, 2014).

PV power stations located in hot regions suffer from comparatively high parasitic self-consumption due to the need to cool inverters in order to avoid heat-induced performance degradation in power conversion. Otherwise, the parasitic loads are generated by inverters, monitoring systems, and solar tracking systems. The availability of data on the parasitic self-consumption of PV power stations is particularly poor in the case of hot desert conditions and therefore, the topic should be further studied before making conclusions about the effect of parasitic loads on PV performance in the context of this thesis.

3. Performance Modelling of Photovoltaic Power Stations

In order to design a PV performance simulation tool specific to a local environment, it is important to first develop a comprehensive general understanding of the existing models and relations relevant for the modelling objective. The literature review presented in this chapter, therefore, addresses each simulation step by discussing its purpose and the techniques involved. At the general level, the simulation process can be divided into four high level modelling tasks as done in Figure 3-1: optical modelling, spectral modelling, thermal modelling, and electrical modelling. The first three steps generate inputs for the electrical model, which produces the power output of the power station, P_{ac} , as the final simulation outcome. The chapter is structured based on the high-level modelling steps presented in Figure 3-1. Section 3.3, which discusses the general aspects of thermal modelling, also includes a summary of Tuomiranta's et al. (2013) paper on the validation of thermal models for solar cells in Abu Dhabi, UAE and presented at ISES Solar World Congress in Cancún, Mexico in 2013.

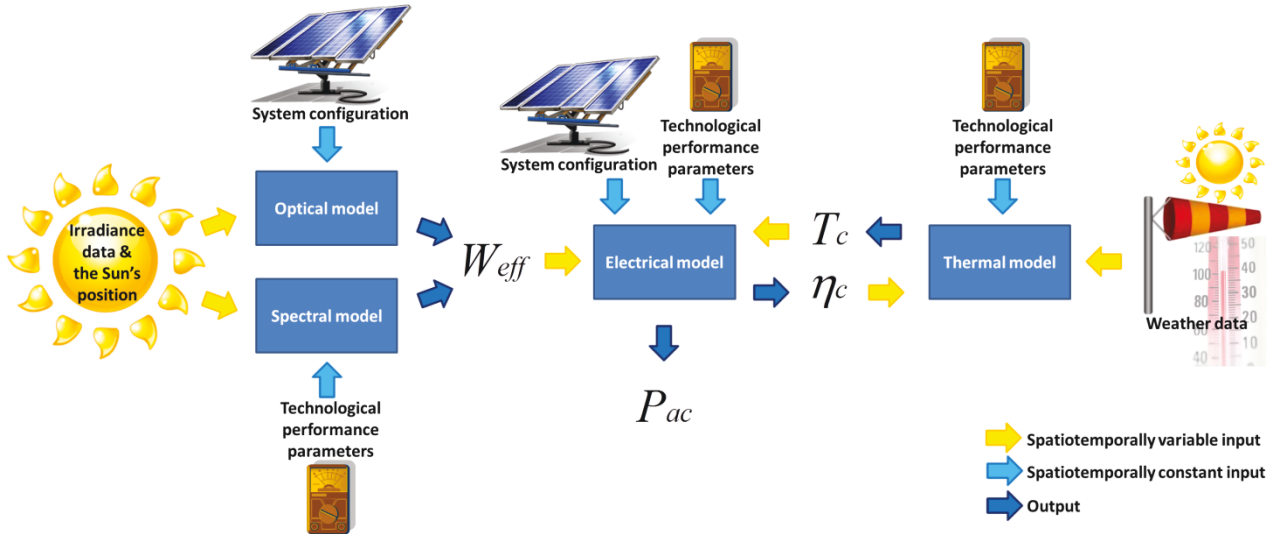


Figure 3-1. Steps involved in modelling the power output P_{ac} of a PV power station.

3.1 Optical Modelling

In this thesis, the purpose of an optical model is defined as the conversion of irradiance and solar position data into the broadband irradiance absorbed by solar modules. Therefore, the output of an optical model is W_{eff} in case the spectral distribution of the incident sunlight matches that of the standard spectrum (G03 Committee, 2012) and the attenuation due to angular reflection and soiling is spectrally neutral. The first step of the optical modelling process, the estimation of W_{poa} , is discussed in the first subsection and the methods used in the modelling of angular reflection and soiling losses in the second subsection.

3.1.1 Irradiance Transposition

Conventionally, the extent of solar radiation on the ground of the Earth is described through three measures of radiant flux density: direct normal irradiance (DNI), diffuse horizontal irradiance (DHI), and global horizontal irradiance (GHI). DNI stands for the flux density of the photons radiated from the sun disk onto a plane perpendicular to the beam propagation. Accordingly, it is also referred to as beam normal irradiance. DHI accounts for the photons from all the other parts of the sky incident on a horizontal plane i.e. a plane perpendicular to the line from POA to the zenith. DNI approximates the level of unscattered

irradiance, whereas DHI is used as an estimate for the incident irradiance affected by atmospheric scattering. GHI is the sum of DHI and horizontally transposed DNI ($DNI \cdot \cos \vartheta_z$).

In addition to the basic irradiance data, parameters defining the Sun's position with respect to POA are required for every time step and location in order to compute W_{poa} . Two solar angles are used for this purpose: solar zenith angle ϑ_z and solar azimuth angle φ_s . ϑ_z stands for the angle between the straight lines from POA to the Sun and to the zenith. Its complementary angle is referred to as the solar elevation angle. φ_s gives the Sun's horizontal direction with respect to the observer. In the context of PV performance assessment, it is often defined as the angle between the line from POA to the closer end of the Earth's axis and the horizontal projection of the line from POA to the Sun, thus, reaching 180° at solar noon. As discussed in section 2.3.1, the Earth-Sun distance also varies with time and is required for the computation of the irradiance at the top of the Earth's atmosphere. This extraterrestrial irradiance is used in irradiance decomposition and can also be employed in irradiance transposition. There are multiple models available for the estimation of the Sun's position. National Renewable Energy Laboratory's (NREL) Sun Position Algorithm (Reda and Andreas, 2008) is considered as the state of the art in terms of accuracy, whereas the Solar Geometry 2 algorithm (SG2) (Blanc and Wald, 2012) of MINES ParisTech provides a much higher computation speed with a slightly lower accuracy. Other algorithms include the ones developed by Grena (2008), Blanco-Muriel et al. (2001), Michalsky (1988), and Duffie and Beckman (2006, pp. 15–16).

In the case of an array installed with horizontal fixed mount (POA facing the zenith), GHI represents W_{poa} . In all other cases however, a transposition model is required in order to compute W_{poa} based on the three basic irradiance measures. Alternatively, global irradiance can be measured on a tilted surface and, thus, directly obtain W_{poa} for the specific POA tilt angle. This is a good option if the optical model is used in simulating the performance of a single plant design with a fixed POA angle. If the tilt angle is intended to be a variable input instead, the global irradiance measurements should be made on a horizontal surface and converted into W_{poa} by means of a transposition model. If irradiance measurements only consist of GHI observations, as is the case with an ordinary pyranometer, a decomposition model can be used to deduce the other two irradiance components. Several such models have been proposed and validated for different sets of independent variables (e.g. Erbs et al., 1982; Maxwell et al., 1987; Orgill and Hollands, 1977; Reindl et al., 1990a).

Transposition models normally use all the three irradiance measures to address photon fluxes radiated from different directions. Accordingly, they divide the incident irradiance into direct, sky diffuse, and ground-reflected components. Eq. 3.1 shows the general form of such models.

$$W_{poa} = W_{b,n} \cdot \cos \theta + W_{d,h} \cdot R_d + \rho \cdot W_{g,h} \cdot R_r \quad (3.1)$$

where $W_{b,n}$ stands for DNI, $W_{d,h}$ for DHI, and $W_{g,h}$ for GHI. Ground-reflected irradiance is normally approximated by multiplying GHI by the albedo ρ i.e. reflection coefficient of the land surface around the array. Each of the three irradiance estimates (DNI, DHI, and $\rho \cdot GHI$) is multiplied by its respective transposition factor. As the contribution of the ground-reflected component is comparatively small most of the time, the irradiance reflected from the ground is generally assumed to be isotropic i.e. it is not dependent on the direction it is radiated from. This isotropic transposition factor in the case of ground-reflected irradiance can be formulated as follows:

$$R_r = \frac{1 - \cos \beta}{2}, \quad (3.2)$$

where β stands for the POA inclination angle. The cosine effect is usually considered to be the only factor

influencing the transposition of direct irradiance, for which reason DNI is simply multiplied by the cosine of the angle of incidence ϑ .

ϑ can be calculated for a fixed, equator-oriented POA based on the solar angles and β as follows (Duffie and Beckman, 2006, p. 15):

$$\theta = \cos^{-1}(\cos \theta_z \cos \beta + \sin \theta_z \sin \beta \cos \varphi_s) \quad (3.3)$$

As discussed in section 2.2.2, single axis trackers turn POA such that ϑ is minimised. There are alternative ϑ optimisation formulae available for different levels of single axis tracking design complicity. Duffie and Beckman (2006, pp. 20–22) limit their analysis to horizontal, vertical, and polar aligned single axis trackers. Duffie and Beckman's work is extended to arbitrarily tilted single axis trackers by Braun and Mitchell (1983). Narvarte and Lorenzo (2008) develop models for arbitrarily tilted tracking geometries where POA does not need to be parallel to the axis, and Marion and Dobos (2013) remove the coupling between the optimum angle of axis rotation ω_{axis} and ϑ so that ω_{axis} can be computed independently. The equations of the different approaches to ϑ minimisation in the case of single axis tracking can be found in Appendix A. Dual axis trackers, in turn, continuously turn POA towards the Sun and, hence in theory, keep ϑ at zero degrees all the time.

As the simple formulations of the transposition factors of direct and ground-reflected irradiances are widely accepted as sufficiently good approximations, the different transposition models mostly vary in how they define the diffuse transposition factor R_d . At its simplest, R_d is the additive inverse of R_r in which case sky diffuse irradiance is assumed to be isotropic i.e. uniformly distributed over the sky dome (Hottel and Woertz, 1942). At least five different isotropic sky diffuse models have been proposed (Badescu, 2002; Jimenez and Castro, 1986; Koronakis, 1986; Liu and Jordan, 1961; Tian et al., 2001). As briefly implied at the end of section 2.3.1 however, the angular distribution of diffuse i.e. sky irradiance is characterised by increasing intensity in the vicinities of the Sun and the horizon. The first commonly recognised attempt to address the anisotropic distribution of sky diffuse irradiance is by Hay and Davies (1978), whose model for sky diffuse irradiance on a tilted, equator-oriented POA, $W_{d,\text{poa}}$, superimposes circumsolar radiation component on the isotropic sky irradiance. The model is expressed in Eq. 3.4.

$$W_{d,\text{poa}} = W_{d,h} \left[\frac{W_{b,n}}{W_{\text{toa},n}} \cos \theta + \frac{1 + \cos \beta}{2} \left(1 - \frac{W_{b,n}}{W_{\text{toa},n}} \right) \right], \quad (3.4)$$

where $W_{\text{toa},n}$ stands for the direct normal irradiance on the top of the atmosphere. In addition to circumsolar brightening, Klucher (1979) includes also a factor for horizontal brightening in his model expressed in Eq. 3.5.

$$W_{d,\text{poa}} = W_{d,h} \frac{1 + \cos \beta}{2} \left[1 + \left(1 - \left(\frac{W_{d,h}}{W_{g,h}} \right)^2 \right) \sin^3 \left(\frac{\beta}{2} \right) \right] \left[1 + \left(1 - \left(\frac{W_{d,h}}{W_{g,h}} \right)^2 \right) \cos^2 \theta \sin^3 \theta_z \right] \quad (3.5)$$

Reindl et al. (1990a, 1990b) adjust the Hay-Davies model by extending it to consider horizontal brightening as well. The resulting formula for $W_{d,\text{poa}}$ is shown in Eq. 3.6.

$$W_{d,\text{poa}} = W_{d,h} \left[\frac{W_{b,n}}{W_{\text{toa},n}} \cos \theta + \frac{1 + \cos \beta}{2} \left(1 - \frac{W_{b,n}}{W_{\text{toa},n}} \right) \left(1 + \sqrt{\frac{W_{b,n} \cos \theta_z}{W_{g,h}}} \sin^3 \left(\frac{\beta}{2} \right) \right) \right] \quad (3.6)$$

In order to improve the accuracy of $W_{d,\text{poa}}$ estimation, Perez et al. (1990, 1987) propose a semi-empirical, computationally more intensive model. As per Perez et al. (1990), the latest set of empirically derived

coefficients (Perez et al., 1990) provide good accuracies across the climatic range of the United States. The basic form of the Perez sky diffuse model is presented in Eq. 3.7.

$$W_{d,poa} = W_{d,h} \left[\frac{1 + \cos \beta}{2} (1 - F_1) + F_1 \frac{a}{b} + F_2 \sin(\beta) \right], \quad (3.7)$$

where

$$a = \max(0, \cos \theta)$$

$$b = \max(0.087, \cos \theta_z)$$

$$F_1 = \max \left(0, f_{11} + f_{12} \frac{W_{d,h}}{W_{toa,n}} m_r + f_{13} \theta_z \right)$$

$$F_2 = f_{21} + f_{22} \frac{W_{d,h}}{W_{toa,n}} m_r + f_{23} \theta_z$$

The coefficients f_{11} , f_{12} , f_{13} , f_{21} , f_{22} , and f_{23} are empirically derived for specific bins of the sky's clearness ϵ . ϵ is defined as follows:

$$\epsilon = \frac{\frac{W_{d,h} + W_{b,n}}{W_{d,h}} + 1.041 \theta_z^3}{1 + 1.041 \theta_z^3} \quad (3.8)$$

In Eq. 3.7-8, all angles are assumed to be in radians. Table 3-1 presents the values for the coefficients representative for eight different sky clearness levels.

Table 3-1. The Perez sky diffuse model coefficients for different levels of sky clearness as per Perez et al. (1990).

ϵ bin	Lower bound	Upper bound	f_{11}	f_{12}	f_{13}	f_{21}	f_{22}	f_{32}
1 overcast	1.000	1.065	-1.008	0.588	-0.062	-0.060	0.072	-0.022
2	1.065	1.230	0.130	0.683	-0.151	-0.019	0.066	-0.029
3	1.230	1.500	0.330	0.487	-0.221	0.055	-0.064	-0.026
4	1.500	1.950	0.568	0.187	-0.295	0.109	-0.152	-0.014
5	1.950	2.800	0.873	-0.392	-0.362	0.226	-0.426	0.001
6	2.800	4.500	1.132	-1.237	-0.412	0.288	-0.823	0.056
7	4.500	6.200	1.060	-1.600	-0.359	0.264	-1.127	0.131
8 clear	6.200	-	0.678	-0.327	-0.250	0.156	-1.377	0.251

In addition to the above four representative anisotropic sky diffuse models, there are multiple others proposed (e.g. Bugler, 1977; Gueymard, 1987, 1986; Ma and Iqbal, 1983; Muneer, 1990; Skartveit and Olseth, 1986; Steven and Unsworth, 1980; Temps and Coulson, 1977; Willmott, 1982). The findings of the numerous studies (e.g. Cameron et al., 2008; David et al., 2013; Diez-Mediavilla et al., 2006, 2005; Evseev and Kudish, 2009; Freeman et al., 2013; Gracia and Huld, 2013; Kamali et al., 2006; Khalil and Shaffie, 2013; Loutzenhiser et al., 2007; Noorian et al., 2008; Notton et al., 2006; Utrillas and Martinez-Lozano, 1994; Yang et al., 2013) validating the above models imply that the accuracy of a sky diffuse model is highly location-dependent and the order of accuracy between the models varies with location. On average however, anisotropic models seem to show significantly better performance than the isotropic ones.

Finally, W_{poa} is also affected by the shading conditions at POA. Shading can be caused by objects both external and internal to the power station. External sources such as trees, buildings, and the topography of the landforms surrounding the site location are obviously highly location-specific and are normally minimised through site assessment studies prior to the plant construction. The shading caused by the plant itself, in turn, is more difficult to avoid. Such shading occurs at the module level due to opaque front contacts (OFC) and at the system level due to other arrays and structures built for power conditioning equipment. Shading affects PV performance directly through lowering W_{poa} but also indirectly through causing performance variability among arrays resulting in mismatch losses. In order to model both of these effects, the shading-induced loss in W_{poa} needs to be computed. In a strictly physical sense, the beam and diffuse transposition factors should be modified to account for the changed distribution of incident irradiance in the case of array shading. The photons radiated from the shaded part of the hemisphere reach POA due to reflection from the surface of the shading object, for which reason the loss in W_{poa} depends on the reflection coefficient of the shading body. This level of analysis can be considered as excessively comprehensive, however, considering the relative significance of shading for the total losses on a daily basis. Row spacing is normally designed in a way that array self-shading only occurs in the early morning and late afternoon. Moreover, in the case of tracking, shading is normally further minimised through backtracking. That is why usually, the simulation of the effects of array self-shading is simplified by computing a shading factor that only affects DNI and stands for the ratio of the shaded POA surface area to the total POA area. A model developed by Narvarte and Lorenzo (2008) can be used to estimate the shading factor on tracking surfaces. It is, therefore, also helpful in developing backtracking algorithms. The partial shading-induced mismatch losses are further discussed at the end of section 3.4.1.

3.1.2 Angular Reflection and Soiling Losses

The increase in reflection due to increasing ϑ is a well-known phenomenon, which is of relevance for any field where the daily changes in surface reflection or absorption of sunlight bear significance. An incidence angle modifier (IAM) is the most common approach to modelling the phenomenon in most fields. In the context of PV performance assessment, IAM for any ϑ can be defined as the ratio of W_{abs} to W_{abs} at ϑ of 0° . The most common PV performance simulation tools use a variety of physical, semi-empirical, and empirical formulations of IAM. The main focus of these equations lies on modelling the interaction between light and an air-glass interface. The five-parameter model developed by De Soto et al. (2006) uses a physical expression of IAM derived by Duffie and Beckman (2006, p. 234) based on Snell's, Fresnel's, and Bouguer's laws. In turn, PVsyst (PVsyst SA, 2014a) uses ASHRAE's semi-empirical IAM specified in ASHRAE Standard 93-77 (1978) and developed by Souka and Safwat (1966) while the Sandia PV Array Performance Model (SAPM) employs an entirely empirical 5th order polynomial function (King et al., 2004).

As explained in section 2.3.2, the impact of ϑ on the reflection losses incurred by a solar module is heavily influenced by superficial dust deposition. That is why in this thesis, angular reflection and soiling losses are discussed in the same section. Although the coupled relationship between soiling and angular reflection losses have already been identified by Wilson and Ross (1983), the only significant contribution found to have been made to the topic from the modelling perspective is by Martín and Ruiz (2005, 2002, 2001). They integrate angular reflection loss effects of ϑ and dust deposition into the basic isotropic irradiance transposition model (Martín and Ruiz, 2002, 2001) and into the Hay-Davies model as presented in Eq. 3.9 (Martín and Ruiz, 2005).

$$W_{eff} = W_{b,n} \left(1 + \frac{W_{d,h}}{W_{toa,n} \cos \theta_z} \right) \cos \theta (1 - F_b) + W_{d,h} \left(1 - \frac{W_{b,n}}{W_{toa,n}} \right) \frac{1 + \cos \beta}{2} (1 - F_d) + \rho W_{g,h} \frac{1 - \cos \beta}{2} (1 - F_r) \quad (3.9)$$

where

$$F_b = \frac{\exp \left[-\cos \left(\frac{\alpha}{a_r} \right) \right] - \exp \left[\frac{-1}{a_r} \right]}{1 - \exp \left[\frac{-1}{a_r} \right]}$$

$$F_d \cong \exp \left\{ \frac{-1}{a_r} \left[\frac{4}{3\pi} \left(\sin \beta + \frac{\pi - \beta - \sin \beta}{1 + \cos \beta} \right) + c \left(\sin \beta + \frac{\pi - \beta - \sin \beta}{1 + \cos \beta} \right)^2 \right] \right\}$$

$$F_r \cong \exp \left\{ \frac{-1}{a_r} \left[\frac{4}{3\pi} \left(\sin \beta + \frac{\beta - \sin \beta}{1 - \cos \beta} \right) + c \left(\sin \beta + \frac{\beta - \sin \beta}{1 - \cos \beta} \right)^2 \right] \right\}$$

As is evident based on Eq. 3.9, the equation only holds for constant spectral distribution and spectrally neutral angular reflection and soiling losses. Apart from the solar geometry and array inclination, the angular loss factors F_b , F_d , and F_r depend on the fitting parameters a_r and c . These parameters are functions of dust deposited on POA and, according to Martín et al. (2012), largely independent of the PV material in question. The model has been validated in Spain's conditions by Martín and Ruiz (2005) and Martín et al. (2012).

Martín and Ruiz (2005) and Martín et al. (2012) give only qualitative estimates on the soiling levels associated with different values of the fitting parameters a_r and c . There is no quantitative model available for linking these parameters to soiling. In fact, widely used soiling models are not available in general. Some plant operators and project developers such as SunPower (Anderson, 2014) and First Solar (Littmann, 2014) have developed their own empirical models for their private use only. These models relate the soiling-induced loss in P_{ac} to rainfall, cleaning schedule, and empirically derived soiling rates. As can be expected, these models are highly dependent on the location as well as the season. Kimber et al.'s (2006) soiling loss model is the presumably first publicly available model for estimating power losses due to dust deposition at hourly resolution. Kimber et al. (2006) find out that during long dry periods, plant performance shows linear degradation with time except for the first 3-7 weeks after rainfall when the degradation is significantly slower or non-existent. Kimber's et al. study's geographical scope is limited to the United States. As discussed in section 2.3.1, atmospheric aerosol loading has been measured to experience high spatial as well as seasonal variation in the Arabian Peninsula. Therefore, the soiling loss model proposed by Kimber et al. is likely not to be generalizable to the conditions of the region. The general difficulty of soiling loss modelling is related to the complexity of the physical phenomena involved in superficial dust deposition. In the regions characterised by highly dynamic dust transport mechanisms, the prediction of soiling losses may not be possible without taking the seasonal weather patterns apart from rainfall into account.

3.2 Spectral Modelling

In this thesis, the term spectral modelling is used to refer to the quantification of the PV performance effect of changes in the distribution of the Sun's spectrum with respect to the standard spectrum (G03 Committee, 2012). As solar cells are spectrally sensitive devices, alteration in the content of the incident spectrum inevitably results in a change in their performance. Since optical models only operate with

broadband irradiance variables, spectral models are used to correct these irradiance levels such that the values are mutually comparable in terms of the resulting power output even if the corresponding spectral distributions differ from each other. Therefore, a spectral model is required for the accurate estimation of W_{eff} . Spectrally distributed irradiance data are not as widely available as broadband irradiance measurements due to the more complex instrumentation requirements. Moreover, in most of the areas where PV-related research has traditionally been concentrated, the spectral distribution of sunlight is mainly a function of optical path length. Consequently, the most affected time periods are early mornings and late afternoons, whose contribution to power output is relatively low. That may be the reason for the poor availability of spectral correction models. Under desert climates, the Sun's spectrum probably experiences less predictable variability due to heavy atmospheric aerosol loading and hence, the development of spectral models is of particular importance for desert regions.

Relatively complex radiative transfer models (Betts et al., 2003; Bird and Riordan, 1986; Leckner, 1978) such as SMARTS (Gueymard, 1995, 2001) can be used to accurately model incident spectra in clear sky conditions. These models are computationally comparatively expensive and require several inputs describing the atmospheric conditions. This level of accuracy is often not possible due to the lack of required data and computation speed limitations. That is why simpler empirical and semi-empirical spectral correction models have been developed for PV performance modelling purposes. A simple empirical univariate formula developed by King et al. (1998) relates solar spectral content variation to air mass as follows:

$$f_{AM} = a_0 + a_1 AM + a_2 AM^2 + a_3 AM^3 + a_4 AM^4 \quad (3.10)$$

where f_{AM} is the effective spectral responsivity factor for W_{eff} estimation and a_1 , a_2 , a_3 , and a_4 empirical fitting parameters. King's et al. (1998) model is used both in SAPM (King et al., 2004) and in the five-parameter model (De Soto et al., 2006).

Martín and Ruiz (1999) follow the same logic in their multivariate model of effective spectral responsivity. In addition to air mass, their model also includes information about the AM-independent level of atmospheric attenuation of irradiance through the clearness index K_t , which is defined as the ratio of GHI to the theoretical extraterrestrial irradiance incident on the same POA. Furthermore, their model specifies an effective spectral responsivity factor for each of the three irradiance components: DNI, DHI, and $\rho^* \text{GHI}$.

$$f_x = c_x \exp[a_x(K_t - 0.74) + b_x(AM - 1.5)] \quad (3.11)$$

where x denotes one of the three irradiance components. a_x , b_x , and c_x are empirical material-dependent fitting parameters, which can be calculated for any PV material through interpolating between the band gaps of the reference materials used by Martín and Ruiz (1999) according to Lorenzo (2003, p. 955). The values 0.74 and 1.5 stand for the STC values of K_t and AM, respectively. The model has not been further validated after its publication.

3.3 Thermal Modelling

In terms of PV performance assessment, the purpose of a thermal model is to obtain the temperature of the photoactive layers of a solar cell based on ambient and technological input parameters. In this thesis, the aforementioned temperature is referred to as cell temperature T_c . As can be seen from Figure 3-1, T_c is one of the two main effective input variables involved in PV performance simulation. It influences the conversion efficiency of a solar cell in various ways (see chapter 2.3) and is strongly affected by ambient conditions. The fundamental basis of the simulation of T_c is the heat transfer energy exchange of a solar cell's active components with the surrounding layers and ambient air. There is a wide range of various

software tools available for the analysis of the three main heat transfer mechanisms, radiation, convection, and conduction (see Eq. 2.8 in section 2.3.2). These thermal analysis tools can produce highly accurate results but require detailed information about the thermal characteristics of the materials involved. Furthermore, in the highly dynamic thermal environment of operational solar modules, a stringently physical approach would also involve a non-steady state assessment of heat flows. Consequently, such models are computationally heavy.

Due to the great importance of T_c in PV performance assessment, numerous empirical and semi-empirical models and correlations have been developed for its estimation without a need for transient heat transfer modelling and detailed material-related input parameters. An approach common to all these tools is the aggregation of all different material layers into a single lumped thermal element corresponding to a solar cell or a solar module. Instead of analysing the heat exchange between the layers, they focus on modelling the interaction between this element and the ambient atmosphere. The most significant ambient parameters are ambient air temperature T_a , incident radiant flux density W_{poa} , and wind velocity vector \mathbf{v}_w . While T_a has a strong impact on the absolute level of T_c , the difference between T_c and T_a is mainly determined by W_{poa} and wind speed v_w (Griffith et al., 1981). Should all other variables be held constant, the temperature difference is linearly dependent on W_{poa} . The slope of this dependence, the Ross coefficient, is mostly dependent on v_w , mounting method, and module composition (Ross, 1976). Since the internal heating process within a solar cell depends on the efficiency at which the cell is converting radiation into electricity, most of these model formulations also include η_c as an input variable. As η_c is dependent on T_c however, the expressed relationship is coupled and mathematically implicit. In addition to η_c , the technological parameters commonly included in these models are module absorptivity and nominal operating cell temperature, which is useful in that it is often included in the datasheets of commercially available solar modules.

Validation of Thermal Models for Photovoltaic Cells under Hot Desert Climates

As implied by the discussion above, the choice of an operating cell temperature model can have a great impact on the results of PV performance simulation. Most of the traditional main market areas of PV systems are located in regions with a temperate or subtropical climate. Consequently, performance modelling tools have also been designed and validated mainly based on measurements made in those regions. When PV capacity building is considered in site locations, whose conditions differ significantly from the ones on the basis of the tools used, recalibration is required.

As part of this thesis study, a project (Tuomiranta et al., 2013) to calibrate and validate operating cell temperature modelling tools based on data collected from a test field installed in Abu Dhabi, UAE (24° 26' 23" N, 54° 37' 11" E) is conducted. Abu Dhabi is located in a hot arid region where solar power has a tremendous and largely untapped potential. This study aims to offer simulation tools better suited to the local conditions and thereby support PV deployment in the region.

Eq. 2.8 (see section 2.3.2) is based on the non-steady state thermal energy balance of PV modules and when decomposed, it involves several module-specific parameters as well as T_{mod} as a variable on both sides of the equation. As explained above, the thermal modelling tools commonly used in PV performance simulators are restricted to steady state conditions. Skoplaki and Palyvos (2009) present a comprehensive review of dozens of such empirical and semi-empirical tools. All the tools considered in the study summarised in this subsection are empirical and semi-empirical as well. In these models, the parameters related to the thermophysical properties of module materials have been lumped into one or a few

coefficients. In addition, all the tools to be validated here are mathematically explicit in that they express T_c entirely in terms of other measurable variables and they contain at most four independent variables: T_a [°C], W_{poa} [W/m²], v_w [m/s], and η_c . The objective of the analysis presented here is to validate modelling tools that are PV material-independent by using data from multiple materials. Therefore, the tools do not include any material-specific parameters.

Methodology

The data required for the validation are collected through measurements over a two-year period, beginning in early 2011. PV module temperature measurements are made in the test field mentioned above by means of adhesive sensors attached on module back sheets. Data are collected from 20 ground-mounted systems of roughly 1 kWp representing various manufacturers and seven different semiconductor materials. Each of the 20 arrays is equipped with two sensors and connected to a power inverter of a nominal output power of 1 kW. The output power levels of each array are measured at the inverter output. Both final temperature and power output data consist of mean values with a resolution of five minutes. Ambient air temperature measurements are taken at the test field over the same period and with the same temporal resolution. A weather station located 850 m west of the test field is used for measurements of relative humidity and wind speed two and five metres above the ground level, respectively. Also ambient temperature two metres above the ground level is measured at this station in order to validate the measurements made in the test field. Another weather station located 2.3 km south of the test field is used for the measurements of DNI, DHI, and GHI. The measurements taken at both weather stations are averaged and stored at intervals of five minutes at the former and ten minutes at the latter.

Linear interpolation is used to fill the short-term data gaps resulting from the different measurement averaging intervals. The ambient air temperature data are validated by comparing the two datasets and omitting those data points with a discrepancy higher than 5 °C. Module temperature measurements higher than 85 °C and lower than 0 °C are also omitted as well as the measurements that are more than 35 °C higher or more than 1 °C lower than ambient air temperature. The periods of fallen module temperature sensors are detected through spotting change points in the cumulative sum curves of the difference between the daily and annual mean standard deviations of the observed temperatures. The final module temperature estimates are obtained by averaging the measurements of the two sensors of each array. Irradiance and relative humidity measurements are converted into estimates of W_{eff} . The estimation is based on the work done by Martín and Ruiz (2002) and Martín et al. (2012) on the angular of incidence losses of PV modules and Perez et al. (1990) on sky diffuse modelling. The Sun's position is estimated based on the tool developed by Reda and Andreas (2008). Estimates of T_c are derived from W_{eff} and T_{mod} using a relation given by King et al. (2004). The power output measurements are used to estimate η_c of the cells of each array. Data points lower than 50 W and higher than 1100 W (maximum output power) are omitted, and the remaining data are divided by the inverter efficiencies at the respective inverter load ratios. The efficiency levels at different inverter load ratios are approximated based on a curve given in the technical specifications of the inverter used. The obtained DC power estimates are divided by the estimates of W_{eff} and the combined surface area of the cells in each array. Finally, the data points exceeding 120% of $\eta_{c,stc}$ are omitted. $\eta_{c,stc}$ is estimated by dividing the module nominal power by $W_{poa,stc}$ and the combined cell surface area.

16 thermal modelling tools for PV modules are validated based on the data collected. The tools contain in most parts the same elements as originally proposed. Some of them are, however, modified to better suit the purposes of the study. The tools and the corresponding original works are listed in Table 3-2.

Nine of the tools express T_c as a function of weather variables only, whereas the remaining seven also include η_c as an independent variable. The most suitable models for final calibration are found through cross-validation. The data are partitioned into five subsets and hence, five rounds of cross-validation with each one of the subsets serving as the testing set are performed for each tool. The tools providing lower average root mean square errors (RMSE) over the five rounds than the median value are selected for the final model validation.

Table 3-2. Thermal PV cell modelling tools to be validated.

#	Tool	Adapted from
1	$T_c = T_a + \beta$	Evans (1981)
2	$T_c = T_a + \beta W_{eff}$	Ross (1976)
3	$T_c = \beta_1 + T_a + \beta_2 W_{eff}$	Schott (1985)
4	$T_c = \beta_1 + \beta_2 T_a + \beta_3 W_{eff}$	Lasnier and Ang (1990, p. 258)
5	$T_c = \beta_1 + \beta_2 T_a + \beta_3 W_{eff} + \beta_4 v_w$	Risser and Fuentes (1984)
6	$T_c = T_a + \beta_1 W_{eff} (1 + \beta_2 T_a) (1 - \beta_3 v_w)$	Servant (1985)
7	$T_c = T_a + W_{eff} (\beta_1 v_w^2 + \beta_2 v_w + \beta_3)$	King (1996)
8	$T_c = T_a + W_{eff} [\beta_1 \exp(\beta_2 v_w) + \beta_3]$	King et al. (1998)
9	$T_c = T_a + W_{eff} [\exp(\beta_1 + \beta_2 v_w) + \beta_3]$	King et al. (2004)
10	$T_c = \beta_1 + \beta_2 T_a + \beta_3 W_{eff} + \beta_4 v_w + \beta_5 \eta_c$	
11	$T_c = T_a + \beta W_{eff} (1 - \eta_c)$	Duffie and Beckman (2006, p. 760)
12	$T_c = T_a + \beta_1 W_{eff} (\beta_2 - T_a) (1 - \eta_c)$	Duffie and Beckman (2006, p. 760)
13	$T_c = T_a + \beta_1 W_{eff} (1 + \beta_2 T_a) (1 - \beta_3 v_w) (1 - \beta_4 \eta_c)$	Servant (1985)
14	$T_c = T_a + \frac{\beta_1 W_{eff}}{\beta_2 + \beta_3 v_w} (1 - \eta_c)$	Duffie and Beckman (2006, p. 760)
15	$T_c = T_a + \frac{\beta_1 + \beta_2 T_a + W_{eff} (1 - \eta_c)}{\beta_3 + \beta_4 v_w}$	Schott (1985)
16	$T_c = \frac{T_a + \left(\frac{W_{eff}}{\beta_1 + \beta_2 v_w} \right) (1 - \beta_3 \eta_c)}{1 - \beta_4 \left(\frac{W_{eff}}{\beta_1 + \beta_2 v_w} \right) \eta_c}$	Rabl (1986, p. 51)

Results and Discussion

Table 3-3 shows the average RMSE values for each validated tool. Four of the tools involving only weather variables and three of the remaining ones perform better than the median case with an RMSE of 3.05. Three out of these seven tools are simple linear regression modelling tools (4, 5, and 10).

Table 3-3. RMSE value for each tool averaged over the five rounds of cross-validation.

Tool #	1	2	3	4	5	6	7	8	9	10	11	12	13	14	15	16
RMSE	7.67	3.43	2.92	2.91	2.61	3.05	3.04	3.06	3.05	2.60	3.47	3.47	3.05	3.12	2.50	2.86

The validated tools are calibrated based on the entire data and the resulting models are presented in Table 3-4. All the coefficients estimated are statistically significant at significance levels of 1%. The accuracy of the provided fits is tested by means of the coefficient of determination (R^2), and the RMSE (rRMSE) and the mean bias error (rBIAS) normalised by the mean of T_c .

Table 3-4. Validated models with the corresponding test statistics.

Tool #	Model	R^2	rRMSE	rBIAS
15	$T_c = T_a + \frac{120 + 0.739T_a + W_{eff}(1 - \eta_c)}{28.6 + 1.51v_w}$	0.958	4.80%	-0.02%
10	$T_c = 6.45 + 1.04T_a + 0.0257W_{eff} - 0.737v_w - 6.28\eta_c$	0.955	4.98%	-0.00%
5	$T_c = 5.47 + 1.04T_a + 0.0258W_{eff} - 0.741v_w$	0.954	5.00%	-0.00%
16	$T_c = \frac{T_a + \left(\frac{W_{eff}}{23.7 + 1.61v_w} \right) (1 + 2.30\eta_c)}{1 + 0.0468 \left(\frac{W_{eff}}{23.7 + 1.61v_w} \right) \eta_c}$	0.945	5.49%	-0.93%
4	$T_c = 2.92 + 1.04T_a + 0.0255W_{eff}$	0.943	5.58%	0.00%
3	$T_c = 4.06 + T_a + 0.0258W_{eff}$	0.943	5.60%	-0.00%
7	$T_c = T_a + W_{eff} (0.000127v_w^2 - 0.0025v_w + 0.0391)$	0.938	5.84%	-1.51%

As can be seen from Table 3-4, the rBIAS values are very low for most of the models and thus, the comparison between the models is founded on R^2 and rRMSE. The model built on tool 15, here referred to as the Schott model, provides the highest R^2 and the lowest rRMSE. The linear regression models based on tools 10 and 5, respectively referred to as the LR5 and the Risser models, give the next best fits in terms of R^2 and rRMSE. The rBIAS levels of these models are even lower than that of the Schott model. As per R^2 and rRMSE, the model constructed on tool 16, referred to as the Rabl model, provides the fourth best fit but slightly underestimates T_c .

Figure 3-2 shows that on a mostly clear day common in Abu Dhabi, all four models mentioned above produce results largely consistent with the measurements. As can be seen from the figure, the modelled temperatures show the highest bias levels immediately after sunrise. The models are not able to capture the transient heat-up period after sunrise without significant underestimation as in the case of the Rabl model (Figure 3-2d). From power production viewpoint however, the period is rather insignificant. The resulting curves also differ in variance due to the varying weights amplifying the η_c terms. In the case of data based on a single array, the variance of the curves in Figure 3-2a, b, and d would be significantly reduced because instead of 20 different curves of η_c , there would be only one value of η_c for each time point. Figure 3-3 compares the results of the four models on a cloudy day. In this case, it is found out that none of the models are capable of following the rapid changes in T_c .

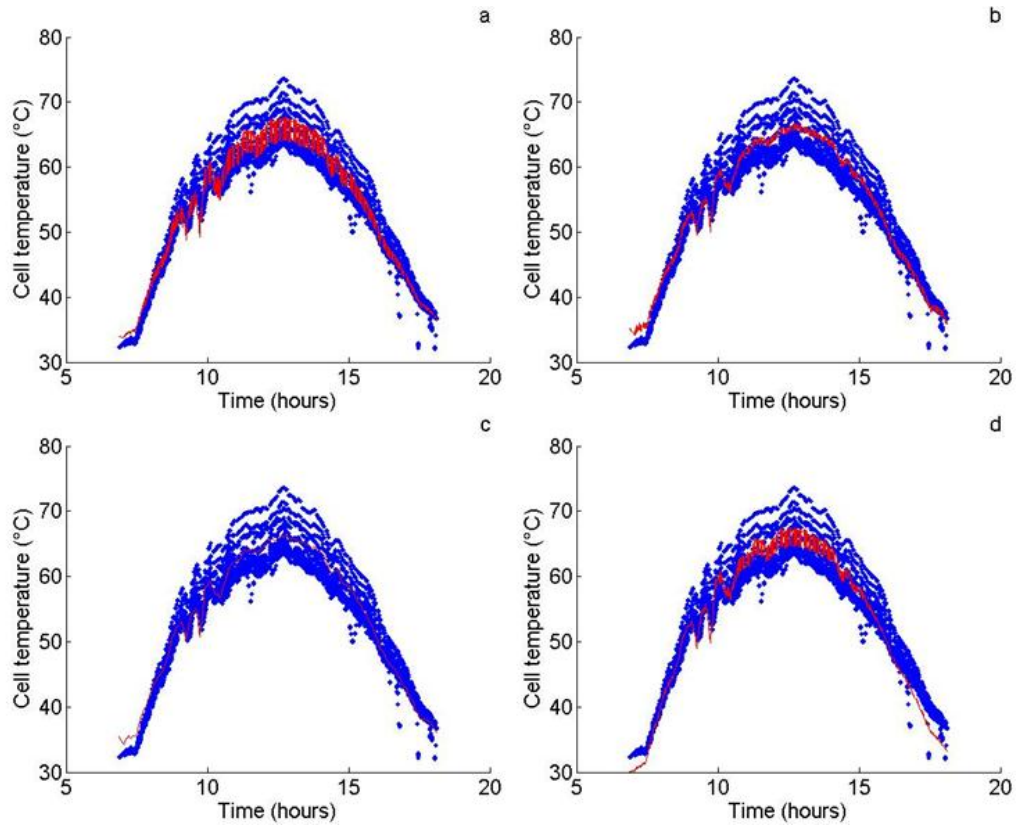


Figure 3-2. Measured (in blue) vs. modelled (in red) T_c on a clear day (May 2nd, 2011) based on tool (a) 15; (b) 10; (c) 5; (d) 16.

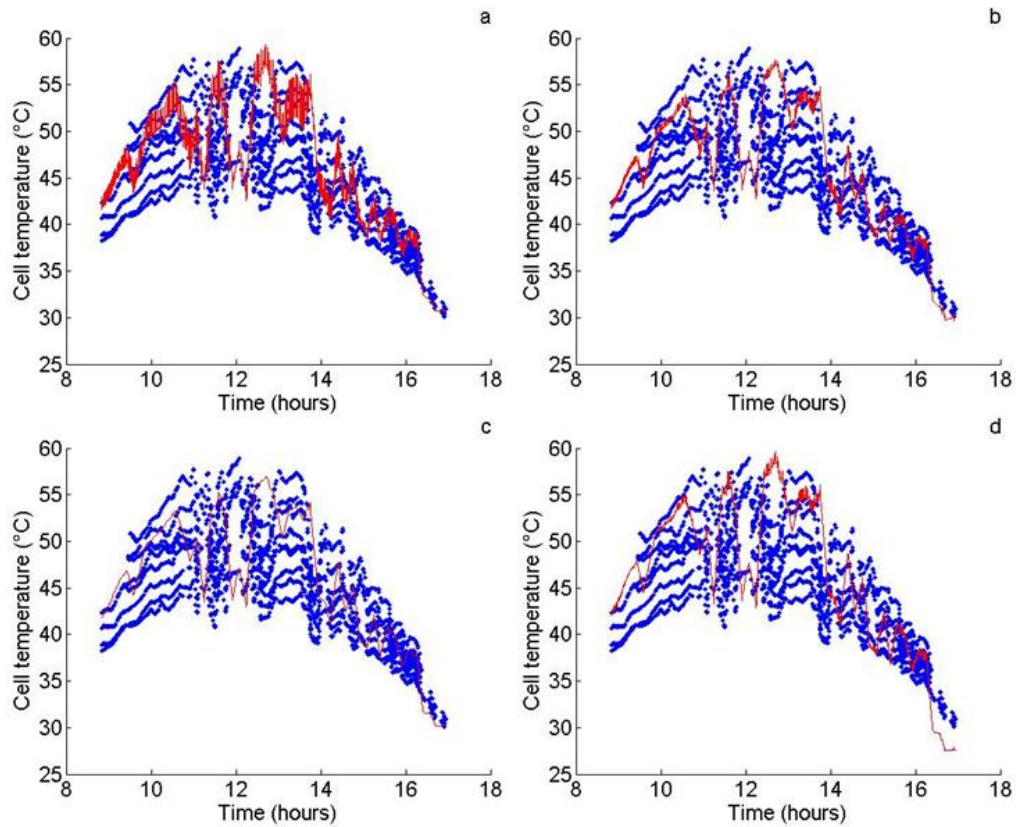


Figure 3-3. Measured (in blue) vs. modelled (in red) T_c on a cloudy day (November 9th, 2011) based on tool (a) 15; (b) 10; (c) 5; (d) 16.

Since the models are found to perform well only on clear days, further weather type-specific analysis is required in order to reliably predict T_c throughout the year. It might also be useful to validate models specific to different materials. Such models would contribute to the understanding of the applicability of different PV technologies under hot desert climates and thus support PV deployment where it makes the most sense.

3.4 Electrical Modelling

The optical, spectral, and thermal models produce spatiotemporal variables, W_{eff} and T_c , which can be directly converted into P_{ac} in the electrical model. The electrical model comprises performance modelling tools for the three functions of a PV power station's system architecture: power generation, power transmission, and power conversion. While the electrical model of power generation accounts for the simulation of most of the losses involved in photovoltaic energy conversion, the models of transmission and conversion exclusively focus on the losses occurring in conductors and power conditioning equipment, respectively.

3.4.1 Power Generation

The electrical model for power generation involves the simulation of all losses occurring inside solar cells and is, therefore, the most important component of a PV performance model. Its purpose is to convert ambient and technological input parameters into the power output of a cell, a module, or an array. As discussed in section 3.3, if T_c is simulated by means of a thermal model which is dependent on η_c , the thermal model and the electrical model for generation are coupled and, therefore, essentially comprise one thermoelectrical model. Both physical and semi-empirical electrical models are widely used in PV performance assessment. There are also numerous empirical relationships between plant output and ambient and technological parameters. Due to their weak generalizability across different locations and technologies however, they are typically not used in analyses with a focus on PV performance but in more generally oriented studies where the output of PV plants is a single input itself. That is why the focus of this thesis study lies on the most common physical and semi-empirical electrical models for PV power generation. This subsection presents a review of three popular models: PVsyst's module model (PVsyst SA, 2014b), the five-parameter model (De Soto et al., 2006), and the electrical modelling tool of SAPM (King et al., 2004). The equations given in the subsection are based on the above three references unless otherwise indicated.

The equivalent circuit approximations of solar cell behaviour are the basis of PVsyst's module model and the five-parameter model. The two most popular such approximations are the single diode model expressed in Eq. 2.4 in section 2.2.1 and the double diode model expressed in Eq. 2.12 in section 2.3.4. Based on these equivalent circuit models, the entire I-V characteristic curve of a solar cell can be obtained. In order to compute the I-V characteristics based on the single diode model, one needs to know the values of the following six parameters that are dependent on the PV technology deployed and the prevalent ambient conditions:

- Photogenerated current I_{ph}
- Reverse saturation current I_0
- Series resistance R_s
- Shunt resistance R_p
- Diode ideality factor n_d
- Cell temperature T_c

The equivalent circuit models of solar cells can be easily applied to modules and arrays consisting of series-connected cells by multiplying all the voltage and resistance terms (including the thermal voltage kT_c/e) by the number of cells in series N_s (Tian et al., 2001).

A prerequisite for PVsyst's module model to function in its default mode is that R_p as well as either R_s or n_d are known as constants or functions of T_c and W_{eff} . The model also assumes T_c not to be dependent on η_c and uses the following simple approximation in the case of free-standing arrays:

$$T_c = T_a + \frac{0.81W_{poa}}{29W/(m^2K)} \quad (3.12)$$

As R_p , T_c , and either R_s or n_d are known for any combination of ambient conditions, the STC parameters $I_{ph,STC}$, $I_{0,STC}$, and either $n_{d,STC}$ or $R_{s,STC}$ can be solved for based on the following system of three single diode model (Eq. 2.4, section 2.2.1) equations in the three STC reference conditions with known output current and voltage levels, $I_{sc,STC}$, $V_{oc,STC}$, $I_{mpp,STC}$, and $V_{mpp,STC}$ (usually given in module datasheets):

- Short circuit ($V_{sc,STC} = 0$)

$$I_{sc,STC} = I_{ph,STC} - I_{0,STC} \left[\exp \left(\frac{eI_{sc,STC}R_{s,STC}}{n_{d,STC}N_s kT_{c,STC}} \right) - 1 \right] - \frac{I_{sc,STC}R_{s,STC}}{R_p} \quad (3.13)$$

- Open circuit ($I_{oc,STC} = 0$)

$$0 = I_{ph,STC} - I_{0,STC} \left[\exp \left(\frac{eV_{oc,STC}}{n_{d,STC}N_s kT_{c,STC}} \right) - 1 \right] - \frac{V_{oc,STC}}{R_p} \quad (3.14)$$

- Maximum power point

$$I_{mpp,STC} = I_{ph,STC} - I_{0,STC} \left\{ \exp \left[\frac{e(V_{mpp,STC} + I_{mpp,STC}R_{s,STC})}{n_{d,STC}N_s kT_{c,STC}} \right] - 1 \right\} - \frac{V_{mpp,STC} + I_{mpp,STC}R_{s,STC}}{R_p} \quad (3.15)$$

Based on the values of $I_{ph,STC}$ and $I_{0,STC}$, derived from Eq. 3.13-15, I_{ph} and I_0 can be calculated by means of Eq. 3.16 and Eq. 3.17, respectively.

$$I_{ph} = \frac{W_{eff}}{W_{poa,STC}} [I_{ph,STC} + \alpha_{Isc,STC} (T_c - T_{c,STC})] \quad (3.16)$$

$$I_0 = I_{0,STC} \left(\frac{T_c}{T_{c,STC}} \right)^3 \exp \left[\frac{eE_{g,STC}}{n_d N_s k} \left(\frac{1}{T_{c,STC}} - \frac{1}{T_c} \right) \right] \quad (3.17)$$

W_{eff} is calculated by means of physical optical and spectral models based on basic irradiance variables and technological parameters. $\alpha_{Isc,STC}$ and N_s are usually given in module datasheets, while $E_{g,STC}$ is known based on basic material properties. In the case of a-Si modules, PVsyst uses the double diode model (Eq. 2.12, section 2.3.4) instead of the single diode one.

In contrast to PVsyst's module model, the five-parameter model approximates the I-V characteristic curve based only on parameters that are normally given in the datasheets of commercially available solar modules. However, as it is a purely electrical model, it requires inputs from optical and thermal models that may require experimental data to function. For instance, this is the case with both the optical and the thermal model of SAPM, which is used by De Soto et al. (2006) in the validation of the five-parameter model. In the model, T_c and n_d are lumped together into a variable a as follows:

$$a = \frac{N_s n_d k T_c}{e} \quad (3.18)$$

Consequently, there are five parameters to be solved for in order to construct I-V characteristics based on the single diode model. Eq. 3.18-22 present the expressions for these parameters:

$$I_{ph} = \frac{W_{eff}}{W_{poa, stc}} [I_{ph, stc} + \alpha_{Isc, stc} (T_c - T_{c, stc})] \quad (3.18)$$

$$I_0 = I_{0, stc} \left(\frac{T_c}{T_{c, stc}} \right)^3 \exp \left\{ \frac{e E_{g, stc}}{N_s k} \left[\frac{1}{T_{c, stc}} - \frac{1 - 0.0002677 (T_c - T_{c, stc}) / K}{T_c} \right] \right\} \quad (3.19)$$

$$R_s = R_{s, stc} \quad (3.20)$$

$$R_p = R_{p, stc} \frac{W_{poa, stc}}{W_{eff}} \quad (3.21)$$

$$a = a_{stc} \frac{T_c}{T_{c, stc}} \quad (3.22)$$

If W_{eff} and T_c are given through optical and thermal models, Eq. 3.18-22 comprise five unknown parameters: $I_{ph, stc}$, $I_{0, stc}$, $R_{s, stc}$, $R_{p, stc}$, and a_{stc} . As in the case of PVsyst's module model, the unknowns are solved for by means of a system of single diode model equations in different STC conditions. In order to obtain values for all the five unknown parameters, two derivative equations are added to the system specified in Eq. 3.13-15. The first one (Eq. 3.23) sets the slope of the $P(V)$ curve zero at MPP and the second one (Eq. 3.24) approximates $R_{p, stc}$ as the additive multiplicative inverse of the slope of the I-V curve at short circuit.

$$\left. \frac{d(IV)}{dV} \right|_{mpp} = 0 \quad (3.23)$$

$$\left. \frac{dI}{dV} \right|_{sc} = - \frac{1}{R_{p, stc}} \quad (3.24)$$

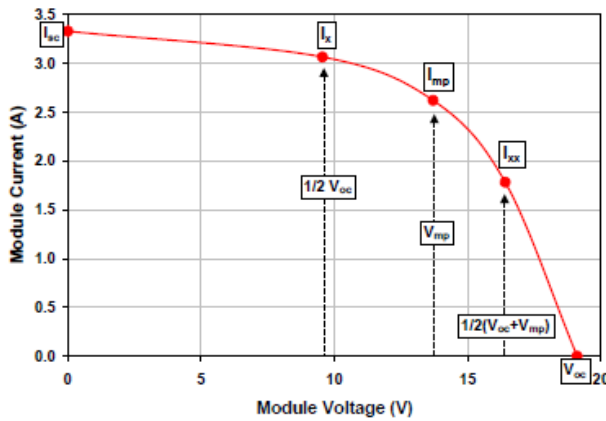


Figure 3-4. I-V characteristic curve points provided by SAPM. (King et al., 2004).

In contrast to PVsyst's module model and the five-parameter model, the SAPM electrical model has been designed to only provide performance parameters at certain points on the I-V curve and are, therefore, not optimised for reconstructing I-V characteristic curves. The points provided by the model are shown in Figure 3-4. The model is semi-empirical as the other components of SAPM. Instead of linking the performance of PV modules to the physical parameters involved in the equivalent circuit models, SAPM specifies I and V as semi-empirical functions of W_{eff} and T_c . with physical parameters consisting only of the corresponding I and V levels at STC. Apart from N_s and the physical constants k and e , all other parameters

are empirical material-dependent coefficients, which are produced through PV performance measurements. SNL has measured these coefficients for dozens of solar modules, though, mostly representing crystalline silicon wafer-based module types. These data are publicly accessible in the Sandia Modules library (Sandia National Laboratories, 2014a). The performance of a module is defined at the five reference points through Eq. 3.24-29.

$$I_{sc} = I_{sc,stc} \frac{W_{eff}}{W_{poa,stc}} \left[1 + \alpha_{I_{sc}} (T_c + T_{c,stc}) \right] \quad (3.24)$$

$$I_{mpp} = I_{mpp,stc} \left[C_0 \frac{W_{eff}}{W_{poa,stc}} + C_1 \left(\frac{W_{eff}}{W_{poa,stc}} \right)^2 \right] \left[1 + \alpha_{I_{mpp}} (T_c + T_{c,stc}) \right] \quad (3.25)$$

$$V_{oc} = V_{oc,stc} + N_s \frac{nkT_c}{e} \ln \left(\frac{W_{eff}}{W_{poa,stc}} \right) + \left[\beta_{V_{oc,stc}} + m_{\beta_{V_{oc}}} \left(1 - \frac{W_{eff}}{W_{poa,stc}} \right) \right] (T_c + T_{c,stc}) \quad (3.26)$$

$$V_{mpp} = V_{mpp,stc} + C_2 N_s \frac{nkT_c}{e} \ln \left(\frac{W_{eff}}{W_{poa,stc}} \right) + C_3 N_s \left[\frac{nkT_c}{e} \ln \left(\frac{W_{eff}}{W_{poa,stc}} \right) \right]^2 + \left[\beta_{V_{mpp,stc}} + m_{\beta_{V_{mpp}}} \left(1 - \frac{W_{eff}}{W_{poa,stc}} \right) \right] (T_c + T_{c,stc}) \quad (3.27)$$

$$I_x = I_{x,stc} \left[C_4 \frac{W_{eff}}{W_{poa,stc}} + C_5 \left(\frac{W_{eff}}{W_{poa,stc}} \right)^2 \right] \left[1 + \alpha_{I_x} (T_c + T_{c,stc}) \right] \quad (3.28)$$

$$I_{xx} = I_{xx,stc} \left[C_6 \frac{W_{eff}}{W_{poa,stc}} + C_7 \left(\frac{W_{eff}}{W_{poa,stc}} \right)^2 \right] \left[1 + \alpha_{I_{xx}} (T_c + T_{c,stc}) \right] \quad (3.29)$$

An extensive historical overview of the development of the above and other PV performance simulation models is presented by Stein and Klise (2009). The Loss Factor Model (LFM), which is relatively new, increasingly popular PV performance model, is not included in Stein and Klise's report. It is a semi-empirical model developed by Sutterlueti et al. (2011) and further improved and validated by Sellner et al. (2012a), Ransome et al. (2012), and Sellner et al. (2012b). LFM has showed good performance when compared to SAPM and equivalent circuit-based models (Stein et al., 2013). However, because no module database for the model's coefficients exists yet, it cannot be integrated in the PV performance simulator being developed. Therefore, LFM is not thoroughly discussed in the review presented in this subsection.

The above models do not include a physical modelling tool for the effect of performance mismatch between modules and arrays due to partial shading and fabrication process-related, inherent variability in module performance. In PVsyst for instance, a fixed loss of 2% is by default assumed to be incurred due to mismatch losses. Nevertheless, there is a number of studies (e.g. Alonso-García et al., 2006; Di Dio et al., 2009; Ishaque et al., 2011; Karatepe et al., 2007; Patel and Agarwal, 2008; Petrone et al., 2007; Ramaprabha and Mathur, 2008) proposing a model for the mismatch effect –often with a focus on the effects of partial shading, though. Another loss process that is somewhat difficult to address by means of a physical model is the time-dependent degradation. Typically, PV performance models consider long-term degradation through an accumulative annual percentage loss in output without taking the exact degradation mechanisms into account. Jordan et al. (2012) present a comprehensive review of the time-dependent degradation rates characterising different PV materials and geographical regions.

3.4.2 Power Transmission

As discussed in section 2.3.5, transmission losses occur due to Joule heating in a power station's conductors i.e. metal wires. In principle, the estimation of the power losses P_{tl} caused by Joule heating on the plant's DC side is straightforward as they increase quadratically with current based on the equation expressed in Eq. 3.30.

$$P_{tl} = RI^2 \quad (3.30)$$

On the AC side, the transmission losses are often considered to be negligible due to the high voltage level. Although the resistivity of metals is known to be a function of temperature, it is normally assumed that the resistance of cables is only dependent on their length and cross-sectional area apart from the conductor material properties. Also, the effect of mismatch losses is usually not considered. The simplified treatment of transmission losses is due to their relatively low weight in the total losses incurred by a PV power station.

3.4.3 Power Conversion

With respect to the total losses involved in PV power generation, power conditioning losses represent a small share as is implied by the inverter efficiency curve shown in Figure 2-14 in section 2.3.5. At extreme conditions discussed in section 2.3.5 however, inverters may momentarily cause significant losses. There is a plethora of inverter performance models available but in today's context of PV performance modelling, there are three models that have gained particular popularity: the double quadratic model (Baumgartner et al., 2007), Sandia Inverter Performance Model (SIPM) (King et al., 2007), and the inverter model developed by Driesse et al (2008).

All three models have been developed to capture both the power and DC input voltage dependencies of inverter performance. Eq. 3.31 shows the equations expressing inverter-induced power loss P_{il} as a function of output power P_{ac} and input voltage V_{dc} as per the double quadratic model:

$$P_{il} = a_0 + a_1 P_{ac} + a_2 P_{ac}^2 \quad (3.31)$$

where

$$a_i = a_{i,1} + a_{i,2} V_{dc} + a_{i,3} V_{dc}^2$$

As can be seen from Eq. 3.31, the double quadratic model includes nine empirical parameters $a_{i,j}$. Baumgartner et al. (2007) attribute the first, P_{ac} -independent term of Eq. 3.31 to the self-consumption of an inverter's auxiliary and drive circuits, the first degree term to switching transition and non-ohmic losses in semiconductor p-n junctions, and the second degree term to the ohmic losses involved. The double quadratic model can be used only based on actual AC output measurements.

In order to facilitate the usage of basic information available, for instance, in inverter datasheets, SIPM (King et al., 2007) compares input power P_{dc} (instead of P_{ac}) to inverter reference values as follows:

$$P_{ac} = \left[\frac{P_{ac,0}}{A - B} - C(A - B) \right] (P_{dc} - B) + C(P_{dc} - B)^2 \quad (3.32)$$

where

$$A = P_{dc,0} [1 + C_1 (V_{dc} - V_{dc,0})]$$

$$B = P_{so} [1 + C_2 (V_{dc} - V_{dc,0})]$$

$$C = C_0 [1 + C_3 (V_{dc} - V_{dc,0})]$$

In Eq. 3.32, $P_{ac,0}$ stands for the inverter's power rating, P_{dc} for the DC power input, V_{dc} for the DC input voltage, $P_{dc,0}$ for the DC power input at $P_{ac,0}$, $V_{dc,0}$ for the DC input voltage at $P_{ac,0}$, P_{so} for the inverter's self-

consumption, and C_i for empirical coefficients derived from inverter performance data. As in the case of the double quadratic equation, SIPM's main equation is quadratic but the assumed voltage dependence of the power parameters is linear.

While SIPM aims to empirically simulate the efficiency curve of an inverter, Driesse's et al. (2008) model is more physical with a focus on the losses incurred – similarly to the double quadratic model. However, the applicability of the model is improved by involving standard parameters usually given in inverter datasheets. The main equation of Driesse's et al. model is presented in Eq. 3.33.

$$P_{il} = P_{ac,0} \left\{ \left[b_{0,0} + b_{0,1} \left(\frac{V_{dc}}{V_{dc,0}} - 1 \right) \right] + \left[b_{1,0} + b_{1,1} \left(\frac{V_{dc}}{V_{dc,0}} - 1 \right) \right] \frac{P_{dc}}{P_{dc,0}} + \left[b_{2,0} + b_{2,1} \left(\frac{V_{dc}}{V_{dc,0}} - 1 \right) \right] \left(\frac{P_{dc}}{P_{dc,0}} \right)^2 \right\} \quad (3.33)$$

where $b_{i,j}$ are empirical parameters determined based on inverter performance data. As can be seen from Eq. 3.33, Driesse et al. model P_{il} with a quadratic dependence on P_{dc} as done in SIPM and the double quadratic model. Each of the terms of the quadratic equation consist of a term for the losses incurred at $V_{dc,0}$ and a V_{dc} -dependent term. According to Driesse et al., the model provides improved accuracies at medium-to-high power levels compared to SIPM due to its focus on the power lost instead of efficiency.

4. Proposed Performance Model

The main objective of this thesis project is the development of a WebGIS-based PV performance simulation tool for the Arabian Peninsula. This chapter describes how this objective is met in practice. The simulator is designed based on the literature reviews presented in chapters 2 and 3. The suitability of different modelling tools is assessed through criteria developed by analysing the peculiarities of both the WebGIS environment as a modelling platform and the Arabian Peninsula as the geographical scope of the tool. The criteria are outlined and justified in the first subsection. The second subsection describes the algorithmic structure and the current scope of the proposed simulator emphasising the reasoning behind the choices made. The assumptions made in the reference power station design are stated and justified in the third subsection specifying the process of system configuration. The remaining four subsections focus on describing the actual performance modelling steps: optical modelling, spectral modelling, thermal modelling, and electrical modelling.

4.1 PV Performance Assessment in WebGIS Environment

The fact that the simulation tool described in the present chapter will be operated through a web-based GIS platform poses some specific challenges and requirements for the design of the simulator. As explained in section 1, the planned integration in a WebGIS environment is, in fact, one of the reasons why an extensive in-house modelling task of this sort is undertaken by ReCREMA. As the simulator is planned to be fully integrated in the current publicly accessible WebGIS architecture, the use of a piece of commercial simulation software is out of the question for legal and technical reasons.

In the case of conventional PV performance assessment, the focus of modelling efforts usually lies on the maximisation of accuracy within the limits of the available input data. In a WebGIS environment however, computation speed becomes a factor as critical as the accuracy of the results. Therefore, due to the importance of computational performance, the most suitable modelling tools for the simulator being developed may not give the best fit to in-situ observations but rather offer the best compromise between computing speed and the accuracy of the generated estimates. The in-house development of the model makes it possible to optimise the different tools included from both perspectives.

In addition to the two typical dimensions, time and the variable of interest, the model being developed involves a third dimension, space. When PV performance is simulated, for instance, for a country like the UAE at a spatial resolution of 0.02° over the whole year at hourly resolution, one variable involves more than one hundred million simulation points. When considering the speed requirements involved in web-based modelling tools, it is obvious that all kinds of transient models with path dependence are not feasible. In fact, no model involving iterative computation over the entire domains under simulation can be selected. This limits the pool of feasible models to the ones comprising only analytically solvable equations. Though, if the model is independent of the continuous user input variables (see section 4.2), also pre-defined look-up tables can be used.

As the primary outputs of the simulator being developed are in the form of maps, the user is likely to be particularly interested in the spatial variability of the simulation outcome. How different areas compare to each other in terms of PV performance is one of the main questions sought to be answered by means of the simulator. That is why the validation of the possible empirical and semi-empirical models should be performed at more than one site preferably representing as many technologies and different

ambient conditions as possible. This future validation work will obviously be facilitated by using a simulator which is developed by ReCREMA.

4.2 Algorithmic Architecture and Scope

The primary purpose of the PV performance simulator under development is to convert spatiotemporally variable input data into spatial data that indicate the performance of a user-defined PV power station over the entire time span of interest. The processes involved at the highest level are presented in Figure 4-1. The first process is the interpretation and the quality check of the user inputs and their conversion into a form which can be processed during the actual performance simulation. The spatial domain of interest is divided by means of the interpretation programme into as many subsets as there are processors available. These subsets are allocated to the processors, and the second high-level step, the actual performance simulation, is then performed by several processors in parallel. In this way, computation speed can be increased if there are several processors available. The performance simulation roughly follows the steps illustrated in Figure 3-1 at the beginning of chapter 3. The last step is the conversion of the simulation outcome into a form which is comprehensible to the user.

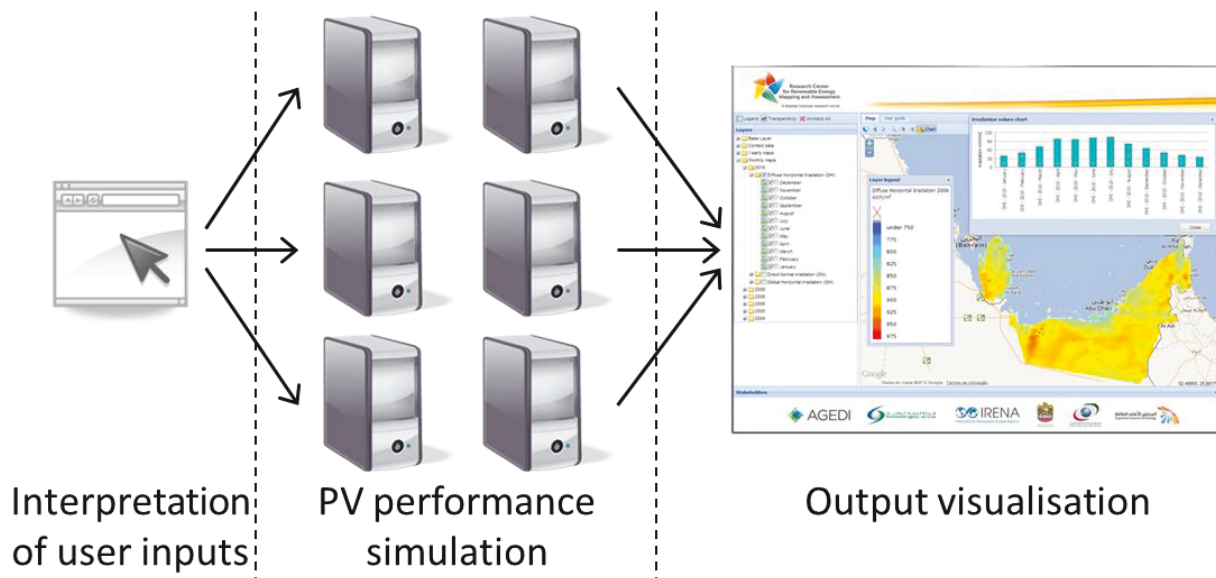


Figure 4-1. High-level algorithmic architecture of the PV performance simulator under development.

In order to run the simulator, the user specifies the area and time of interest as well as four guiding design parameters for system configuration. The area of interest is selected by means of a bounding box on the map of the graphical user interface. The bounding box is converted into a list of indices of the pixel matrix stored in the system. The pixel matrix consists of latitudes, longitudes, and elevations associated with the index of each pixel. The indices are evenly distributed into as many groups as there are processors available for the simulation. The distribution is done such that each group consists of pixels with latitudes as close to each other as possible. This is done to make it possible to design a single system configuration for all these pixels. The start and the end times defined by the user are used to define the timeframe of interest as a list of indices of the hour vector stored in the system. The hour vector covers the entire timeline available for simulation. In addition to different time values, the hour vector includes the Earth-Sun distance for every time step. The distance is used to estimate the extraterrestrial irradiance on the top of the Earth's atmosphere.

The user-given design parameters for system configuration include PV material, mounting method, and plant capacity and loading ratio. The PV material of interest is selected by choosing one of the solar module types included in the simulator's module database. The module types covered include 45 commercial solar modules and are presented in Table 4-1 and Table 4-2. The decisions on the inclusion of the module types are made based on data availability. The simulator's database consists of the mechanical, thermal, and electrical parameters of each module type included in the study. The module database is further discussed in section 4.7.

Table 4-1. Considered module types with electrical model coefficients based on third-party field tests.

Name	Material	Country of origin	Release year	Database	Source	$\eta_{mpp,STC}$	Temperature coefficient of $P_{mpp,STC}$
Canadian Solar CS5P-220M	c-Si	China	2009	SAM	SNL	15.3 %	-0.47 %/°C
Solar World SW175 Mono Sun	c-Si	Germany	2009	SAM	SNL	16.1 %	-0.48 %/°C
SunPower 128-Cell Module	c-Si	USA	2009	SAM	SNL	20.8 %	-0.41 %/°C
SunPower SPR-305-WHT	c-Si	USA	2009	SAM	SNL	21.3 %	-0.40 %/°C
Sanyo HIP-200BA19	HIT	Japan	2009	SAM	SNL	21.3 %	-0.46 %/°C
BP Solar BP3220N	mc-Si	USA	2010	SAM	SNL	14.8 %	-0.44 %/°C
BP Solar BP3180N	mc-Si	USA	2010	SAM	SNL	14.9 %	-0.42 %/°C
BP Solar BP380J	mc-Si	USA	2009	SAM	SNL	14.1 %	-0.51 %/°C
Ligitek LM220 BB00	mc-Si	Taiwan	2009	SAM	SNL	14.9 %	-0.45 %/°C
Moser Baer MBPV 220	mc-Si	India	2010	SAM	SNL	14.3 %	-0.46 %/°C
SolarFun SF220-30-P220	mc-Si	China	2010	SAM	SNL	15.9 %	-0.45 %/°C
Suntech STP200S-18-ub-1	mc-Si	China	2009	SAM	SNL	15.2 %	-0.43 %/°C
Yingli Solar YL230-29b	mc-Si	China	2009	SAM	SNL	15.8 %	-0.44 %/°C
First Solar FS-272	CdTe	USA	2009	SAM	SNL	9.9 %	-0.33 %/°C
Kaneka TSC120	a-Si	Japan	2006	PVsyst	Photon Magazine	7.0 %	-0.31 %/°C

The mounting method is chosen among three different mechanisms: fixed mount, single axis tracking, and dual axis tracking. In the case of the two former, the user additionally specifies the inclination angle. The angle refers to the tilt of POA in the case of fixed mount and to the axis tilt in the case of single axis tracking. The two tracking mechanisms under consideration are a tilted single axis tracker and a tip-tilt dual axis tracker. These tracking technologies are chosen due to their popularity among project developers. The reference single axis tracker is selected to be DEGERenergie's TOPtracker and the dual axis tracker DEGERenergie's DEGERtracker (DEGERenergie GmbH & Co. KG, 2014).

The capacity of the power station stands for the combined nominal power of the plant's all solar modules. Its unit is watt-peak (Wp). The nominal power of a module is the module's power output at STC. Based on the general scope of the project outlined in chapter 1, the plant capacities that the simulator should handle are limited to utility-scale levels. Therefore, they range from 500 kWp to 1 GWp. The fourth user-given design parameter, loading ratio, is used for configuring the inverters of the plant. The parameter stands for the ratio of the capacity of a power block, which consists of modules connected to a single inverter, to the AC output power rating of the inverter. If the simulator's system configuration algorithm is made to multiply identical power blocks to obtain the configuration of the entire plant, loading ratio can be defined as the ratio of the plant capacity to the combined nominal AC output power of the plant's inverters. The simulator under development should allow for a loading ratio ranging from 50% to 150% in order to cover all ratios normally used in utility-scale power plants. However, all combinations of capacity and loading ratio are not possible even if they are within the defined limits due to the modular architecture of a PV power station and the inverter-specific limitations for array configuration. Due to the good

availability of performance data, SMA Solar Technology's SMA SUNNY CENTRAL MV series is used as the reference set of inverters (SMA Solar Technology AG, 2014). The capacities of the seven inverters are approximately 500 kW, 630kW, 800kW, 1000 kW, 1250 kW, and 1600 kW. Since the purpose of the simulator is not to focus on the evaluation of power conditioning technologies, the reference inverters do not have to represent different manufacturers. For the same reasons as with inverters, the reference generator junction box is chosen to be Gustav Hensel's Mi PV 3941 (Gustav Hensel GmbH & Co. KG, 2014).

Table 4-2. Considered module types with electrical model coefficients based on data provided by manufacturers.

Name	Material	Country of origin	Release year	Database	Source	$\eta_{mpp,sc}$	Temperature coefficient of $P_{mpp,sc}$
Canadian Solar CS6X 320M	c-Si	China	2013	PVsyst	Manufacturer	18.6 %	-0.45 %/°C
JA Solar JAM6 R 72 340	c-Si	China	2014	PVsyst	Manufacturer	19.4 %	-0.42 %/°C
Jinko Solar JKM 315M 72	c-Si	China	2013	PVsyst	Manufacturer	18.4 %	-0.41 %/°C
ReneSola JC270S 24Bb	c-Si	China	2012	PVsyst	Manufacturer	18.5 %	-0.44 %/°C
SunPower SPR-455J-WHTD	c-Si	USA	2012	PVsyst	Manufacturer	22.7 %	-0.33 %/°C
Panasonic VBHN240SE10	HIT	Japan	2012	PVsyst	Manufacturer	22.0 %	-0.29 %/°C
Canadian Solar CS6X 320P	mc-Si	China	2013	PVsyst	Manufacturer	18.3 %	-0.43 %/°C
Conergy E 250P	mc-Si	Germany	2013	PVsyst	Manufacturer	17.1 %	-0.44 %/°C
Hanwha Qcells QPRO L 315	mc-Si	Germany	2013	PVsyst	Manufacturer	18.0 %	-0.42 %/°C
Hanwha HSL 72P6 PC 7 315	mc-Si	China	2014	PVsyst	Manufacturer	18.0 %	-0.44 %/°C
JA Solar JAP6 72 330 3BB	mc-Si	China	2014	PVsyst	Manufacturer	18.8 %	-0.43 %/°C
Jinko Solar JKM 310P 72	mc-Si	China	2013	PVsyst	Manufacturer	17.7 %	-0.43 %/°C
Kyocera KD315GX LPB	mc-Si	Japan	2011	PVsyst	Manufacturer	16.2 %	-0.45 %/°C
REC 260PE	mc-Si	Norway	2012	PVsyst	Manufacturer	17.8 %	-0.40 %/°C
ReneSola JC310M 24Ab	mc-Si	China	2012	PVsyst	Manufacturer	17.7 %	-0.40 %/°C
Sharp ND R250A5	mc-Si	Japan	2011	PVsyst	Manufacturer	17.1 %	-0.43 %/°C
SolarWorld SW 250 Poly	mc-Si	Germany	2011	PVsyst	Manufacturer	17.1 %	-0.48 %/°C
Trina Solar TSM 310 P14A	mc-Si	China	2012	PVsyst	Manufacturer	17.7 %	-0.42 %/°C
Yingli Solar YL310P 35b	mc-Si	China	2014	PVsyst	Manufacturer	17.7 %	-0.41 %/°C
Inventux X94A	a-Si	Germany	2009	PVsyst	Manufacturer	7.2 %	-0.26 %/°C
NexPower NH100AT 5A	a-Si	Taiwan	2009	PVsyst	Manufacturer	7.3 %	-0.20 %/°C
Inventux X140 125	a-Si/ μ c-Si	Germany	2010	PVsyst	Manufacturer	10.6 %	-0.31 %/°C
NexPower NT 170AX	a-Si/ μ c-Si	Taiwan	2012	PVsyst	Manufacturer	11.7 %	-0.30 %/°C
Sharp NA-E140L5	a-Si/ μ c-Si	Japan	2013	PVsyst	Manufacturer	10.8 %	-0.30 %/°C
Calyxo CX65	CdTe	Germany	2010	PVsyst	Manufacturer	10.0 %	-0.33 %/°C
FirstSolar FS3100 Plus	CdTe	USA	2014	PVsyst	Manufacturer	15.3 %	-0.31 %/°C
Avancis PowerMax STRONG 140W	CIS	Germany	2012	PVsyst	Manufacturer	14.0 %	-0.40 %/°C
SolarFrontier SF170 S	CIS	Japan	2013	PVsyst	Manufacturer	15.2 %	-0.32 %/°C
Solibro SL2-125	CIS	Germany	2014	PVsyst	Manufacturer	14.6 %	-0.37 %/°C
Stion STN150	CIS	USA	2013	PVsyst	Manufacturer	15.1 %	-0.35 %/°C

4.3 System Configuration

System configuration essentially defines how the power station, whose performance is simulated, is structured. Therefore, it greatly influences the outcome of the simulation although it cannot be considered as a performance simulation step. The system configuration of the power station is defined based on the user-defined design parameters and the technological system input variables: physical module and inverter parameters. Hence, it can be considered as a bridge between the user's inputs and the actual performance simulation.

The first step of the system configuration process is to define the number of modules in an array, N_{mod} . As discussed in section 2.3.5, regions characterised by high ambient air temperatures favour high nominal system voltage levels. That is why here, N_{mod} is computed based on the maximum voltage that can

be input into an inverter, $V_{dc,max}$. As all the inverters included in the simulator's database have the same $V_{dc,max}$ (1 kV), N_{mod} can be computed before selecting the inverters to be deployed in the configuration. N_{mod} is calculated based on Eq. 4.1-2 depending on the mounting method:

- Fixed mount and single axis tracking

$$N_{mod} = 2 \left\lceil \frac{V_{dc,max}}{2V_{OC}} \right\rceil \quad (4.1)$$

- Dual axis tracking

$$N_{mod} = 4 \left\lceil \frac{V_{dc,max}}{2V_{OC}} \right\rceil \quad (4.2)$$

The different equations for fixed mount and single axis tracking systems on one hand and for dual axis tracking ones on the other are due to the typical array configurations used in association with these mounting methods. The fixed mount and single axis tracking arrays are assumed to be long strings only consisting of series-connected modules. In order to ensure high enough number of modules also in the case of tip-tilt dual axis tracking systems characterised by roughly square-shaped arrays, the arrays are assumed to consist of two strings in parallel.

The second step is the determination of row spacing. The distance between arrays is minimized so that on a horizontal ground in the case of fixed mount, there is no shading on modules due to other arrays three hours after the solar noon on the winter solstice. With tracking systems, the constraint is one hour stricter resulting in wider row spacing. The variation in the constraint aims to address the differences between the cost structures of fixed mount and tracking systems. The distances can be computed based on N_{mod} , module dimensions, solar angles at the specified times, and the tilt angle specified by the user. Due to different row spacing requirements, the configuration depends on the site latitude and, therefore, varies between the groups allocated to different processors.

The following formulae, Eq. 4.3-7, can be used to obtain the row spacing for different array configurations. The minimum north-south distance between arrays with a fixed tilt $d_{a,0t}$ can be calculated by means of Eq. 4.3. In the case of single axis tracking, the north-south distances between arrays $d_{a,1t,NS}$ can be obtained through Eq. 4.4 and the east-west distance between axes $d_{a,1t,EW}$ through Eq. 4.5. The axis rotation angle equation derived by Narvarte and Lorenzo (2008) is used in the formulation of the latter two equations. Eq. 4.6 addresses the north-south distance $d_{a,2t,NS}$ and Eq. 4.7 the east-west distance $d_{a,2t,EW}$ between axes in the case of dual axis tracking.

$$d_{a,0t} = \frac{2l_{mod} \cdot \sin \beta \cdot \cos \varphi_{S,d}}{\cot \theta_z} \quad (4.3)$$

$$d_{a,1t,NS} = \frac{\left[\frac{N_{mod} \cdot w_{mod} \cdot \sin \tau}{2} + 2l_{mod} \sin \left(\arctan \left\{ \frac{\sin \theta_z \cdot \sin \varphi_{S,d}}{\sqrt{(\sin \theta_z \cdot \cos \varphi_{S,d})^2 + \cos^2 \theta_z} \cdot \sin \left[\arctan \left(\frac{\cos \theta_z}{\sin \theta_z \cdot \cos \varphi_{S,d}} \right) + \tau \right]} \right\} \right) \right] \cos \varphi_{S,d}}{\cot \theta_z} \quad (4.4)$$

$$d_{a,1t,EW} = \frac{\left[\frac{N_{\text{mod}} \cdot w_{\text{mod}} \cdot \sin \tau}{2} + 2l_{\text{mod}} \sin \left(\arctan \left\{ \frac{\sin \theta_z \cdot \sin \varphi_{S,d}}{\sqrt{(\sin \theta_z \cdot \cos \varphi_{S,d})^2 + \cos^2 \theta_z} \cdot \sin \left[\arctan \left(\frac{\cos \theta_z}{\sin \theta_z \cdot \cos \varphi_{S,d}} \right) + \tau \right]} \right\} \right) \right] \sin \varphi_{S,d}}{\cot \theta_z} + \frac{2l_{\text{mod}}}{\cos \left(\arctan \left\{ \frac{\sin \theta_z \cdot \sin \varphi_{S,d}}{\sqrt{(\sin \theta_z \cdot \cos \varphi_{S,d})^2 + \cos^2 \theta_z} \cdot \sin \left[\arctan \left(\frac{\cos \theta_z}{\sin \theta_z \cdot \cos \varphi_{S,d}} \right) + \tau \right]} \right\} \right)}$$
(4.5)

$$d_{a,2t,NS} = \begin{cases} 6l_{\text{mod}} \cdot \sin \theta_z \cdot \cos \varphi_{S,d} + \frac{1}{3} N_{\text{mod}} \cdot w_{\text{mod}} \cdot \sin \varphi_{S,d}, \varphi_{S,d} \leq \varphi_{S,\text{max}} \\ 6l_{\text{mod}} \cdot \sin \theta_z \cdot \cos \varphi_{S,\text{max}} + \frac{1}{3} N_{\text{mod}} \cdot w_{\text{mod}} \cdot \sin \varphi_{S,\text{max}}, \varphi_{S,d} > \varphi_{S,\text{max}} \end{cases}$$
(4.6)

$$d_{a,2t,EW} = \begin{cases} 6l_{\text{mod}} \cdot \sin \theta_z \cdot \sin \varphi_{S,d} + \frac{1}{3} N_{\text{mod}} \cdot w_{\text{mod}} \cdot \cos \varphi_{S,d}, \varphi_{S,d} \leq \varphi_{S,\text{max}} \\ 6l_{\text{mod}} \cdot \sin \theta_z \cdot \sin \varphi_{S,\text{max}} + \frac{1}{3} N_{\text{mod}} \cdot w_{\text{mod}} \cdot \cos \varphi_{S,\text{max}}, \varphi_{S,d} > \varphi_{S,\text{max}} \end{cases}$$
(4.7)

where l_{mod} stands for the length of the longer side of a module, w_{mod} for that of the shorter side, $\varphi_{S,d}$ for the Sun's azimuth angle three or four hours after the solar noon on the winter solstice (0-90°), τ for the axis tilt angle, and $\varphi_{S,\text{max}}$ for the Sun's azimuth angle when the minimum distance between the axes of different tracking systems reaches its maximum.

After specifying N_{mod} and row spacing between arrays, the actual number of arrays N_a , capacity P_{stc} , and loading ratio r of the power plant can be computed. The system configuration programme finds the configuration which provides the best match between the input combinations given by the user and the actually possible combinations of the inputs. As real PV power stations consist of modular building blocks, solar modules and inverters, P_{stc} and r cannot equal the ones desired by the user most of the times. Instead, the simulator always finds the closest possible fit by minimising the sum of relative differences between the actual and desired capacities and between the actual and desired loading ratios. The corresponding optimisation problem is expressed by Eq. 4.8.

$$\min : \frac{|P_{\text{stc},\text{desired}} - P_{\text{stc}}|}{P_{\text{stc},\text{desired}}} + \frac{|r_{\text{desired}} - r|}{r_{\text{desired}}}$$

(4.8)

s.t.

$$N_a < \frac{N_i I_{dc,\text{max}}}{I_{sc}}$$

As can be seen from Eq. 4.8, the maximum input current to the inverter $I_{dc,\text{max}}$ also limits the number of arrays.

After computing N_{mod} , N_a , P_{stc} , r , and row spacing between the arrays, the total surface areas of the AC power blocks and the entire power station can be calculated. As all the dimensions of the power station are known, the computation of the lengths of the cable runs is finally possible. There are three to four levels of cable runs in the reference power station connecting arrays to an array junction box (solar cable), array junction boxes to a generator junction box (array main cable), generator junction boxes to an inverter (DC main cable), and inverters to the grid connection point (AC main cable). The plant is equipped with array junction boxes only if the number of arrays in an AC power block exceeds 192, which is the product of the maximum number of inlets at the reference junction box (24) (Gustav Hensel GmbH & Co. KG, 2014) and the maximum number of inlets at the reference inverters (8) (SMA Solar Technology AG, 2014). In order to estimate the exact cable lengths, the placing of AC power blocks, power conditioning units, and junction boxes needs to be defined.

An AC power block consists of the arrays connected to a single inverter. The guidelines for placing AC power blocks with respect to each other are illustrated in Figure 4-1. In the case of more than one inverter, the power units aligned in the east-west direction are denoted as lines, whereas the units aligned in the north-south direction are denoted as columns. The number of columns should always be either equal to or one more than the number of lines. The units comprising the incomplete line or column should be placed centrally on the southern (lines) or eastern (columns) side and the grid connection point on the northern side with respect to the full lines or columns. Within a power unit, the medium voltage transmission line from inverters to the grid connection point is always laid parallel to the columns. Between two power units however, the transmission lines are laid perpendicular to the columns if the length of additional cable trenches required can be so reduced as in the case of eight inverters in Figure 4-2.

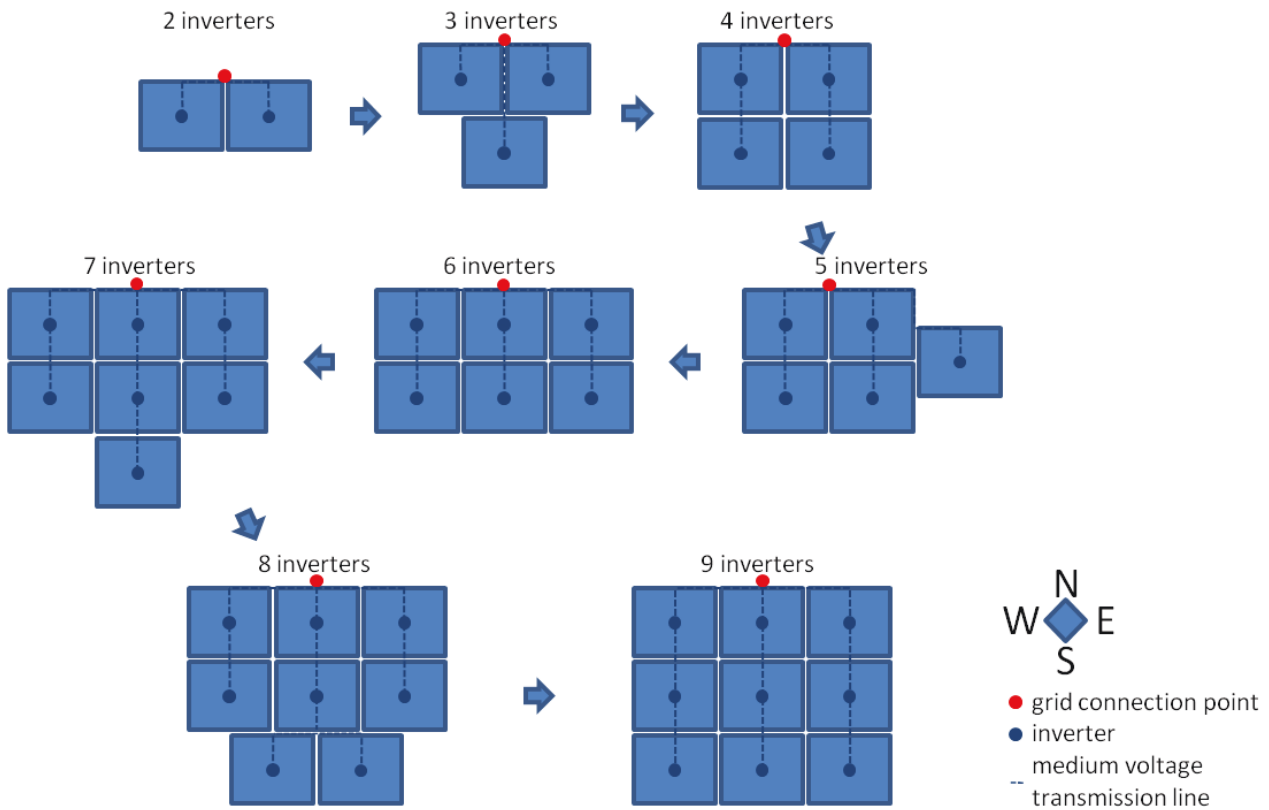


Figure 4-2. Guidelines for placing AC power blocks in the reference design.

A power conditioning unit is always placed in the middle of its power unit so that there are equally many full rows of arrays on its all sides. Instead of complying with Eq. 4.5 and Eq. 4.7, the width of the row spacing between the western and eastern halves of the power unit might also depend on the inverter and transformer dimensions. This is the case if the distance calculated by means of Eq. 4.5 or Eq. 4.7 is shorter than 9 m. In these cases, the distances equal 9 m. If tracking is not used however, the east-west distance between arrays equals 1 m in the case of an empty row and 6 m in the case of an inverter. The north-south distances always comply with Eq. 4.3-4 and Eq. 4.6.

All junction boxes are located under the arrays of two rows, denoted as junction rows here, parallel to the inverter row in the middle of the unit. If there is an even number of north-south array rows on each side of the inverter row, the boxes are installed under the arrays of the one of the two midmost array rows closest to the inverter row as shown in the example of Figure 4-3. In the case of an odd number of the rows, the boxes are placed under the arrays of the single midmost row as illustrated in Figure 4-4. Under the arrays with fixed mount or single axis tracking, the boxes are located at a corner of the horizontal projection of the arrays above them: at the north-eastern corner in the case of a single midmost row on the western half (Figure 4-4) or in the case of two midmost rows on the eastern half (Figure 4-3) and at the north-western one in the opposite cases. In the case of dual axis tracking, the boxes are always assumed to be placed right next to tracker axes.

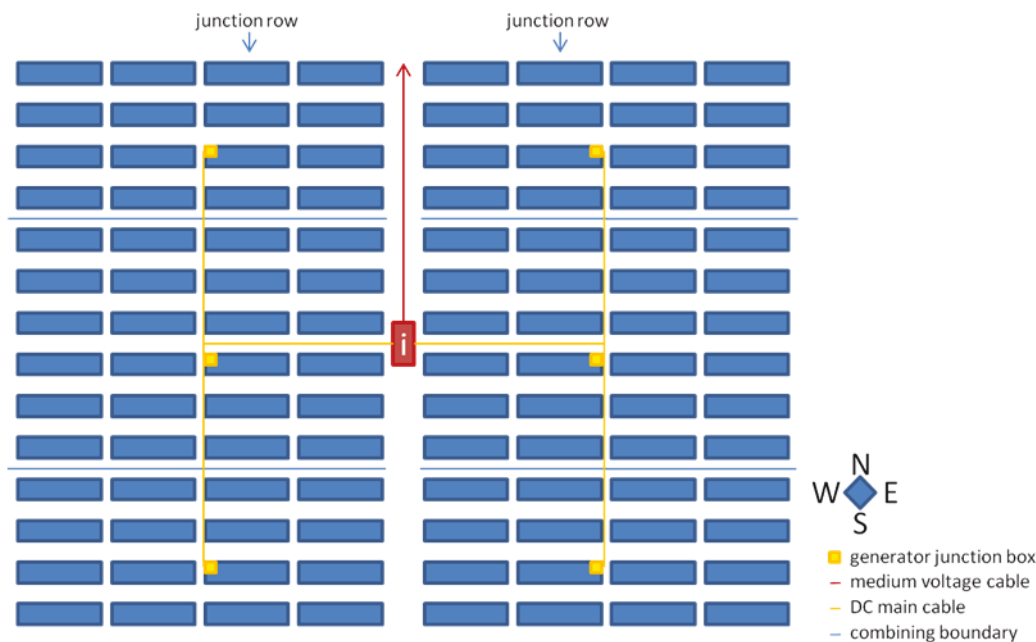


Figure 4-3. Example of junction box placing in the case of an even number of north-south array rows with fixed mount on each side of the inverter.

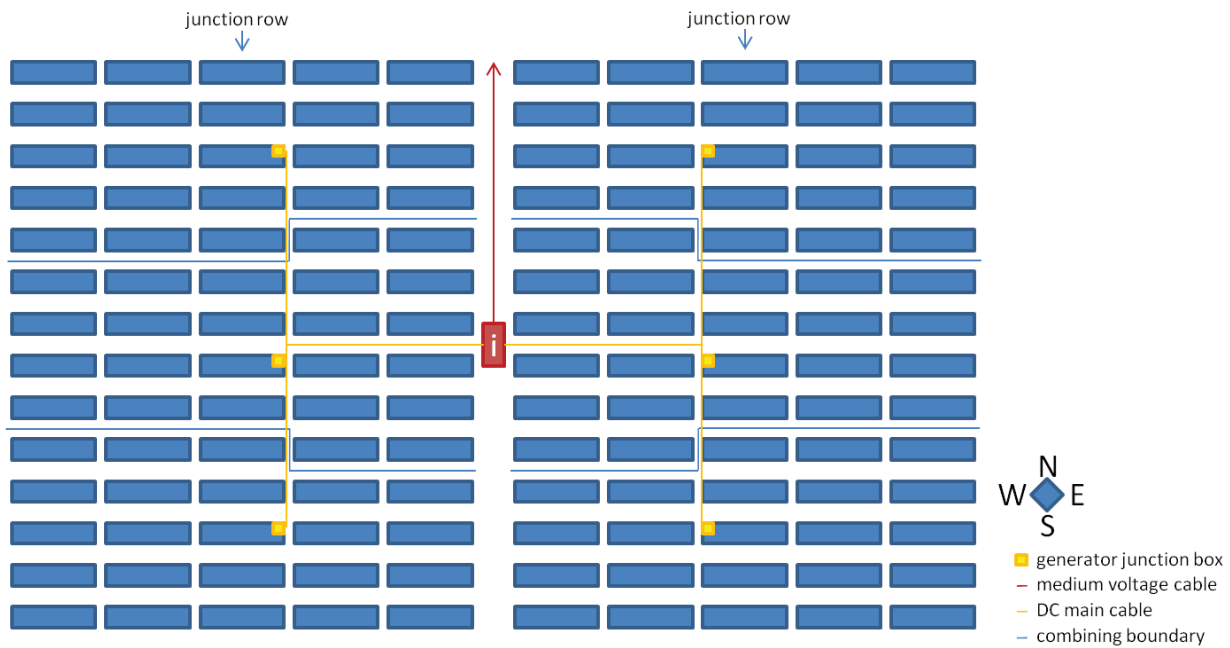


Figure 4-4. Example of junction box placing in the case of an odd number of north-south array rows with fixed mount on each side of the inverter.

The blue lines in the examples of Figure 4-3 and Figure 4-4 represent the boundaries between the areas from whose arrays each generator junction box combines current flows. The number of arrays combined by a junction box always equals 24 in the case of combining areas located between other combining areas. In the periphery of the power unit however, these areas may comprise fewer than 24 arrays as can be seen from Figure 4-3 and Figure 4-4. The mutual symmetry of the combining areas is optimized by minimizing the difference between the numbers of arrays each of the four peripheral combining areas consists of. In the case of 12 or fewer arrays however, this symmetry rule is renounced by distributing combining areas of 24 arrays to all junction boxes except for the two southernmost boxes. When an east-west array row is divided between two junction boxes, the arrays located nearer to the inverter row are combined with the east-west array rows located nearer to the inverter as presented in Figure 4-4. The junction box of a combining area is located in the midmost east-west array row of the area. In case there are two midmost rows, the box is always installed in the more southern one. In case there are both array and generator junction boxes in the power station, the above discussion applies only to array junction boxes. In this case, there is always an even number of generator junction boxes in both halves of an AC power block and therefore, the combining areas of the generator junction boxes only consist of entire combining areas of array junction boxes. The generator junction boxes are placed in the junction row so that the combined cable run length from array junction boxes is minimised.

Solar cables are used to connect arrays to junction boxes. The guidelines for the layout of solar cables are given in Figure 4-5. The combining area illustrated in the figure includes 24 arrays and, therefore, 24 solar cables with varying lengths and cross-section areas. Because both the positive and negative terminals of an array need to be connected to the circuit with a junction box, the length of a required solar cable is calculated based on the distance between the box and the middle point of the shorter side of the array as shown in the case of fixed mount in Figure 4-5. The same principle can be applied to systems with

single axis tracking. In the case of dual axis tracking however, solar cables are laid starting from tracker axes in the middle of the arrays.

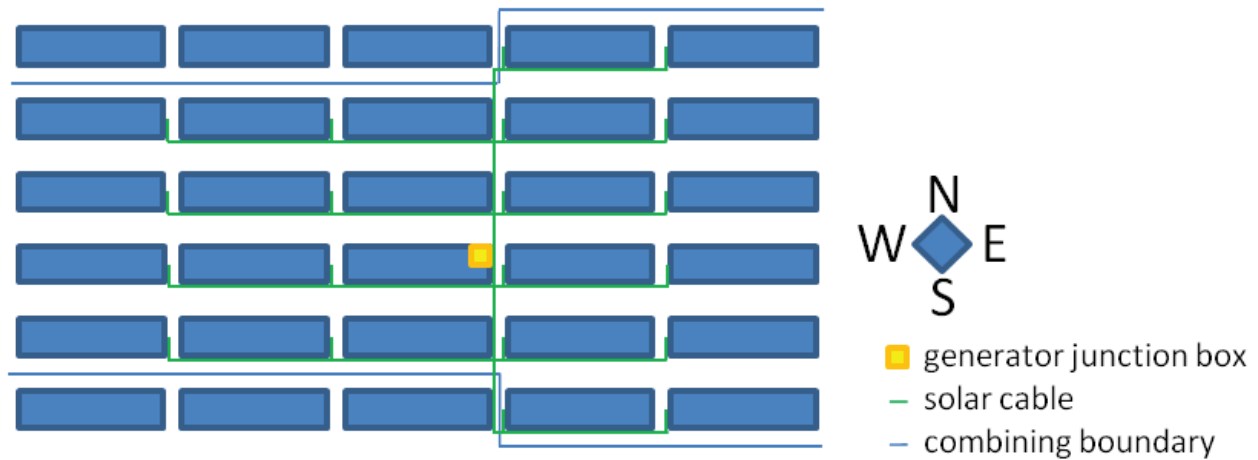


Figure 4-5. Guidelines for laying solar cables in the reference design with fixed mount.

After calculating the lengths for all cable run, the system configuration programme finds the optimal cross-section areas and cable numbers for each cable run. The UAE's electricity wiring regulations allow only stranded copper conductors to be used in circuits with fixed wiring (Regulation and Supervision Bureau, 2009). In the model therefore, the material is assumed to be copper. The optimisation between cost and voltage drop is done by means of junction boxes that enable using different sizes of wires between arrays and inverter. The selection of the conductor size is dependent on the maximum allowable voltage drop for long-term operation and the current carrying capacity of the conductor. The combined long-term voltage drop from an array to an inverter must not exceed 2 per cent in the case of any array-inverter combination. In this study, the maximum allowable voltage drop is based on module and inverter parameters under standard conditions. An optimization problem can be used to derive the lowest possible total conductor volume while keeping voltage drop at an acceptable level and conductor current carrying capacities sufficient (with a temperature correction factor of 0.91 based on the BS 7671 specifications (Institution of Engineering & Technology, 2008)). Through solving the problem, a set of conductors with optimal cross-section areas and numbers can be found.

4.4 Optical Model

As explained in section 3.1, the purpose of the optical model is to estimate W_{poa} based on ambient data and system configuration and then correct it to account for the angular reflection and soiling losses. The Perez model (see Eq. 3.7-8 in section 3.1.1) is selected to be the simulator's transposition model, which is used to calculate W_{poa} . There are two main reasons for the decision. First, due to its popularity, the model has been tested in a large variety of locations. In most of the Middle East-based validation studies reviewed (Evseev and Kudish, 2009; Kamali et al., 2006; Khalil and Shaffie, 2013; Noorian et al., 2008), the model showed good or average performance. Second, even if the model turns out to perform poorly under the conditions of the Arabian Peninsula, it can be recalibrated thanks to its semi-empirical nature.

In order to run the Perez sky diffuse model, four parameters need to be computed: clearness level, relative optical air mass, brightness level, and ϑ . In the case of tracking systems, the estimation of ϑ requires a model for backtracking. The backtracking algorithm of the model is developed based on the

shading geometry formulations outlined by Narvarte and Lorenzo (2008). Based on the same paper, also shading losses are estimated in the case of fixed mount. As explained in section 3.1, only DNI is assumed to be affected by shading. In the case of tracking systems, the backtracking switch is controlled only by the shading cast by the neighbouring arrays in the east-west direction. Array self-shading is assumed to be the only source of shading due to the fact that most of the other causes for shading can be minimised by careful site selection.

Diffuse sky radiation is an input to the final W_{eff} modelling tool, which is developed as a combination of the Perez transposition model (Perez et al., 1990) and Martín and Ruiz's (2002) model for angular reflection soiling losses (see Eq 3.9 in section 3.1.2). The model is expressed in Eq. 4.9:

$$W_{\text{eff}} = W_{b,n} \cos \theta (1 - F_b) + W_{d,h} \left[\frac{1 + \cos \beta}{2} (1 - F_1) + F_1 \frac{a}{b} + F_2 \sin(\beta) \right] (1 - F_d) + \rho W_{g,h} \frac{1 - \cos \beta}{2} (1 - F_r) \quad (4.9)$$

Martín and Ruiz's model was selected due to its unique way to combine the effects of angular reflection losses and soiling. Under dynamic dust transport conditions as in the Persian Gulf region, it is important that the optical model enables dust corrections in a physically justifiable way rather than through, for instance, fixed percentage reductions in P_{ac} .

4.5 Spectral Model

Originally, Martín and Ruiz's (1999) spectral correction model has been implemented in the simulator as it can be easily integrated in Eq. 4.9. With the spectral model, W_{eff} estimates, however, have become unrealistically high at certain hours of the day and with certain technologies. Consequently, the model has been removed from the simulator. Therefore, the W_{eff} estimates produced by the current version of the model are not spectrally corrected. Currently, a validation study is being undertaken to calibrate Martín and Ruiz's model for the local conditions.

4.6 Thermal Model

Tuomiranta et al. (2013) find the Schott model (tool # 15 in section 3.3) to be the most suitable thermal model for solar cells under hot desert conditions in Abu Dhabi. Shown by a later study by ReCREMA, the Schott model, in fact, shows the best performance with all PV materials according to the measurements made at the PV test field in Masdar City. For this reason, the Schott model is chosen to be implemented in the simulator as its thermal model. Table 4-3 presents the PV material-specific Schott model coefficients derived based on test field measurements in Masdar City and stored in the simulator's module database.

Table 4-3. Schott model coefficients for different PV materials derived based on test field measurements in Masdar City.

PV material	θ_1	θ_2	θ_3	θ_4
c-Si	141.15	0.2062	29.502	1.6747
HIT	111.50	1.3252	30.107	1.7937
mc-Si	91.94	1.4037	27.204	1.4805
a-Si	165.59	-0.3899	30.259	1.8016
a-Si/ μ c-Si	97.74	1.8850	31.527	2.0213
CdTe	152.33	-0.8446	25.387	1.1341
CIS/CIGS	128.33	0.3665	26.655	0.6867

4.7 Electrical Model

SAPM (King et al., 2004) is selected as the simulator's electrical model for generation for three reasons. Most importantly, SNL maintains a database of dozens of modules with empirically derived SAPM coefficients (Sandia National Laboratories, 2014a). No other PV performance model is supported by such amount of publicly available third-party field test (TPFT)-based data. Secondly, amongst the three models under comparison, SAPM is the only model that is analytically solvable. The other two models would require numerical analysis to be solved. The third advantage is that when T_c in the SAPM power equation ($I_{mpp} * V_{mpp}$) is substituted by the Schott model equation, the model is still analytically solvable in spite of the coupled relationship between η_c and T_c . In addition to the thermal model substitution, the SAPM-based power equation is multiplied by the technology-specific and past operating life-dependent degradation coefficient derived from Jordan et al. (2012) Finally, the array power output is multiplied by 0.98 to account for mismatch losses as done in the default mode of PVsyst (PVsyst SA, 2014b).

Due to the selection of SAPM as the simulator's electrical model, only those solar module types for which the Sandia module model coefficients can be derived are selected. Two sources of module performance data are used when estimating these coefficients: System Advisor Model's (SAM) module library provided by SNL and the module performance database incorporated in PVsyst 6. The Sandia module model coefficients can be directly extracted from the SAM module library whereas in the case of PVsyst's database, the coefficients are approximated through regression of PVsyst's single diode model output in various ambient conditions. 14 out of the 45 selected modules are chosen from the SAM module library and the remaining 31 from PVsyst. Out of the 31, one module type has been assessed by an independent testing organisation (Photon Magazine) and the rest by the respective manufacturers. The data for the 14 modules from the SAM library are entirely based on field data collected by SNL. The comparative performance assessment summarised in section 5.2.2 is conducted separately for the data collected by TPFT and the data provided by the manufacturers. As can be seen from Table 4-1 in section 4.2, the module data provided by the testing organisations are outdated and represent only five different PV materials. Therefore, in order to take the recent technological development into consideration and expand the technological scope of the simulator, it is necessary to also analyse data produced by manufacturers. In addition to the Sandia module model coefficients, basic mechanical and electrical module parameters are extracted from the same two databases.

DC transmission losses are calculated based on the ohmic, quadratic relationship of Joule heating and current. In case V_{dc} is too low or I_{dc} or V_{dc} too high at the inverter inlet, the simulator simulates an approximated I-V characteristic curve based on the five points given by SAPM and forces the modules downwards on their I-V curves. Finally, P_{ac} is computed as the output of SIPM. SIPM is selected as the electrical model for power conditioning due to SNL's inverter database which consists of dozens of inverters with measured SIPM coefficients (Sandia National Laboratories, 2014b). Therefore, SIPM facilitates the inclusion of a wider range of different inverters if need be in the future. At the end, the self-consumption due to possible tracking systems is subtracted from P_{ac} . Other self-loss components will be added in the future if relevant data are found.

4.8 Output Processing

The final product of the actual performance simulation process consists of as many P_{ac} time series as there are sites to be analysed. The time series are the basis for the computation of the simulator's main output data. These spatial data comprise two performance indicators, capacity factor CF (Eq. 4.10) and performance ratio PR (Eq. 4.11). The indicators are formulated mathematically in the below equations

where Y stands for the total yield for the entire time of interest, P_{stc} for the nominal generation capacity of the power station, t for the number of hours included in the time of interest, and W_{eff} for the average effective irradiance level in each hour.

$$CF = \frac{Y}{P_{stc} t} \quad (4.10)$$

$$PR = \frac{Y}{P_{stc}} \cdot \frac{1000W/(m^2h)}{\sum_{t=1}^{t_{end}} W_{eff}} \quad (4.11)$$

CF gives a general idea of the goodness of the combination of a site location and selected technologies. The indicator is affected by both the abundance of solar resource and the performance of the selected technologies in real operating conditions. The performance of solar modules in the standard test conditions (P_{stc}) does not, however, have an impact on CF due to the normalisation by P_{stc} . In contrast to CF , PR is not influenced by the level of solar resource because the indicator is constructed by normalising the full load-equivalent operating hours (FLH) (Y/P_{stc}) by the annual effective irradiation incident on the module. In this way, the linear effect of incoming irradiance on the short-circuit current of solar cells can be isolated. Hence, PR can be used to compare the suitability of a module technology between site locations with different solar resource levels. In addition to the performance indicators that are finally converted into maps, the simulator produces a detailed listing of system configuration parameters for each location.

5. Case Study – PV Performance in the Arabian Peninsula

The case analysis presented in this chapter focuses on the performance assessment of PV power stations in the Arabian Peninsula. The analysis specifically aims to answer how different design parameters influence PV performance and how the impacts vary with time and location. The different parameters covered in the assessment include PV material, mounting method, plant capacity, and loading ratio.

The study is based on the in-situ observations of meteorological parameters performed at undisclosed solar resource monitoring stations. Hence, it is a point-based assessment, and no spatial interpolation will be done based on these data. PV performance is assessed by means of the PV performance simulator developed as part of this thesis project. The PV module types included in the analysis span the entire range of different materials used for PV devices.

The chapter is composed of two main components. The first subsection describes the spatial and temporal variability of the meteorological data used in the analysis. The actual results of the study are presented in the second subsection and reflected back to the first one in order to formulate causal relationships between the inputs and the outputs. Finally, the validity and reliability of the results are discussed in the third subsection.

5.1 Spatiotemporal Input Variables

The spatiotemporally variable input data comprise measurements made at 12 monitoring stations in the Arabian Peninsula over a period of one year from the beginning of August till the end of July. The measured parameters include irradiance as well as ambient air temperature and wind speed. In addition to the meteorological parameters, parameters defining the Sun's position with respect to the Earth are required as inputs for the simulation. The temporal resolution of the simulation is one hour.

The annual global horizontal irradiation levels presented in Figure 5-1 show that the Arabian Peninsula has exceptionally abundant solar resources. Over the selected time span of one year, the global irradiation ranged between 2150 kWh/m² and 2360 kWh/m² at the 12 monitoring stations considered in the study. The highest global irradiation levels were measured at Region 1's three stations: Site G, Site I, and Site H. The variability in the annual global irradiation is low considering the geographical dispersion of the stations. By contrast, the annual direct normal irradiation experiences significant variation ranging from 1850 kWh/m² to 2610 kWh/m². As can be seen from Figure 5-1, the division of the data into three geographical segments can be justified on the grounds that on average, the stations located in Region 2 have the lowest DNI levels and the ones in Region 3 the highest.

The seasonal variation in daily average irradiation levels can be studied by looking at Figure 5-2 for Region 1, Figure 5-3 for Region 2, and Figure 5-4 for Region 3. Due to the Arabian Peninsula's location in the northern hemisphere, daily average global horizontal irradiation levels peak (7.9-9.2 kWh/m²) in July and reach the minimum (3.4-4.6 kWh/m²) in December or in January in every region. The exact minimum months vary because atmospheric scattering follows different seasonal cycles across the peninsula. Interestingly, all sites experience a seasonal peak in DNI just before the vernal equinox, in February in Region 1 and Region 3 and in March in Region 2. The highest seasonal variability can be found in Region 3 whose stations experience the country's lowest average GHI levels in the winter and the highest in the summer. This is due to the low level of atmospheric scattering throughout the year. The variation of irradiance follows the seasonal cycle of the Sun's position more closely in Region 3 as the changing cosine

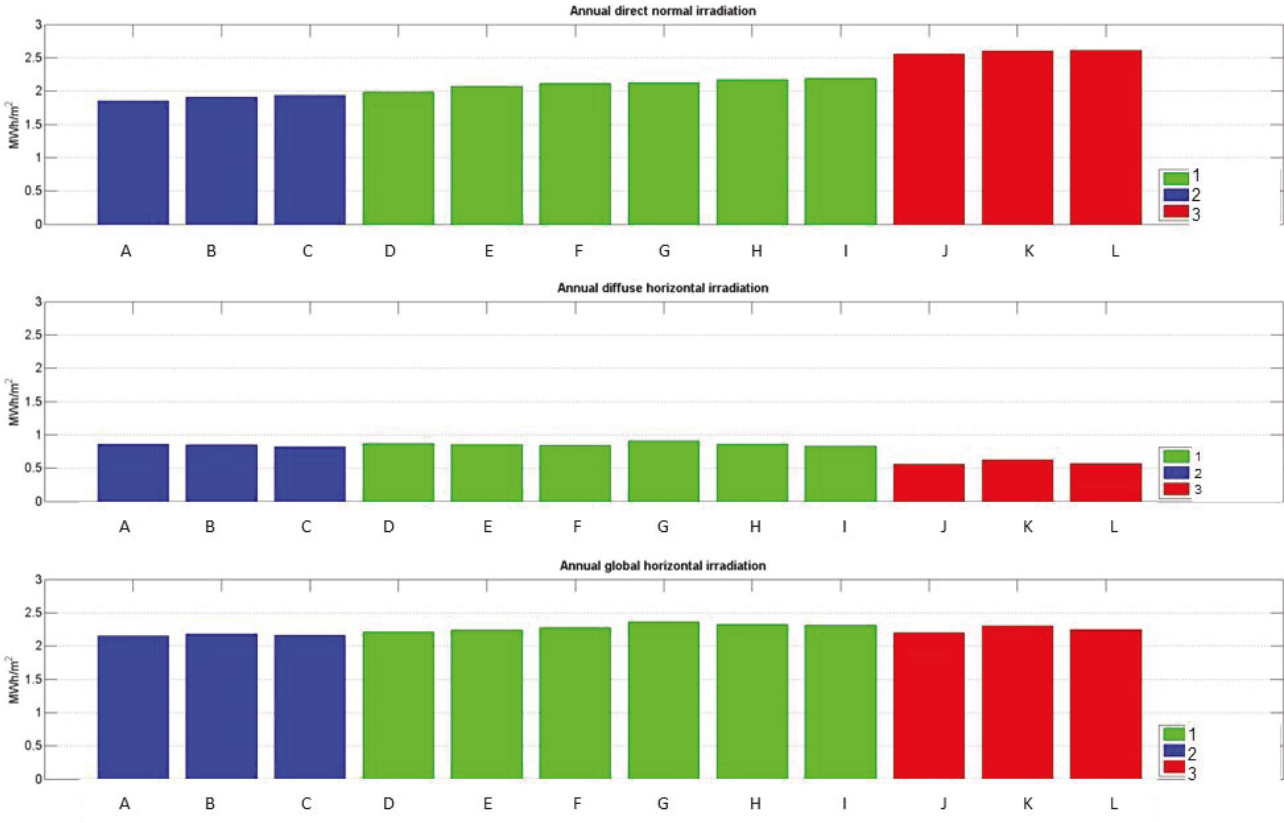


Figure 5-1. Annual irradiation at each monitoring station considered in the study.

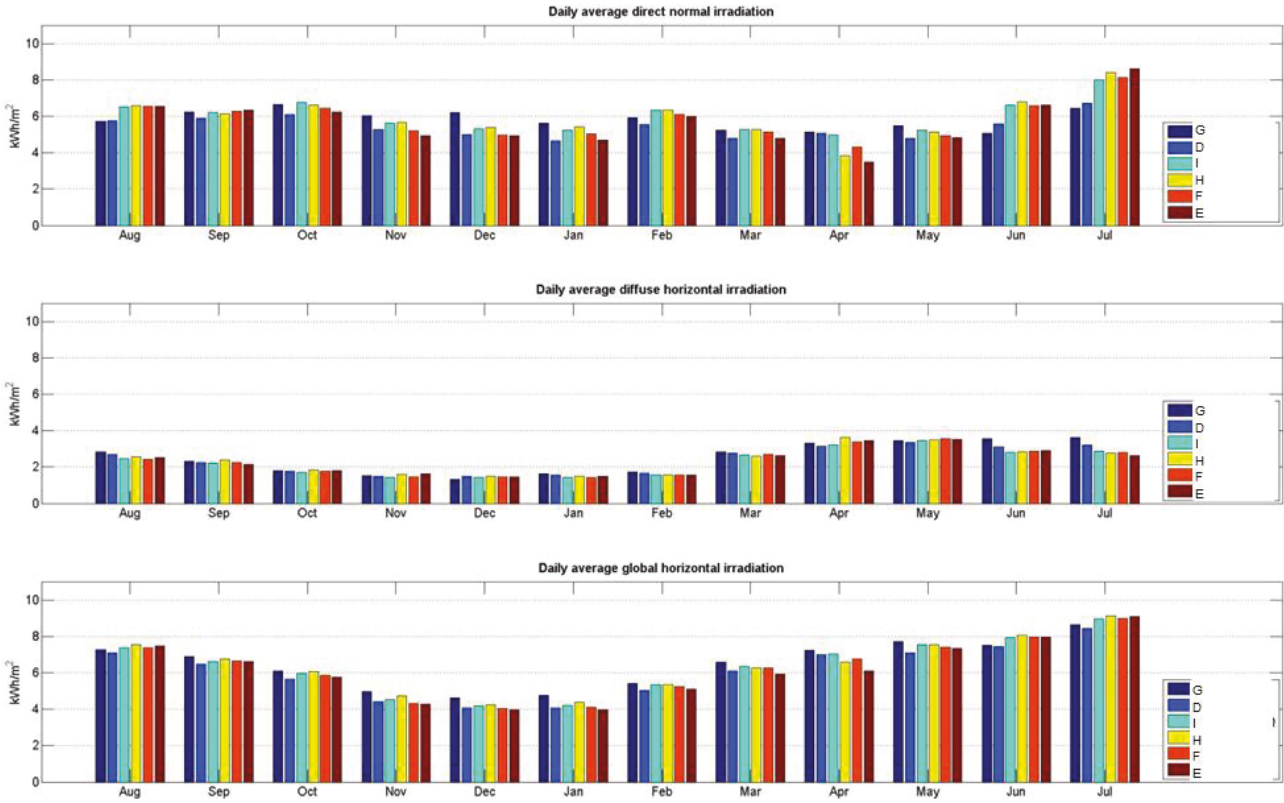


Figure 5-2. Daily average irradiation levels in Region 1 in each month of the study period.

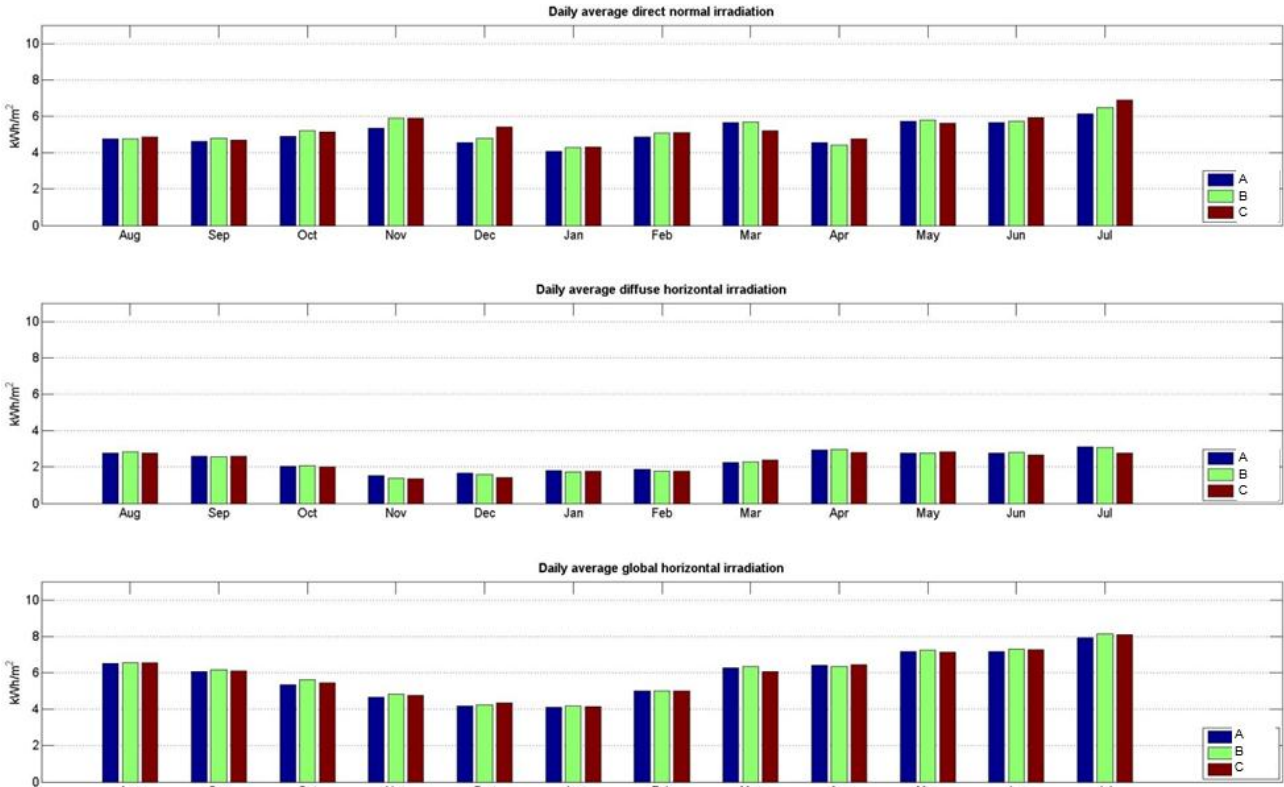


Figure 5-3. Daily average irradiation levels in Region 2 in each month of the study period.

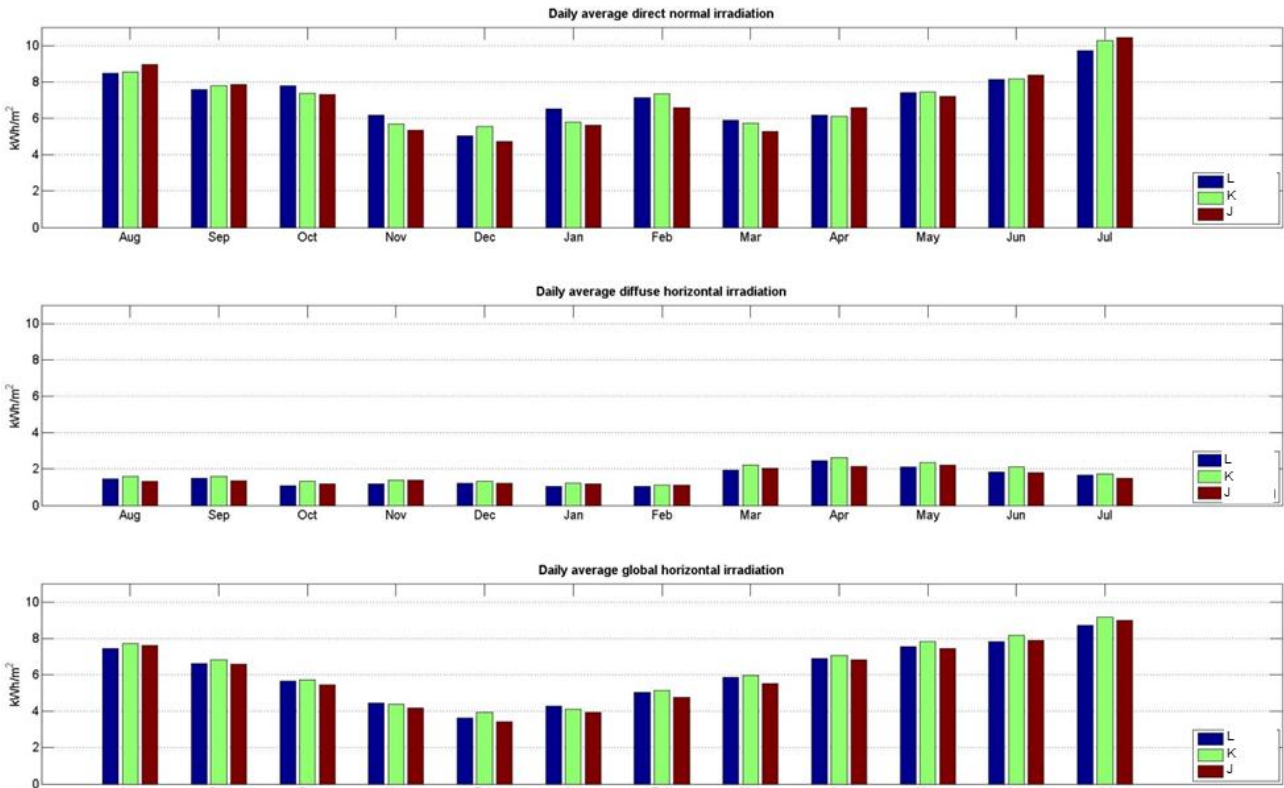
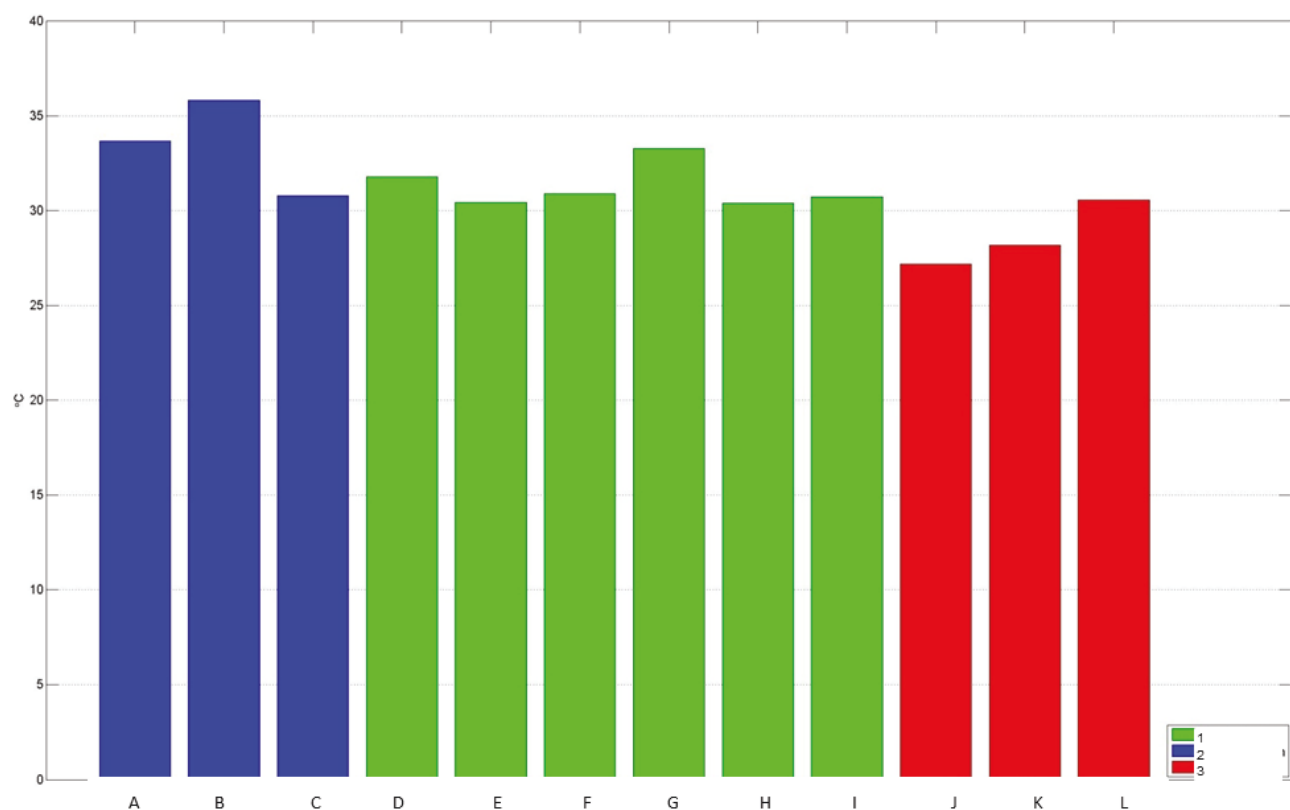


Figure 5-4. Daily average irradiation levels in Region 3 in each month of the study period.

effect is not smoothened out by a fluctuating proportion of diffuse irradiance. The seasonal pattern of atmospheric scattering in Region 1 resembles that in Region 3 but reaches significantly higher levels especially in the summer when the cosine effect reaches its minimum. The comparatively low annual direct irradiation levels of Region 2 are caused by high atmospheric scattering throughout the time between the vernal and autumnal equinoxes. That is why the region has the lowest seasonal variability of daily average global irradiation. In general, the seasonal variability of DNI is lower than that of GHI because DNI is not affected by the cosine effect.

The irradiance data imply that out of the 12 monitoring station sites, the best ones for PV power generation are located in Region 1 due to some of its sites' comparatively high global irradiation levels and in Region 3 due to its low level of atmospheric scattering. In addition to irradiance however, the operating cell temperature of PV modules has a major impact on the efficiency at which the module converts sunlight into electricity. As discussed in section 3.3, the cell temperature is mainly influenced by ambient air temperature, incident irradiance, and wind speed. Therefore, also ambient air temperature and wind speed levels need to be studied in order to find out the suitability of a site for PV installation.

Since PV electricity is not generated at night, only daytime ambient air temperatures matter. Furthermore, midday temperature levels are more important than morning or evening temperatures in the case of typical utility-scale array tilt angles. Therefore, rather than averaging ambient air temperature over the entire time frame or even over daylight hours only, temperature level differences were studied by comparing the GHI-weighted annual average temperatures at the 12 stations. As can be seen from (2013)Figure 5-5, the lowest temperature estimates are found in Region 3 and the highest in Region 2.



(2013)Figure 5-5. GHI-weighted annual average air temperature at each monitoring station considered in the study.

The observations show (Figure 5-6) that the common knowledge of the moderating effect of water bodies on seasonal temperature variability is valid also in the case of GHI-weighted average temperatures. The country's lowest as well as highest temperatures were measured at the inland stations, whereas the three stations on the coast in Region 2 and Region 3 (Site C, Site A, and Site L) experienced the least variation. The GHI-weighted average temperature stayed below 35 °C at all three stations in Region 3 in every month.

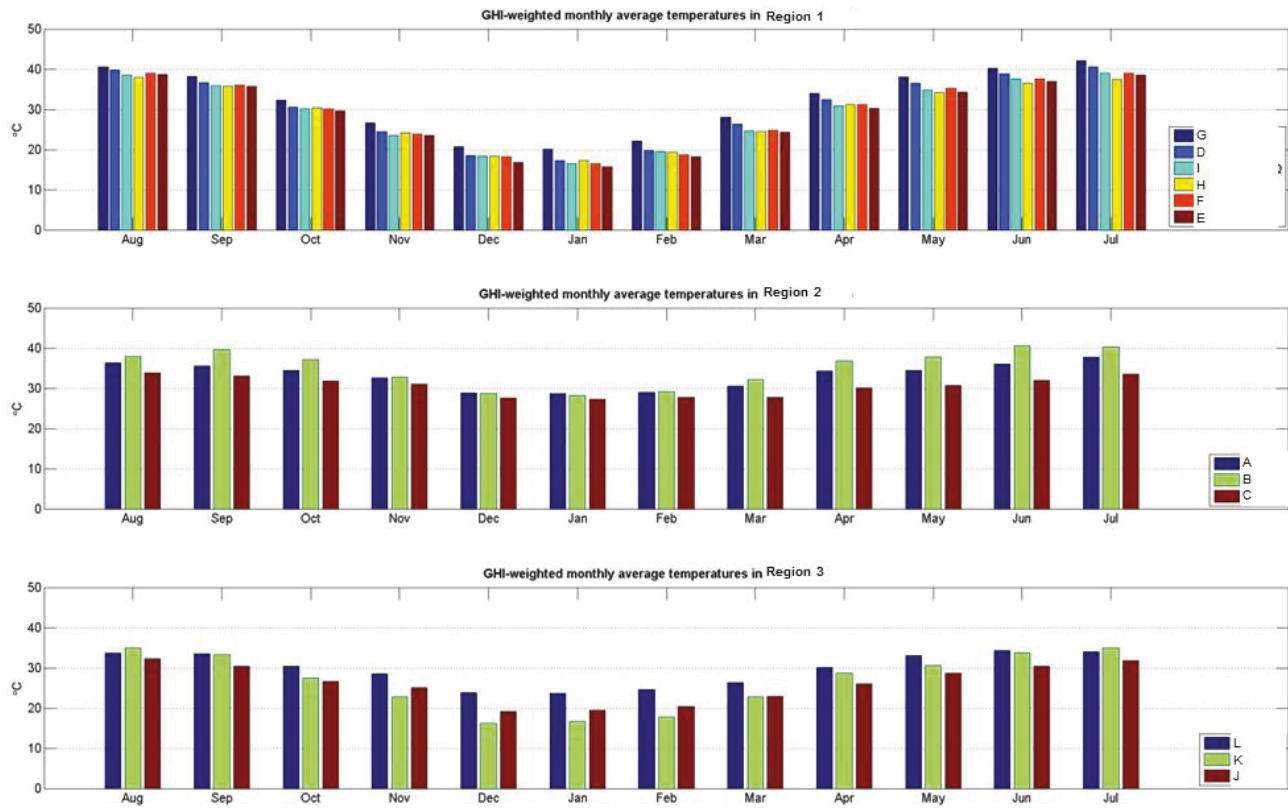


Figure 5-6. GHI-weighted monthly average air temperatures at each monitoring station considered in the study.

Increasing ambient air temperature reduces the conversion efficiency of a solar module through rising cell temperature. By contrast, increasing wind speed lowers the temperature of a solar cell by intensifying the forced convection of heat from the cell. Consequently, the performance of the module is improved. Therefore, windy site locations are generally more suitable for PV deployment than calm locations. The effect of wind speed is, however, much less significant than that of irradiance or ambient air temperature.

As can be seen from Figure 5-7, the wind speed measurements do not correlate well with the data segmentation adopted: all three regions have relatively windy and calm sites. Only the Site J in Region 3 stands out with clearly higher weighted average wind speed levels than the other stations throughout the year. The seasonal variability of wind speed is low at most stations. In summer months however, wind speeds seem to be on average higher than in winter months. This is good from the PV performance point of view as most of the annual irradiation is concentrated between the vernal and autumnal equinoxes.

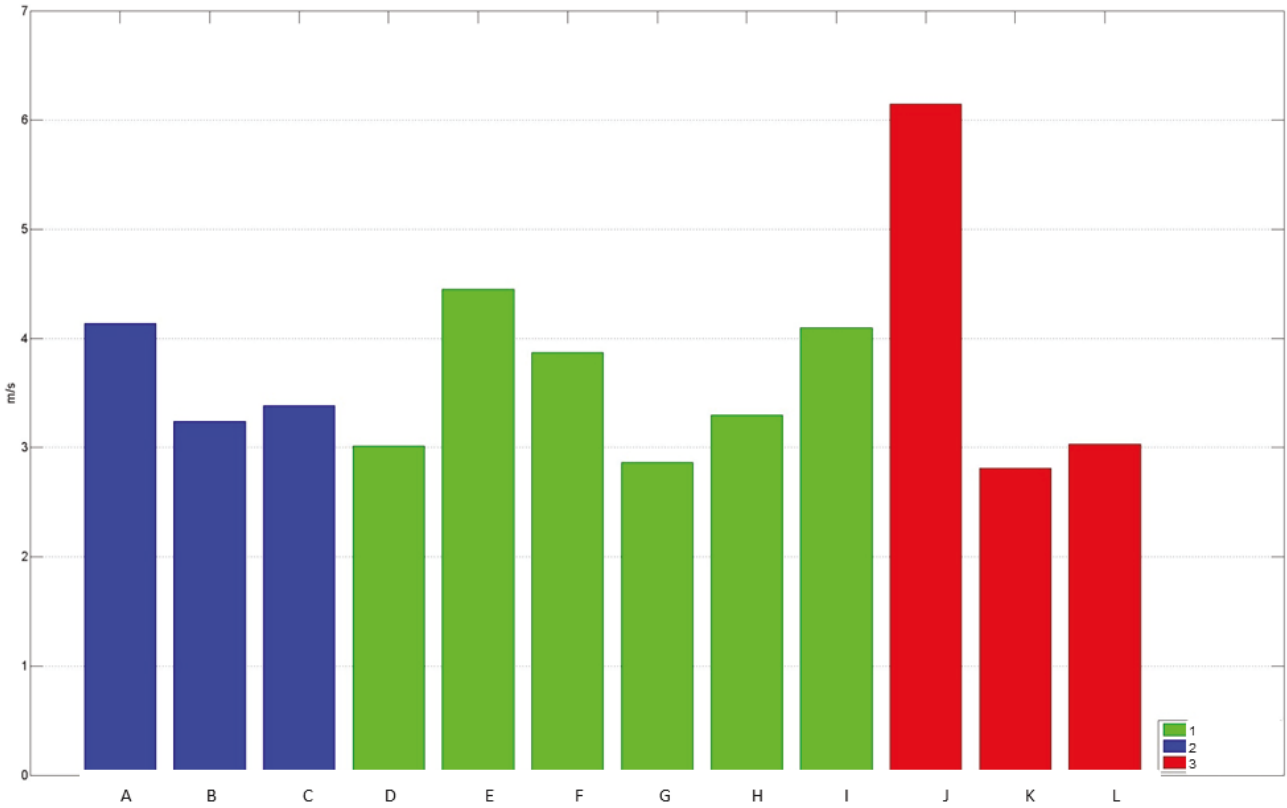


Figure 5-7. GHI-weighted annual average wind speed at 3 m altitude at each monitoring station considered in the study.

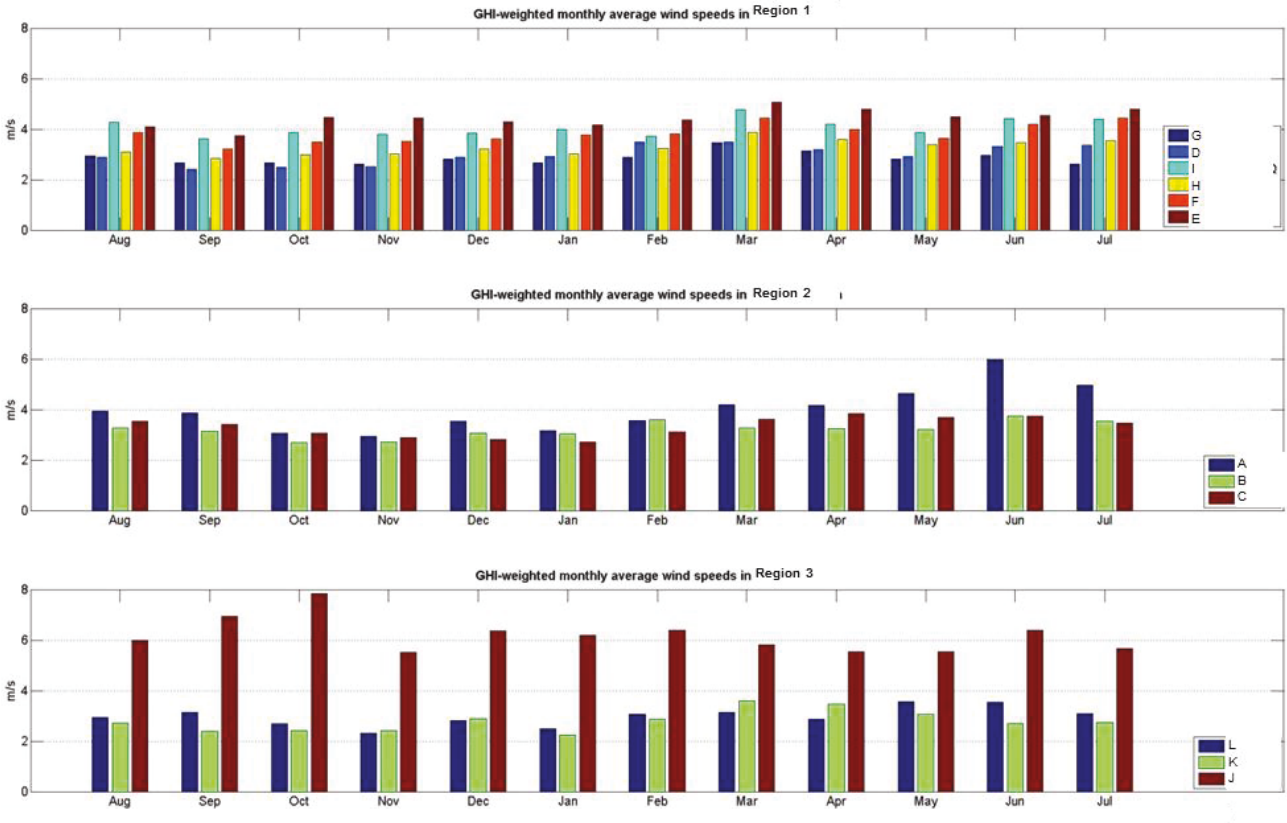


Figure 5-8. GHI-weighted monthly average wind speeds at 3 m altitude at each monitoring station considered in the study.

5.2 Assessment of PV Performance

This subsection presents the outcome of the performance simulation of different PV power plant designs in the Arabian Peninsula. The focus of the section lies on the impact which different design choices have on plant performance. Specifically, the section reports the sensitivity of the simulated plant performance to PV material, mounting method, plant capacity, and loading ratio. Section 4.1 first gives the basis for the subsequent technology comparison-oriented sections by describing the extent and variability of effective irradiance simulated for the 12 monitoring station sites.

5.2.1 Effective Irradiance

Resulting from the assumptions made in the optical model, the simulation of W_{eff} is not dependent on the selected PV material but solely on the mounting method, which determines ϑ on POA. Tracking mechanisms are used to minimise ϑ by constantly turning POA towards the Sun and, thereby, increase the proportion of incident direct irradiance and maximise the incident global irradiance on POA. Single axis trackers can significantly reduce ϑ compared to fixed mount and with dual axis trackers, ϑ can be kept, in theory, at zero degrees throughout the day. In reality however, the tracking benefits are limited by array self-shading as well as imperfect tracking precision. In order to avoid self-shading, backtracking is normally used in the morning and evening hours. Because of the objective of maximising the proportion of incident direct irradiance, the deployment of tracking technologies is favoured by site locations with low levels of atmospheric scattering. This can also be seen in Figure 5-9, which presents the simulated annual effective irradiation at each of the 12 monitoring stations. In the case of fixed mount, the spatial variability of annual effective irradiation is low ranging from around 2200 kWh/m² at the stations in Region 2 to 2400 kWh/m² at some of the stations in Region 1 and Region 3. GHI, whose spatial variability is relatively low, is the key determinant of effective irradiance with fixed mount. When tracking is used however, the significance of DNI is emphasised and consequently, the variation in simulated effective irradiation between stations is increased. Due to its high DNI levels, Region 3 possesses the most abundant resources for PV stations with tracking systems. While at Site A, effective irradiation increases by 28% when shifting from fixed mount to dual axis tracking, the respective change at Site L leads to a boost of 37%. In the case of single axis tracking, the corresponding figures are 18% and 23%, respectively.

The seasonal variability of the simulated effective irradiation can be observed in Figure 5-10 for Region 1, in Figure 5-11 for Region 2, and in Figure 5-12 for Region 3. When compared to GHI (Figure 5-2, Figure 5-3, and Figure 5-4), the seasonal variability of effective irradiance is significantly lower due to its higher proportion of DNI. Nevertheless, the seasonal patterns of effective irradiance are similar to those of GHI; the variability is the highest in Region 1 and Region 3 and the lowest in Region 2. The vernal peaks in DNI can be observed more clearly in the seasonal pattern of effective irradiance than in that of GHI. When shifting from fixed mount to tracking, the impact of atmospheric scattering is reduced thus making the variation more closely follow the seasonal cycle of the Sun's position. As a result, a tracking system tends to increase and regularize the seasonal variability of effective irradiance.

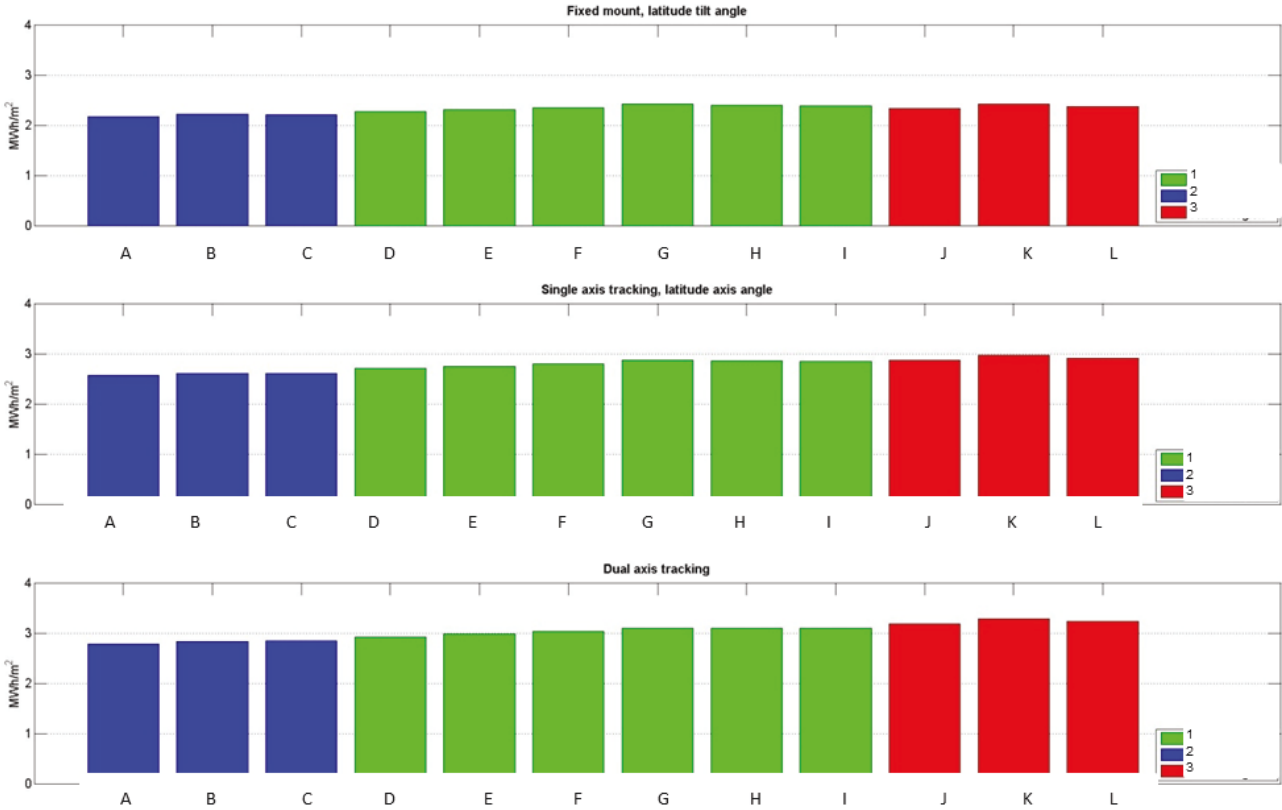


Figure 5-9. Annual effective irradiation at each monitoring station considered in the study.

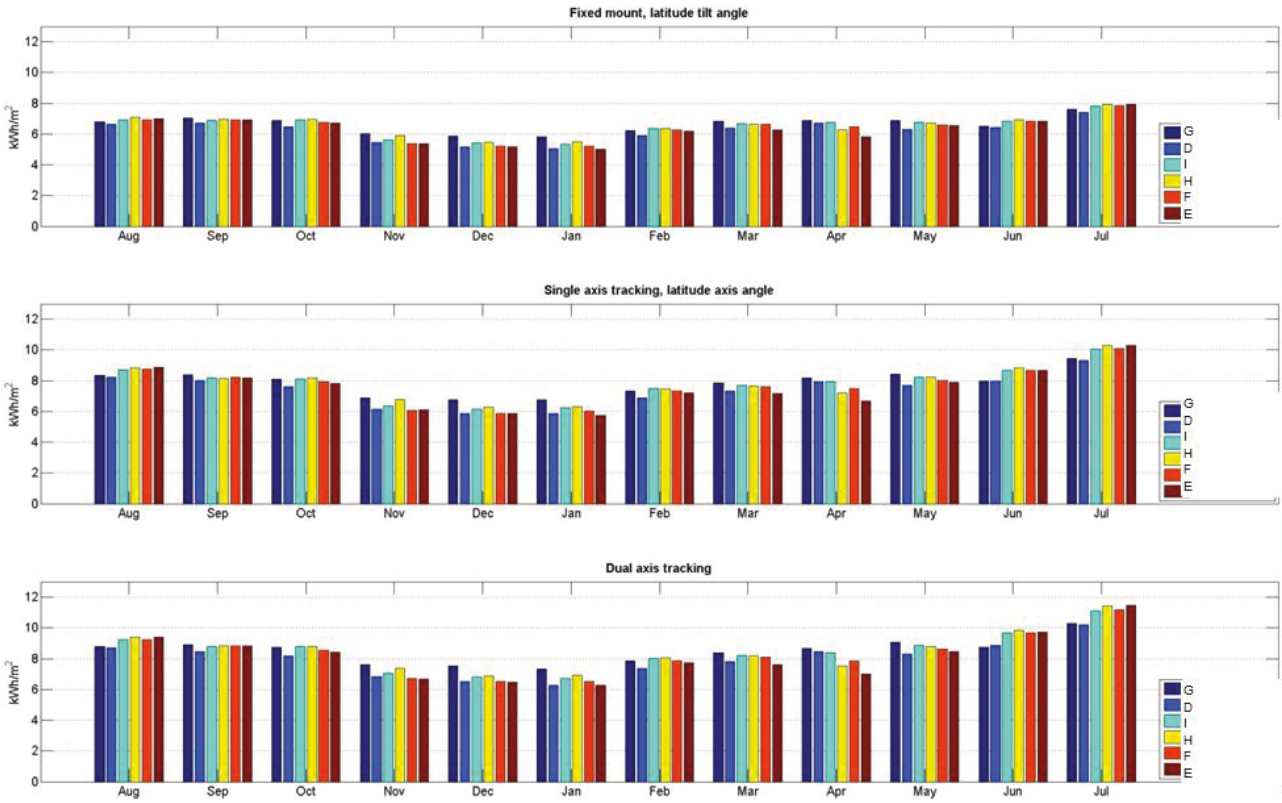


Figure 5-10. Daily average effective irradiation levels in Region 1 in each month of the study period.

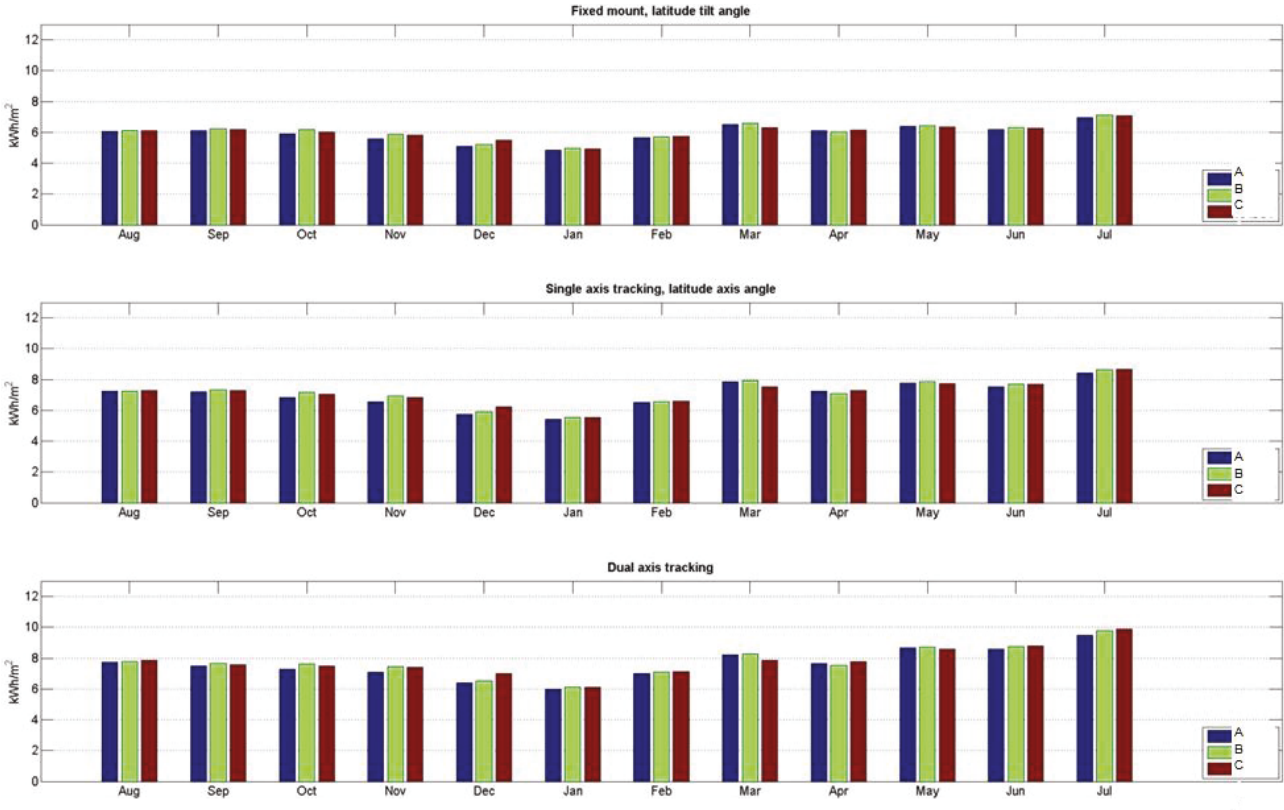


Figure 5-11. Daily average effective irradiation levels in Region 2 in each month of the study period.

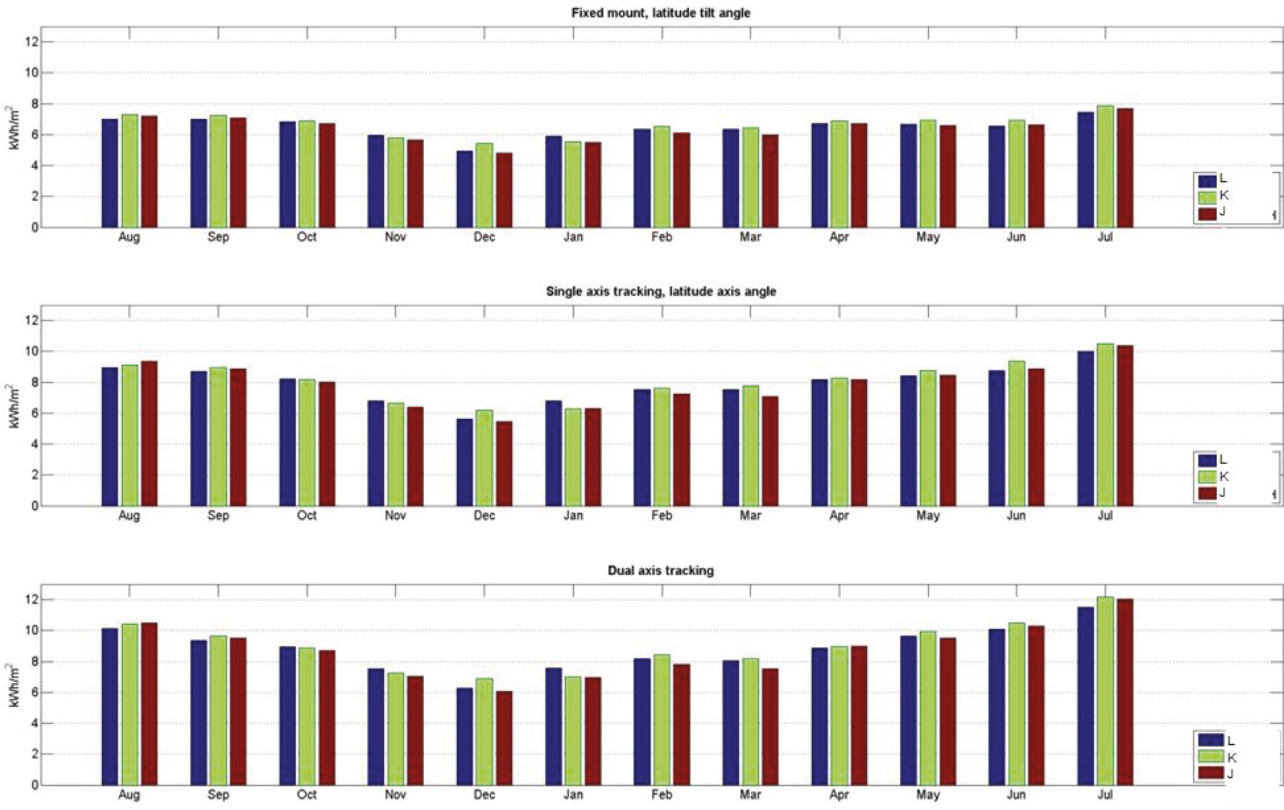


Figure 5-12. Daily average effective irradiation levels in Region 3 in each month of the study period.

5.2.2 Effect of PV Material

The focus of this section is on the comparison of performance levels obtained by using different solar module types in the simulation. The modules under consideration are compared in two separate subsections based on the classification explained in section 3.4.1: the module types with the electrical model coefficients based on TPFT (TPFT group) and the types with the coefficients based on data provided by manufacturers (MD group). Since the thermal model incorporated in the simulator involves technology-dependent parameters, also the simulated cell temperature levels are discussed in this section. This section only deals with power stations equipped with fixed mount. The effect of tracking is discussed in section 5.2.3. In this section, the best-performing module type from each PV material group is selected for the further analysis of the subsequent sections.

Module Types with Third-Party Field Test-Based Electrical Model Coefficients

The module types of the TPFT group comprise 13 wafer-based and two thin-film modules. The generalizability of the results of this assessment is, therefore, hindered by the limited scale and scope of the thin-film module sample. Moreover, the single a-Si module, Kaneka TSC120, is significantly older than the rest of the considered modules. The electrical model coefficients being based on the measurements of well-known testing laboratories however, the credibility of the results can be considered good.

Apart from effective irradiance, cell temperature is the most important factor influencing PV performance. It varies with changing meteorological parameters and conversion efficiency. Figure 5-13 presents the simulated effective irradiance-weighted annual average cell temperatures for each module type and all sites considered. In general, the wafer-based solar modules should operate at a lower cell temperature than thin-film modules because of their higher conversion efficiencies (see Table 4-1 in section 4.2). This can also be observed in Figure 5-13. The simulated weighted average cell temperature levels of the CdTe module, First Solar FS-272, are on average 13% higher than those of the heterojunction with intrinsic thin layer (HIT) module, Sanyo HIP-200BA19. First Solar FS-272 and Sanyo HIP-200BA19 are the two extremes of this sample when it comes to their thermal behaviours. The temperature levels of the other thin-film module considered, Kaneka TSC120, do not seem consistent, however. The a-Si thin-film module shows thermal behaviour similar to the mc-Si modules although its STC conversion efficiency is less than half of the average efficiency of the mc-Si modules and the temperature coefficient of maximum power only slightly lower than that of First Solar FS-272 (see Table 4-1). This inconsistency might be caused by the temperature-dependent stabilisation level of light-induced efficiency degradation (Staebler-Wronski effect). The stabilisation level increases with rising cell temperature and, thus, partially compensates the temperature-induced voltage drop caused by intensified recombination. As a result, the conversion efficiency of a-Si modules should decrease at a declining rate with rising cell temperature. However, further local validation work on the topic is required to expand the geographical and technological scopes of Tuomiranta et al. (2013) and, thereby, determine whether there is more generalized basis for these findings.

The spatial variability of the cell temperature levels is lower than that of GHI-weighted average ambient air temperature ((2013)Figure 5-5) because of the low correlation between the monthly average levels of effective irradiance, ambient air temperature, and wind speed. However, the pattern is alike. The lowest cell temperature levels are simulated for the cool and windy, northern site, Site J, whereas the highest levels are obtained for the southern inland stations Site B and Site G, which also experienced the highest average ambient air temperatures. The variability within the regions is relatively high due to the microclimate-scale effects on ambient air temperature and wind speed.

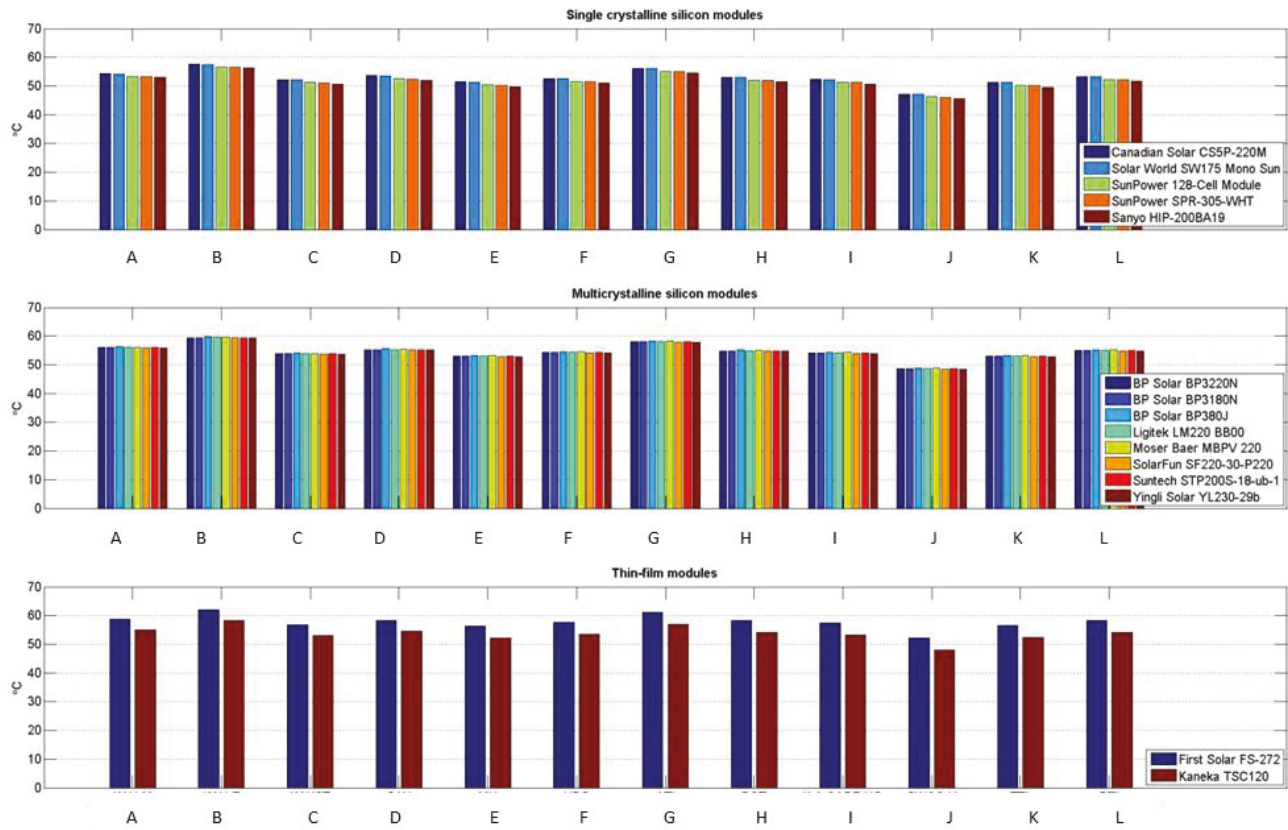


Figure 5-13. Simulated effective irradiance-weighted annual average cell temperatures for the module types of the TPFT group. (Other design-specific user inputs: fixed mount, latitude tilt, 20 MWp, 100% loading ratio; valid in Figures 4-13 – 4-15).

Figure 5-14 presents the simulated plant *CF* of each location for all 15 sample modules. The sites located in Region 3 and Region 1's sites with high global irradiation levels are the most favourable locations for PV deployment while the sites in Region 2 are the least suitable. This is the case of all 15 module types. As can be clearly seen from Figure 5-15 presenting the simulated *PR*, site suitability seems to be primarily determined by effective irradiance (Figure 5-9). The impact of effective irradiance is isolated (Eq. 4.11) and consequently, spatial variability becomes minimal. The most notable exception to this generalisation is Site J, which is the second most favourable location for the wafer-based modules in spite of its comparatively low annual effective irradiation. This is due to the exceptionally low cell temperature levels simulated for the site and the consequently high *PR*. The opposite is true for Site G. It is exposed to the highest global irradiation among all 12 stations. Due to the high cell temperatures however, the performance of the wafer-based modules is simulated to be slightly better at other Region 1's sites with high global irradiation levels as well as at Site K and Site J. The performance of thin-film modules is less temperature-dependent than that of wafer-based modules (see Table 4-1) and, therefore, has a higher correlation with effective irradiance levels i.e. a lower variability of irradiance-normalised performance.

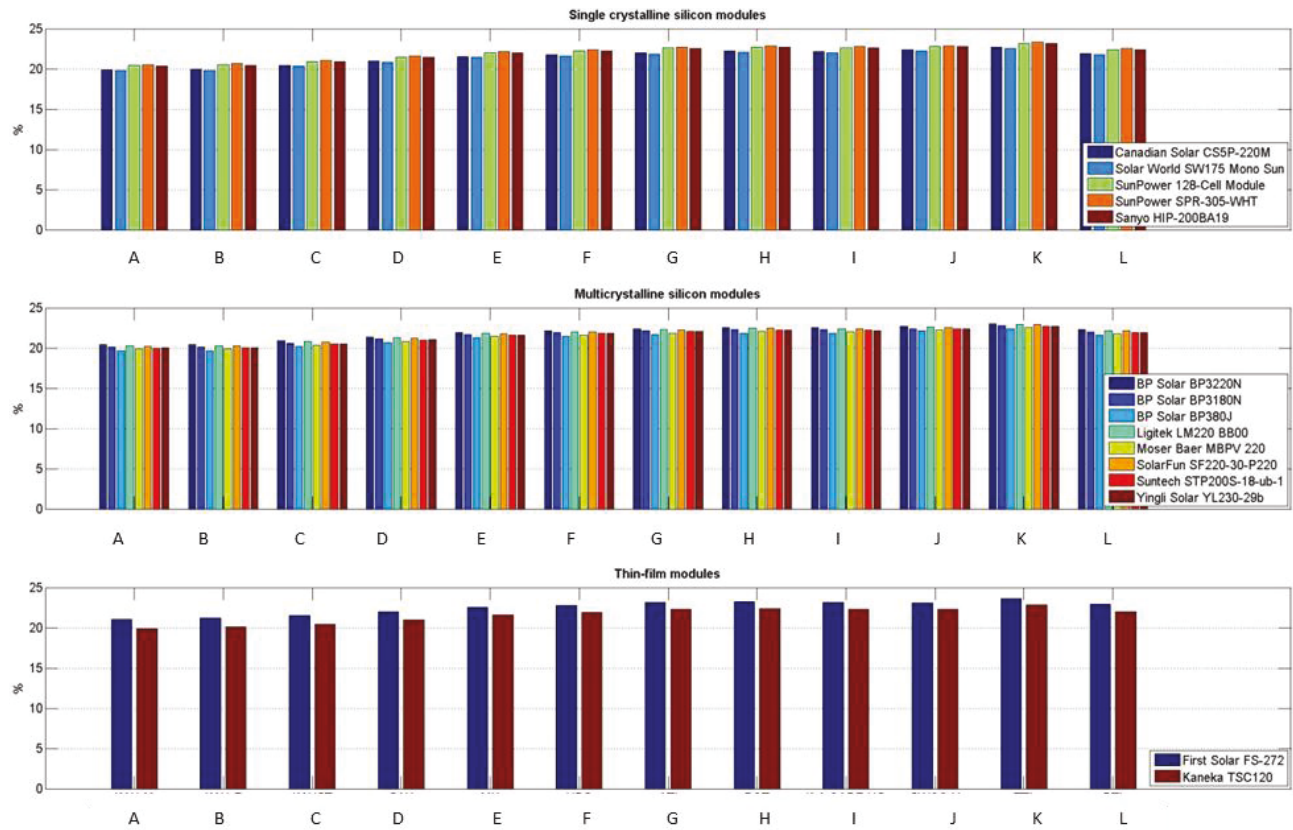


Figure 5-14. Simulated capacity factors for the module types of the TPFT group.

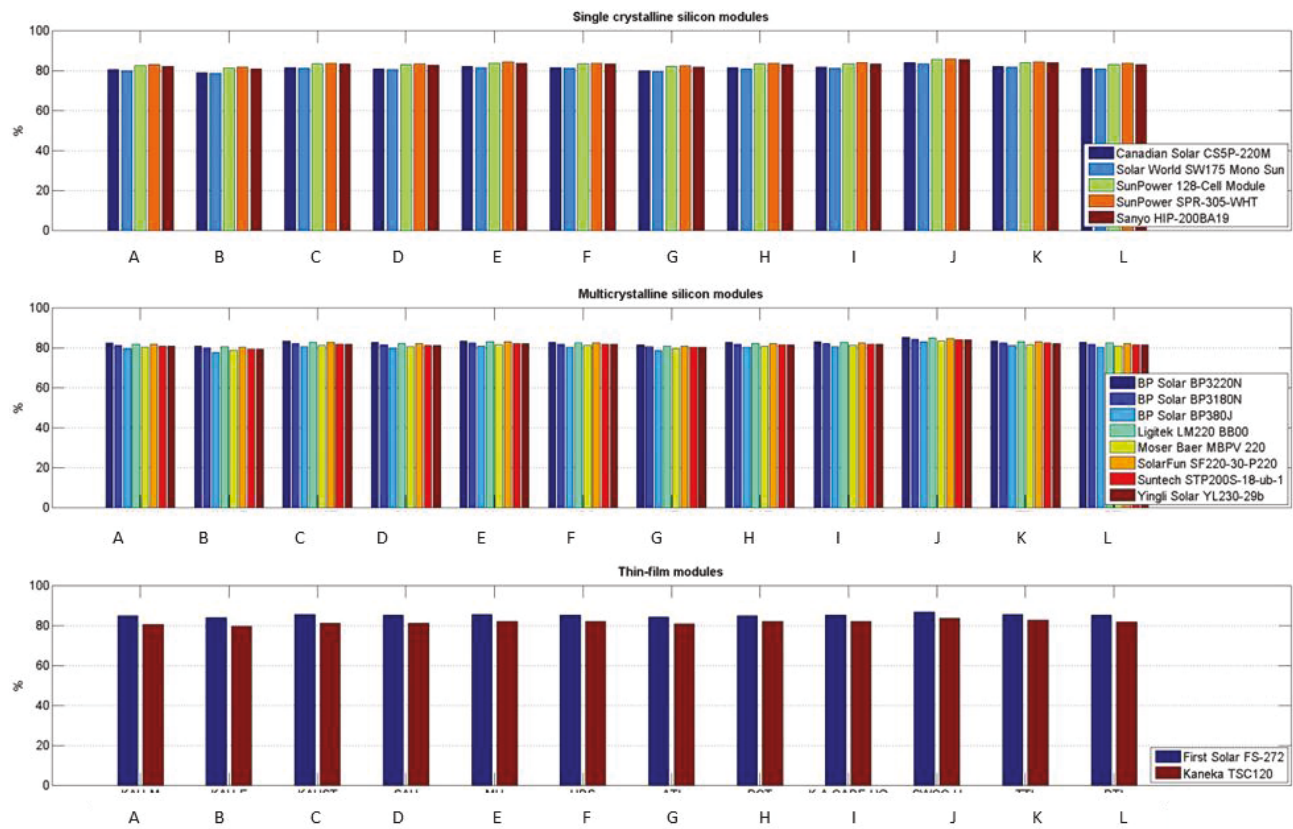


Figure 5-15. Simulated performance ratios for the module types of the TPFT group.

As can be seen from the above figures, the highest performance indicators were obtained for the CdTe module, First Solar FS-272, reaching its maximum CF of 23.6% (2070 FLH) at Site K. This module type turned out to show the best performance in all site locations followed by SunPower's modules made of c-Si wafer-based back-contact solar cells and Sanyo's HIT module. The best performing mc-Si module is BP Solar's BP3220N with a maximum CF of 23.0% (2020 FLH). The highest CF simulated for the a-Si module type is 22.8% (2000 FLH). At the worst site, Site A, CF ranges from 19.7% (1720 FLH, BP Solar BP380J) to 21.0% (1840 FLH, First Solar FS-272).

Module Types with Manufacturer Data-Based Electrical Model Coefficients

Table 4-2 in section 4.2 shows that the module types of the manufacturer data-based (MD) group comprise 19 wafer-based and 11 thin-film modules. The oldest models of the sample are the two a-Si modules released in 2009. Half of the modules have been released in 2013 or 2014 covering all the materials apart from a-Si and HIT. The scale and scope of the sample can be considered sufficient for a credible comparison. However, as the simulation of the modules' electrical performance is based on data provided by manufacturers, the absolute performance levels of single module types are not as credible as in the case of the TPFT group.

Figure 5-16 presents the simulated effective irradiance-weighted annual average cell temperatures for the considered module types. As in the case of the TPFT sample, the lowest cell temperatures were obtained for high-efficiency wafer-based modules and the highest for CdTe and copper indium diselenide (CIS) modules. The average difference between the two extreme cases, Calyxo's CdTe module and Panasonic's HIT module, is 13% as in the case of the TPFT group.

As in the assessment of the TPFT module types, the sites located in Region 3 and Region 1's sites with high global irradiation levels offer the most and the sites in Region 2 the least favourable locations for all technologies (Figure 5-17). Also, the spatial variability of PR levels (Figure 5-18) shows the exactly same pattern as in the case above: the best irradiance-normalised performance is obtained for Site J and the worst for Site B and Site G. Performance levels significantly vary between the different CIS module types (Table 4-2). This is due to the highly variable temperature coefficient of maximum power inside the CIS group caused by the varying concentrations of gallium in the modules. Therefore, in addition to the wafer-based modules, the CIS modules with a low gallium concentration show high sensitivity to changes in cell temperature. The fact that the spatial variabilities of the performance indicators are so similar between the two samples implies that firstly, the discrepancy between the ranges of the samples' temperature coefficients is not sufficiently high for the effect of cell temperature to outrun that of effective irradiance in new locations. Secondly, irradiation variability within the area of interest is not sufficiently high to bring forth the wider low light efficiency behaviour spectrum of this sample.

The highest performance indicators for all site locations are obtained by NexPower's a-Si and micromorphous silicon (a-Si/ μ c-Si) thin-film modules – CF of 25.0% (2190 FLH) and 24.3% (2130 FLH), respectively, at Site K. NexPower's modules were followed by Panasonic's HIT, SunPower's back-contact c-Si, Sharp's a-Si, and Solar Frontier's CIS modules. First Solar's CdTe module has a maximum CF of 23.7% (2080 FLH) and the best performing mc-Si module, REC's 260PE, 23.2% (2030 FLH). At the worst site, Site A, CF ranges from 19.8% (1730 FLH, Solibro SL2-125) to 22.3% (1950 FLH, NexPower NH100AT 5A). Apart from Panasonic's and SunPower's high-efficiency wafer-based modules, all best-performing module types ($CF > 21\%$ at all sites) are made of thin-film materials. The CIS and mc-Si modules with high temperature coefficients of maximum power (Kyocera, SolarWorld, Solibro, Avancis) showed the worst performance at

CHAPTER 5. PV PERFORMANCE IN THE ARABIAN PENINSULA



Figure 5-16: Simulated effective irradiance-weighted annual average cell temperatures for the module types of the MD group. (Other design-specific user inputs: fixed mount, latitude tilt, 20 MWp, 100% loading ratio).

CHAPTER 5. PV PERFORMANCE IN THE ARABIAN PENINSULA



Figure 5-17: Simulated capacity factors for the module types of the MD group. (Other design-specific user inputs: fixed mount, latitude tilt, 20 MWp, 100% loading ratio).

CHAPTER 5. PV PERFORMANCE IN THE ARABIAN PENINSULA



Figure 5-18: Simulated performance ratios for the module types of the MD group. (Other design-specific user inputs: fixed mount, latitude tilt, 20 MWp, 100% loading ratio).

all sites. Interestingly, CIS modules form the only group where there are both best-performing and worst-performing modules due to their highly variable temperature coefficients. Although the manufacturers do not always give information about whether they use gallium in the fabrication of their modules, it is somewhat obvious that the CIS modules with lower temperature coefficients and, therefore, higher band gaps have higher gallium concentrations.

5.2.3 Effect of Mounting Method

This section deals with the impact of the mounting method on the performance of power stations equipped with the best-performing module types of each PV material group discussed in section 5.2.2. The first subsection delves into the effect of the POA inclination angle on the performance of fixed mount systems. The second subsection presents the outcome of an analogous analysis of single and dual axis tracking systems equipped with the highest-efficiency module types ($\eta_{mpp,0} > 20\%$, see Table 5-1). Moreover, the performances of the tracking systems are compared to those of the respective fixed mount systems.

Fixed Mount

This section reports the results of the optimisation of fixed mount tilt angles for the 12 station sites. The technological scope of the analysis comprises the best performers of each PV material group analysed in section 5.2.2. The 13 selected module types are presented in Table 5-1, which is a combined extract from Table 4-1 and Table 4-2.

Table 5-1: Module types considered in sections 5.2.3, 5.4, and 5.5.

Name	Material	Country of origin	Release year	Database	Source	$\eta_{mpp,0}$	Temperature coefficient of $P_{mpp,0}$
SunPower SPR-305-WHT	c-Si	USA	2009	SAM	SNL	21.3 %	-0.40 %/°C
Sanyo HIP-200BA19	HIT	Japan	2009	SAM	SNL	21.3 %	-0.46 %/°C
BP Solar BP3220N	mc-Si	USA	2010	SAM	SNL	14.8 %	-0.44 %/°C
First Solar FS-272	CdTe	USA	2009	SAM	SNL	9.9 %	-0.33 %/°C
Kaneka TSC120	a-Si	Japan	2006	PVsyst	Photon Magazine	7.0 %	-0.31 %/°C
SunPower SPR-455J-WHTD	c-Si	USA	2012	PVsyst	Manufacturer	22.7 %	-0.33 %/°C
Panasonic VBHN240SE10	HIT	Japan	2012	PVsyst	Manufacturer	22.0 %	-0.29 %/°C
REC 260PE	mc-Si	Norway	2012	PVsyst	Manufacturer	17.8 %	-0.40 %/°C
ReneSola JC310M 24Ab	mc-Si	China	2012	PVsyst	Manufacturer	17.7 %	-0.40 %/°C
NexPower NH100AT 5A	a-Si	Taiwan	2009	PVsyst	Manufacturer	7.3 %	-0.20 %/°C
Sharp NA-E140L5	a-Si/ μ c-Si	Japan	2013	PVsyst	Manufacturer	10.8 %	-0.30 %/°C
FirstSolar FS3100 Plus	CdTe	USA	2014	PVsyst	Manufacturer	15.3 %	-0.31 %/°C
SolarFrontier SF170 S	CIS	Japan	2013	PVsyst	Manufacturer	15.2 %	-0.32 %/°C

Figure 5-19 and Figure 5-20 show the change in the simulated capacity factors of power stations equipped with the selected modules of the TPFT group when the POA inclination angle is varied from horizontal to vertical (with the orientation normal to the equator). The results of the same simulation for power stations equipped with the selected modules of the MD group are presented in Figure 5-21 and Figure 5-22. The difference in performance between optimally and vertically tilted arrays ranges from a reduction of 34% (BP Solar BP3220N at Site K) to 45% (Kaneka TSC120 at Site A). As can be expected based on the Arabian Peninsula's location in the low latitudes, the respective variation between optimal and horizontal tilt angles is much less ranging from a reduction of 5.6% (BP Solar BP3220N at Site A) to 11.8% (Kaneka TSC120 at Site J). Accordingly, horizontal alignment reduces performance less in southern sites and vertical alignment in northern sites. The module types with low temperature coefficients of maximum power tend to have the highest tilt angle-dependent performance variability as the effect of effective irradiance outruns the effect of cell temperature in their case.

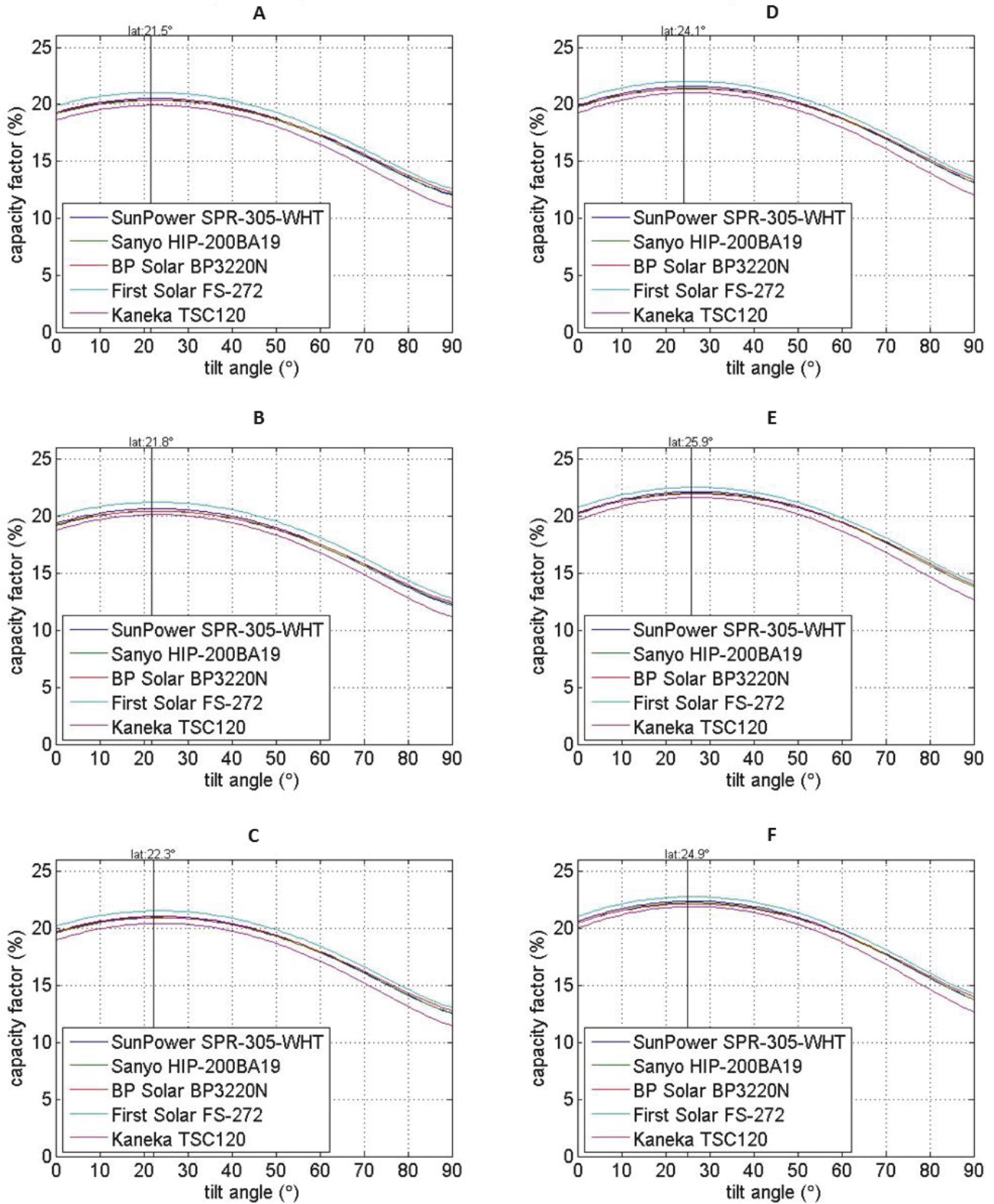


Figure 5-19: POA-tilt angle-dependent variation in the simulated capacity factors of fixed mount systems equipped with the best-performing module types of the TPFT group in the six lowest-DNI site locations. (Other design-specific user inputs: 20 MWp, 100% loading ratio).

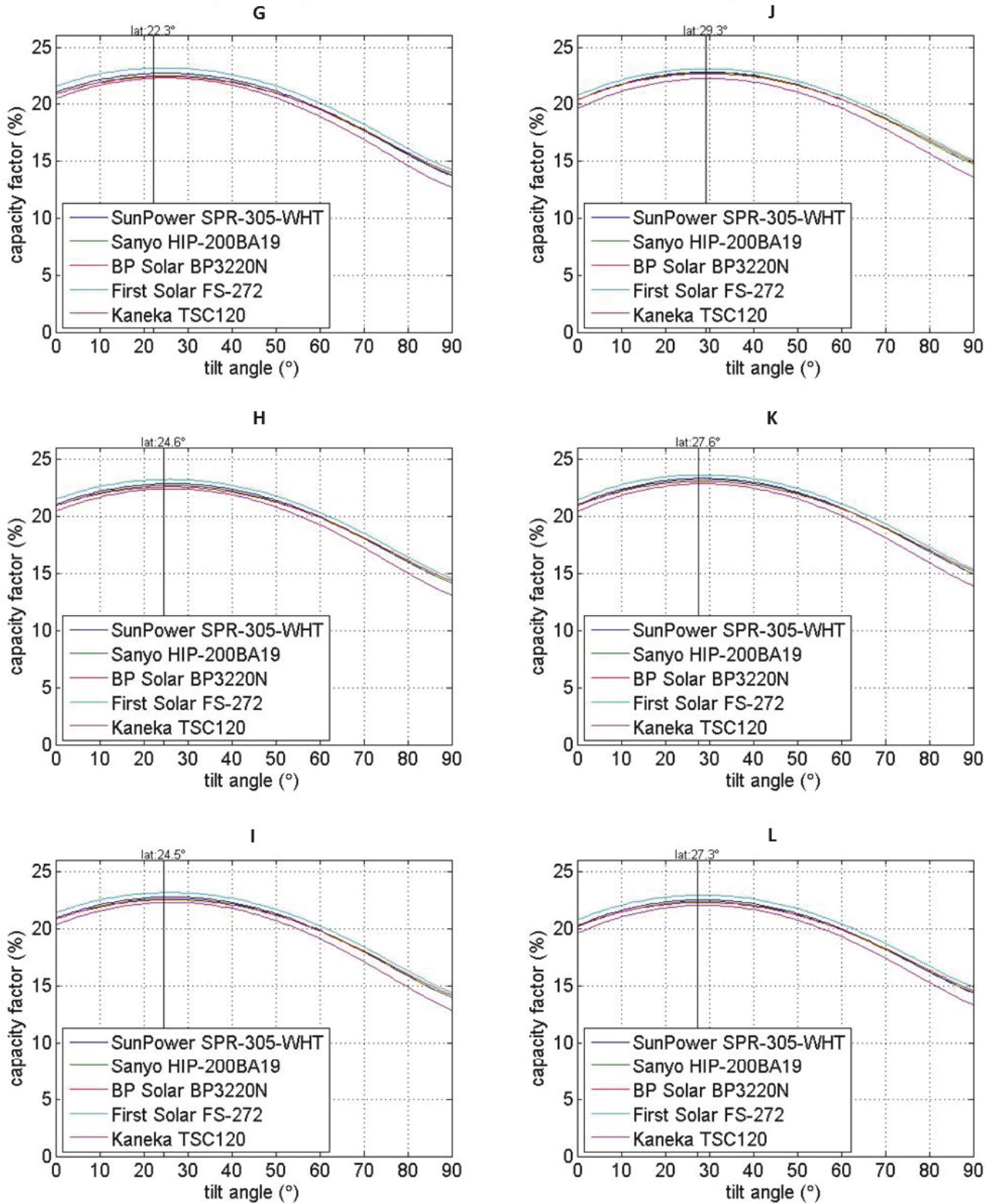


Figure 5-20: POA tilt angle-dependent variation in the simulated capacity factors of fixed mount systems equipped with the best-performing module types of the TPFT group in the six highest-DNI site locations. (Other design-specific user inputs: 20 MWp, 100% loading ratio).

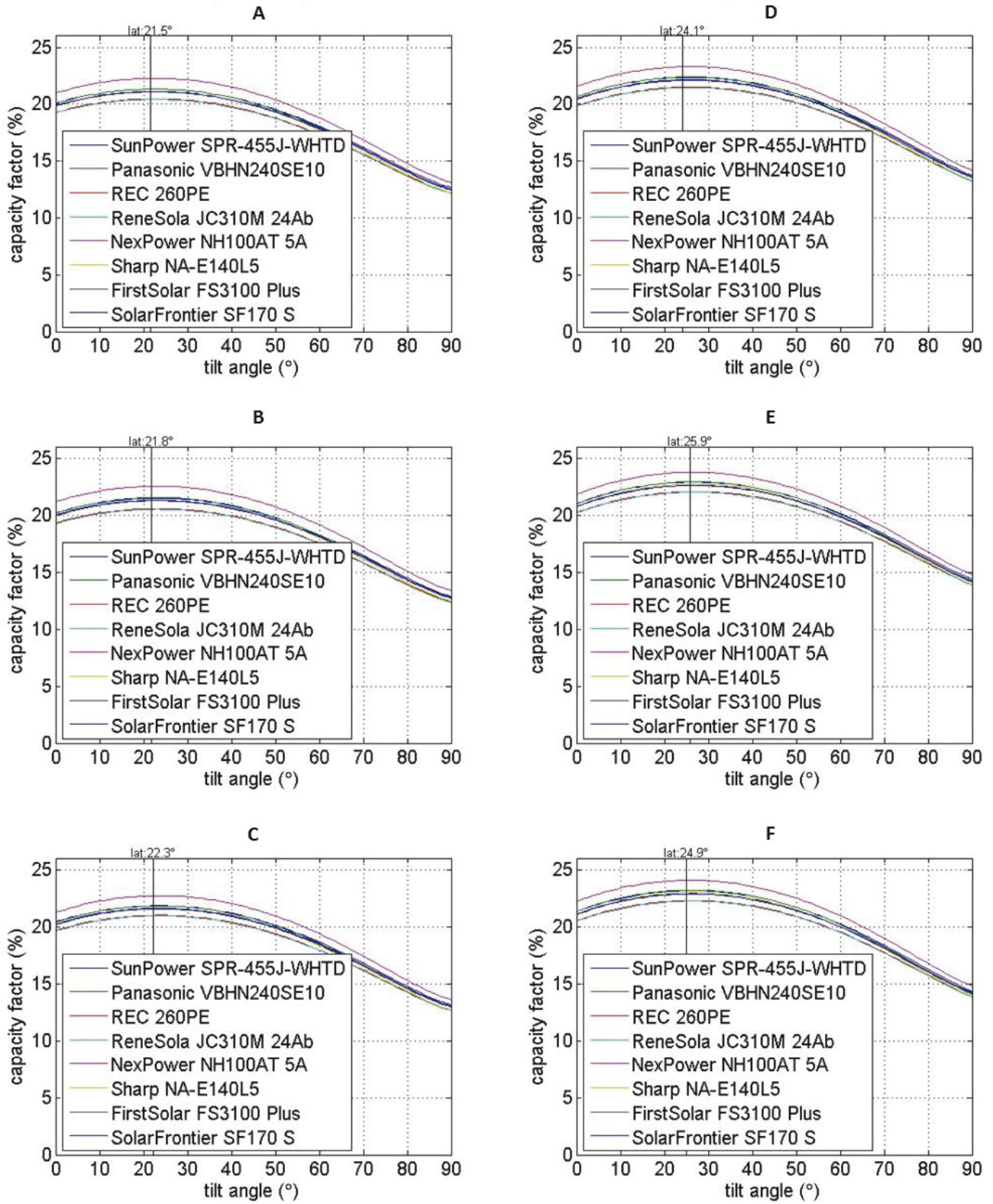


Figure 5-21: POA tilt angle-dependent variation in the simulated capacity factors of fixed mount systems equipped with the best-performing module types of the MD group in the six lowest-DNI site locations. (Other design-specific user inputs: 20 MWp, 100% loading ratio).

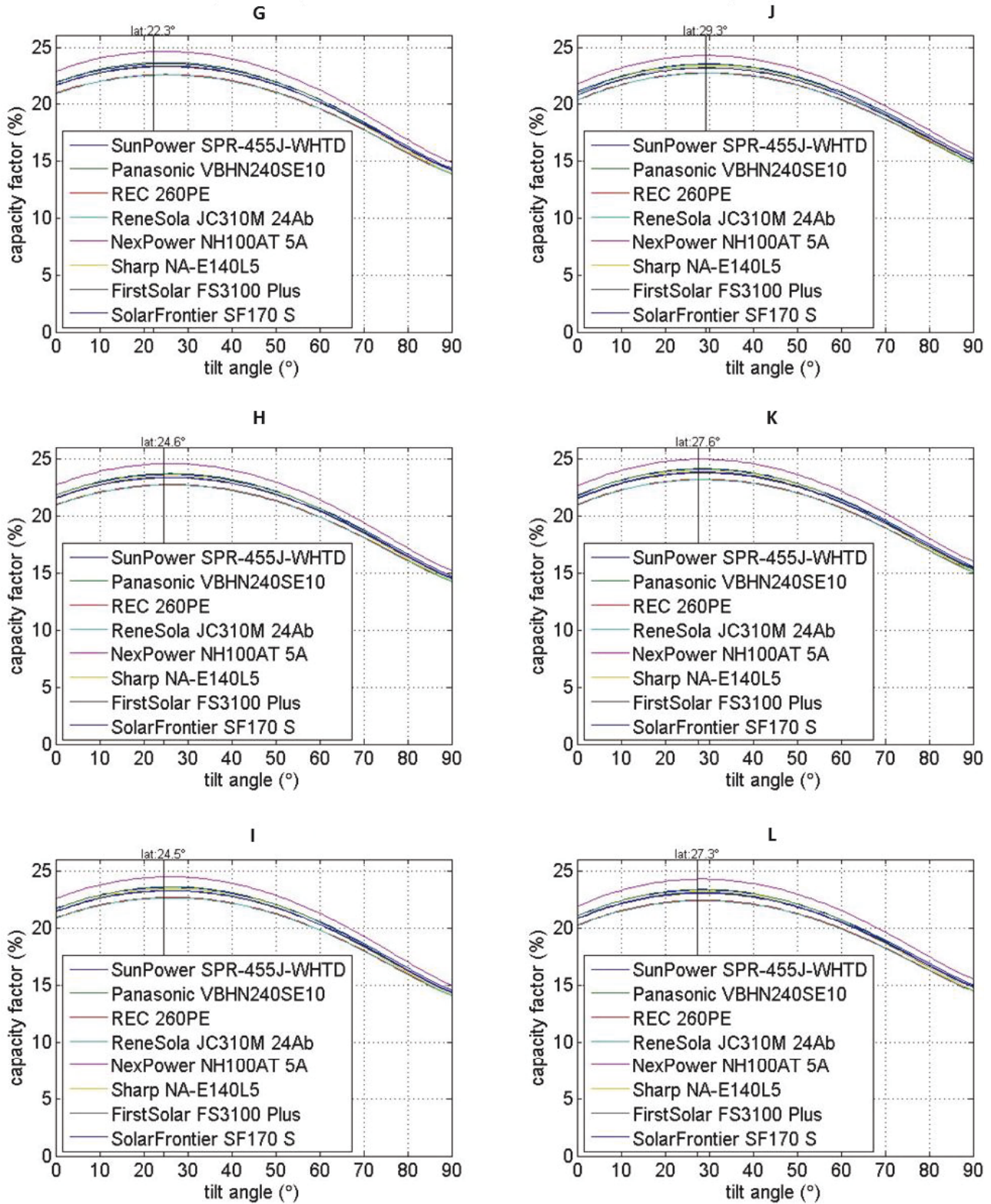


Figure 5-22: POA tilt angle-dependent variation in the simulated capacity factors of fixed mount systems equipped with the best-performing module types of the MD group in the six highest-DNI site locations. (Other design-specific user inputs: 20 MWp, 100% loading ratio).

In the low latitudes ($< 30^\circ$), the POA inclination angle is commonly set at the latitude of the plant's site location. Through this practice, ϑ can be minimised on the equinoxes making it roughly reach zero at the solar noon. The practice is based on an assumption that the two periods between the equinoxes are equally good when it comes to the overall conditions for PV power generation. As can be seen from the above figures, the optimum tilt angles are higher or approximately the same as the site latitudes for all module types and site locations. The fact that the optimum tilt angles are never lower than the respective site latitudes implies that the months between the vernal and autumnal equinoxes have overall conditions either similar to or worse than the conditions in the months of the opposite period. In other words, the period from April to September does not appear to offer significantly better conditions for PV power generation than the period from October to March in the case of any module type or site location. Therefore, the results indicate that the negative effect of higher cell temperatures in the summer period is not outplayed by the positive effect of higher effective irradiance at any of the 12 sites.

Table 5-2 lists the approximate differences between the simulated module type-specific optimal tilt angles for the 12 station sites and the latitudes of each site. The largest discrepancies, around 2° - 3° , can be found for Site G and Site D. This is due to the sites' high ambient air temperatures (Figure 5-6) relative to the effective irradiance levels (Figure 5-2) during the summer period. The sites of the stations Site E, Site J, and Site K have the highest variation of the optimum tilt angles between technologies. There are two major reasons for this sort of local variability among module types. The first one is related to the wide range of close-to-optimum tilt angles at which abruptly changing array configurations lead to multiple peaks. Thus, in such cases, the variability of the optimum tilt angle is not really caused by seasonal differences in performance patterns but the wide close-to-optimum range of tilt angles sensitive to minor differences in array configurations. This is the case with Site E and Site J, for instance. The other reason is related to a combined effect of the site-specific meteorological characteristics and the differences in the module types' thermal and low-light behaviours. The vernal peak of DNI, which seems to characterise all the 12 station sites (see Figure 5-2, Figure 5-3, and Figure 5-4), plays an important role here. Due to the comparatively low cell temperatures at the time of the peak (see Figure 5-13 and Figure 5-16), the annual maximum of plant performance tends to coincide with the peak. Therefore, in the cases where the close-to-optimum region of tilt angles is narrow, the optimum tilt is primarily determined by the level and duration of the peak (relative to those of July's broader peak) and the thermal behaviour of the module type in question. At Site K for instance, the low temperature coefficient of NexPower's a-Si module makes it possible for the module to perform reasonably well also in the summer months characterised by high effective irradiance as well as high cell temperatures. With the other module types however, the peak in February is more productive and therefore, their optimum tilt angles are higher.

Table 5-2: The differences between the simulated module type-specific optimal tilt angles for the 12 station sites and the latitudes of each site.

	Material	A	B	C	D	E	F	G	H	I	J	K	L
Latitude		21.5	21.8	22.3	24.1	25.9	24.9	22.3	24.6	24.5	29.3	27.6	27.3
SunPower SPR-305-WHT	c-Si	+2°	+1°	+2°	+2°	+2°	+1°	+3°	+1°	+1°	+1°	+1°	+2°
Sanyo HIP-200BA19	HIT	+2°	+1°	+2°	+2°	+0°	+1°	+3°	+2°	+1°	+1°	+1°	+2°
BP Solar BP3220N	mc-Si	+1°	+1°	+1°	+2°	+1°	+1°	+3°	+1°	+1°	+0°	+1°	+2°
First Solar FS-272	CdTe	+2°	+1°	+1°	+2°	+1°	+1°	+3°	+1°	+1°	+0°	+1°	+1°
Kaneka TSC120	a-Si	+1°	+1°	+1°	+2°	+1°	+1°	+3°	+1°	+1°	+1°	+1°	+2°
SunPower SPR-455J-WHTD	c-Si	+1°	+1°	+2°	+2°	+1°	+1°	+3°	+1°	+1°	+1°	+1°	+2°
Panasonic VBHN240SE10	HIT	+2°	+1°	+2°	+2°	+1°	+1°	+3°	+1°	+1°	+1°	+1°	+2°
REC 260PE	mc-Si	+2°	+1°	+2°	+3°	+1°	+1°	+3°	+1°	+1°	+1°	+2°	+2°
ReneSola JC310M 24Ab	mc-Si	+1°	+1°	+2°	+2°	+1°	+1°	+3°	+1°	+1°	+1°	+1°	+2°
NexPower NH100AT 5A	a-Si	+2°	+1°	+2°	+2°	+1°	+1°	+3°	+1°	+1°	+1°	+0°	+2°
Sharp NA-E140L5	a-Si/ μ c-Si	+2°	+1°	+2°	+2°	+1°	+1°	+3°	+1°	+1°	+1°	+1°	+2°
FirstSolar FS3100 Plus	CdTe	+2°	+1°	+2°	+2°	+1°	+1°	+3°	+1°	+1°	+1°	+1°	+2°
SolarFrontier SF170 S	CIS	+1°	+1°	+1°	+2°	+1°	+2°	+3°	+1°	+1°	+2°	+1°	+2°

Tracking

In order to make the PV projects involving tracking systems economically feasible compared to fixed mount projects, the use of high-efficiency solar modules is usually required. That is why the technological scope of the analysis reported in this section is limited to the four highest-efficiency modules of the sample presented in Table 5-1. Figures 5-23-26 show the results for the modules selected from the TPFT group, SunPower SPR-305-WHT and Sanyo HIP-200BA19, and the remaining four (Figures 5-27-30) for the modules chosen from the MD group, SunPower SPR-455J-WHTD and Panasonic VBHN240SE10. There are two types of figure for each group. The first ones (5-23, 5-25, 5-27, and 5-29) show both the fixed axis angle-dependent variation in the performance of a single axis tracking system and the performance of a dual axis tracking system. The second ones (5-24, 5-26, 5-28, and 5-30) compare the performances of the single axis tracking system and the dual axis tracking system to a corresponding fixed mount system with the same tilt angle as the single axis tracking system's axis angle. Hence, the first figure type shows absolute performance and the second type performance relative to a corresponding fixed mount system.

As can be seen from the absolute performance figures, the optimum fixed axis angle is zero in all site locations. This is not caused by summer conditions being overwhelmingly better for these module types than winter conditions. The reason lies in the row spacing assumptions made in the system configuration algorithm. Row spacing minimisation is subjected to the following constraint: the arrays may not shade each other four hours after the solar noon on the winter solstice. Thus, there is always shading due to other arrays in the morning and evening hours. In the case of tracking systems, the array self-shading is minimised by means of backtracking. In backtracking, the minimisation of ϑ is compromised for a lower shading factor. The higher the maximum array height, the more shading occurs and the more backtracking the operation of a PV plant involves. Array heights can be lowered by reducing the axis angle. Therefore, backtracking used in large-scale systems shifts the optimum axis angle away from the optimal angle of a single array. This problem can be addressed by increasing row spacing and, therefore, reducing the need for backtracking.

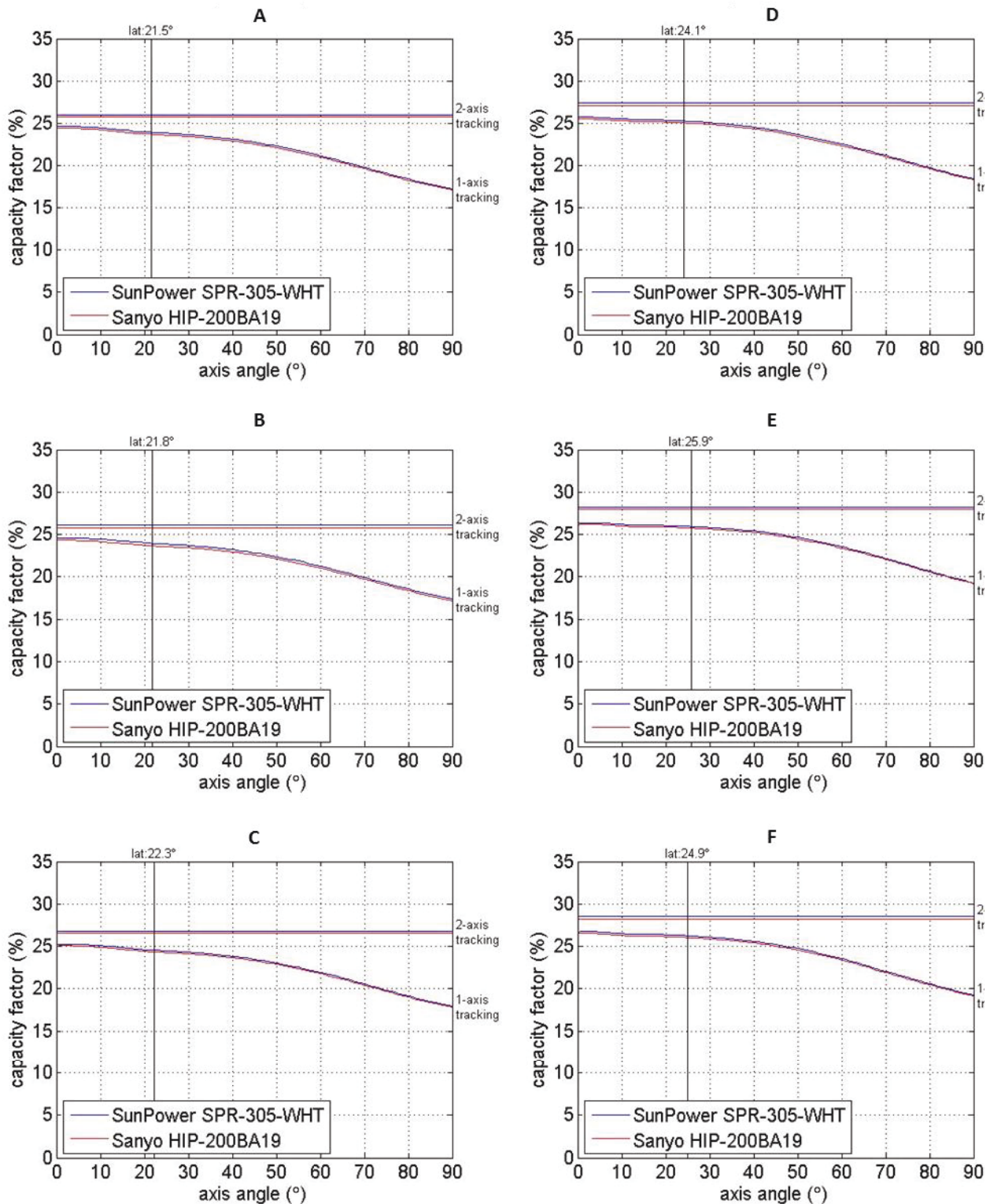


Figure 5-23: Axis angle-dependent variation in the simulated capacity factors of single (and dual) axis tracking systems equipped with the highest-efficiency module types of the TPFT group in the six lowest-DNI site locations. (Other design-specific user inputs: 20 MWp, 100% loading ratio).

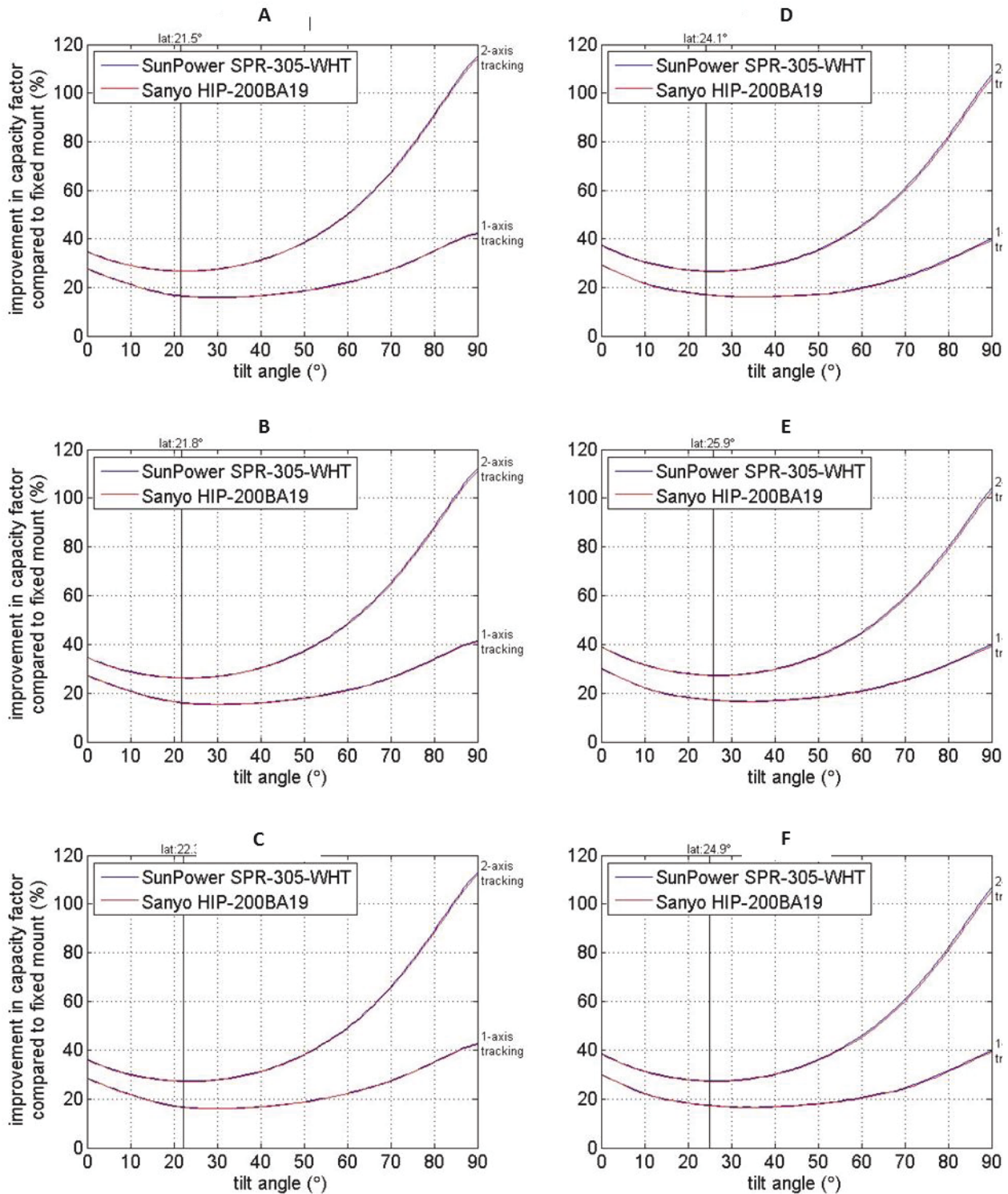


Figure 5-24: POA tilt and axis angle-dependent variation in the relative difference between the simulated capacity factors of fixed mount and tracking systems equipped with the highest-efficiency module types of the TPFT group in the six lowest-DNI site locations. (Other design-specific user inputs: 20 MWp, 100% loading ratio).

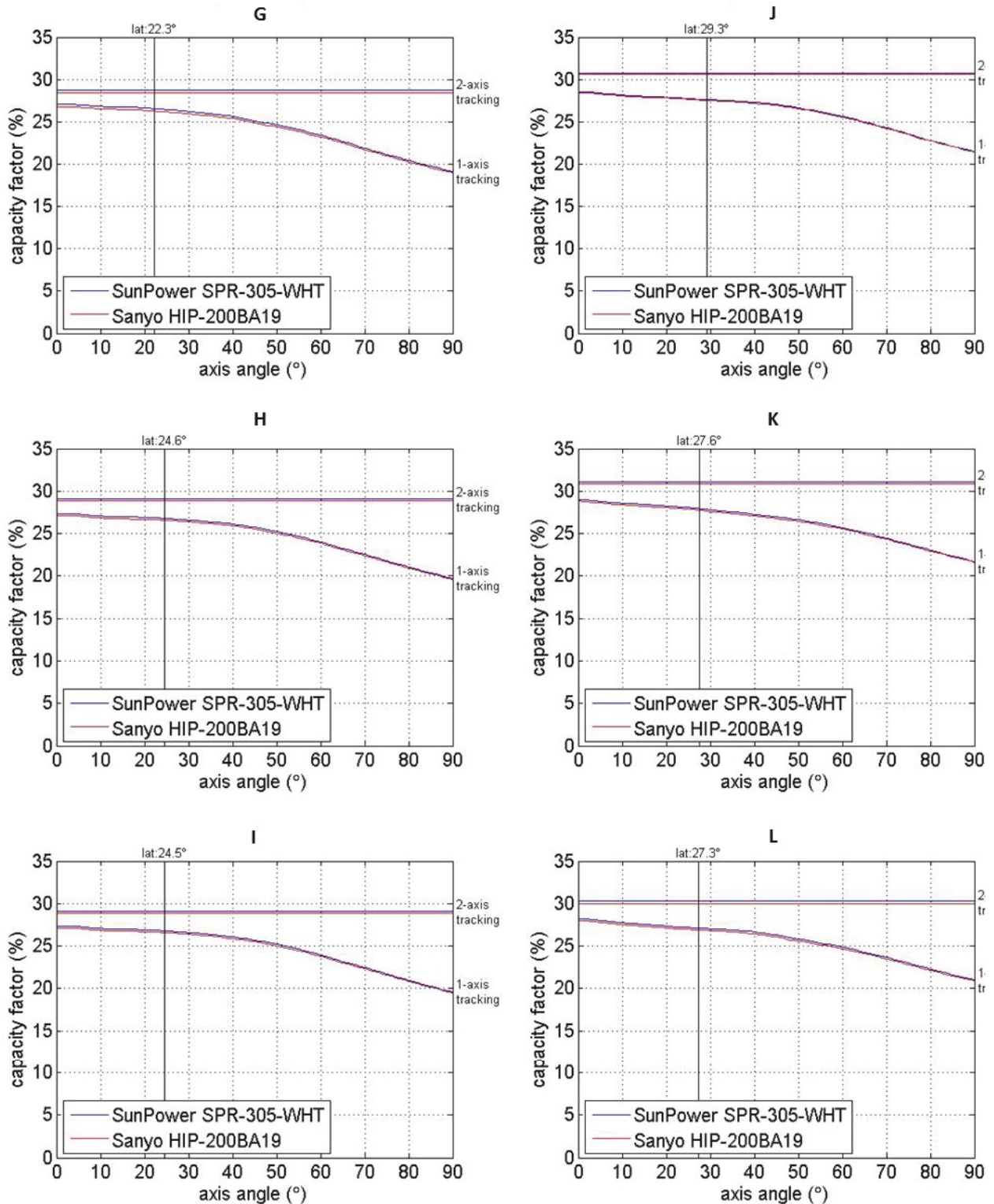


Figure 5-25: Axis angle-dependent variation in the simulated capacity factors of single (and dual) axis tracking systems equipped with the highest-efficiency module types of the TPFT group in the six highest-DNI site locations. (Other design-specific user inputs: 20 MWp, 100% loading ratio).

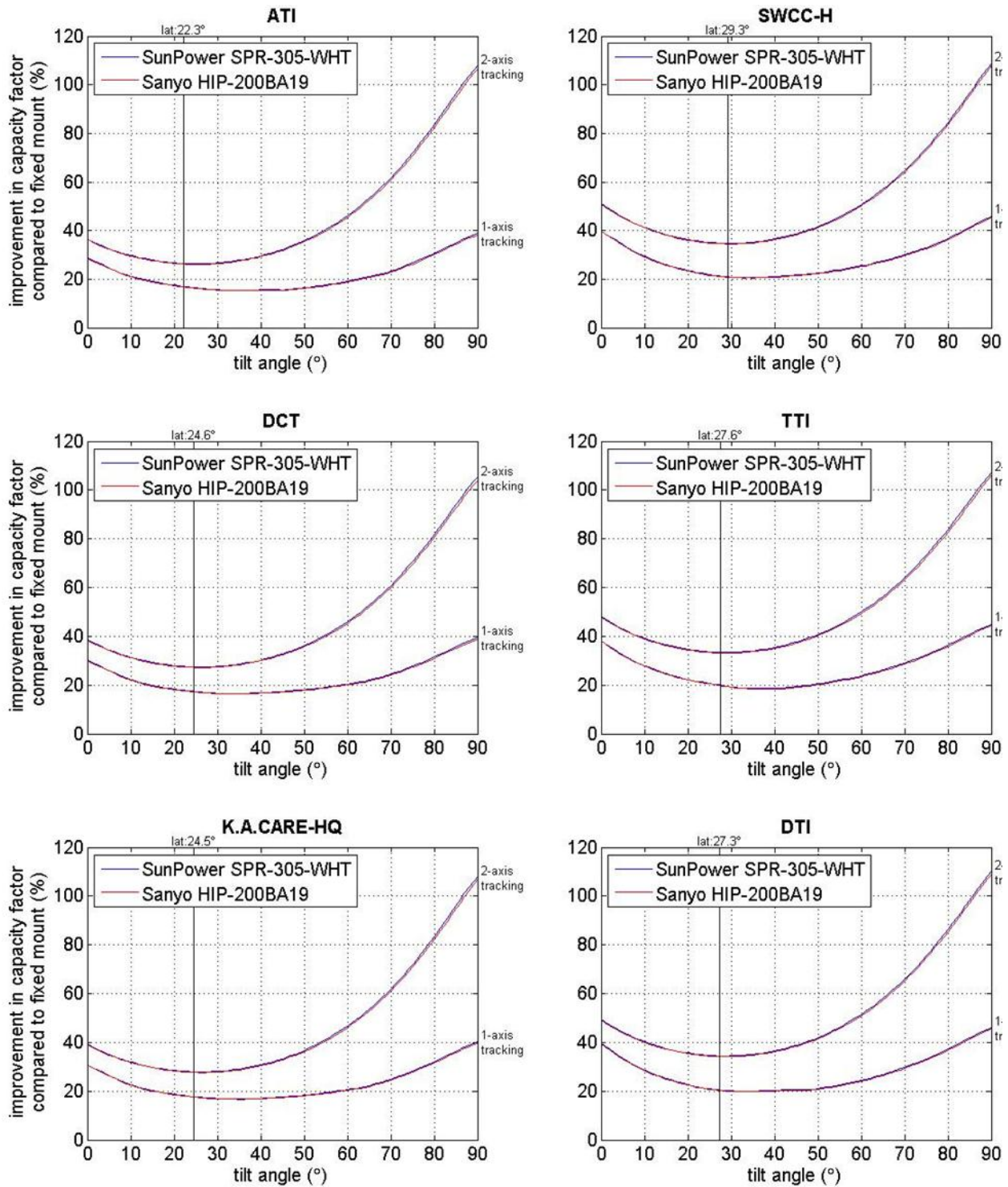


Figure 5-26: POA tilt and axis angle-dependent variation in the relative difference between the simulated capacity factors of fixed mount and tracking systems equipped with the highest-efficiency module types of the TPFT group in the six highest-DNI site locations. (Other design-specific user inputs: 20 MWp, 100% loading ratio).

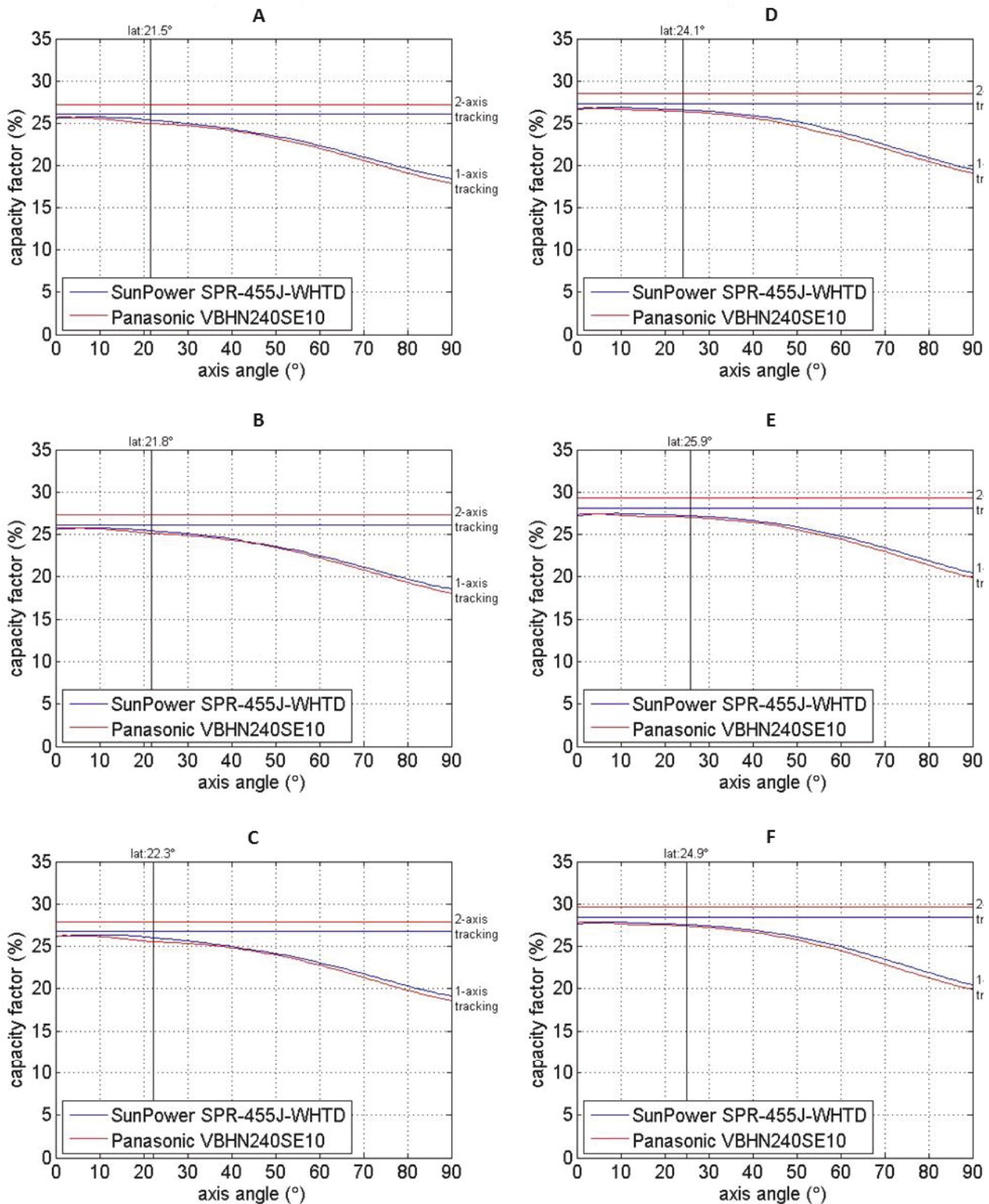


Figure 5-27: Axis angle-dependent variation in the simulated capacity factors of single (and dual) axis tracking systems equipped with the highest-efficiency module types of the MD group in the six lowest-DNI site locations. (Other design-specific user inputs: 20 MWp, 100% loading ratio).

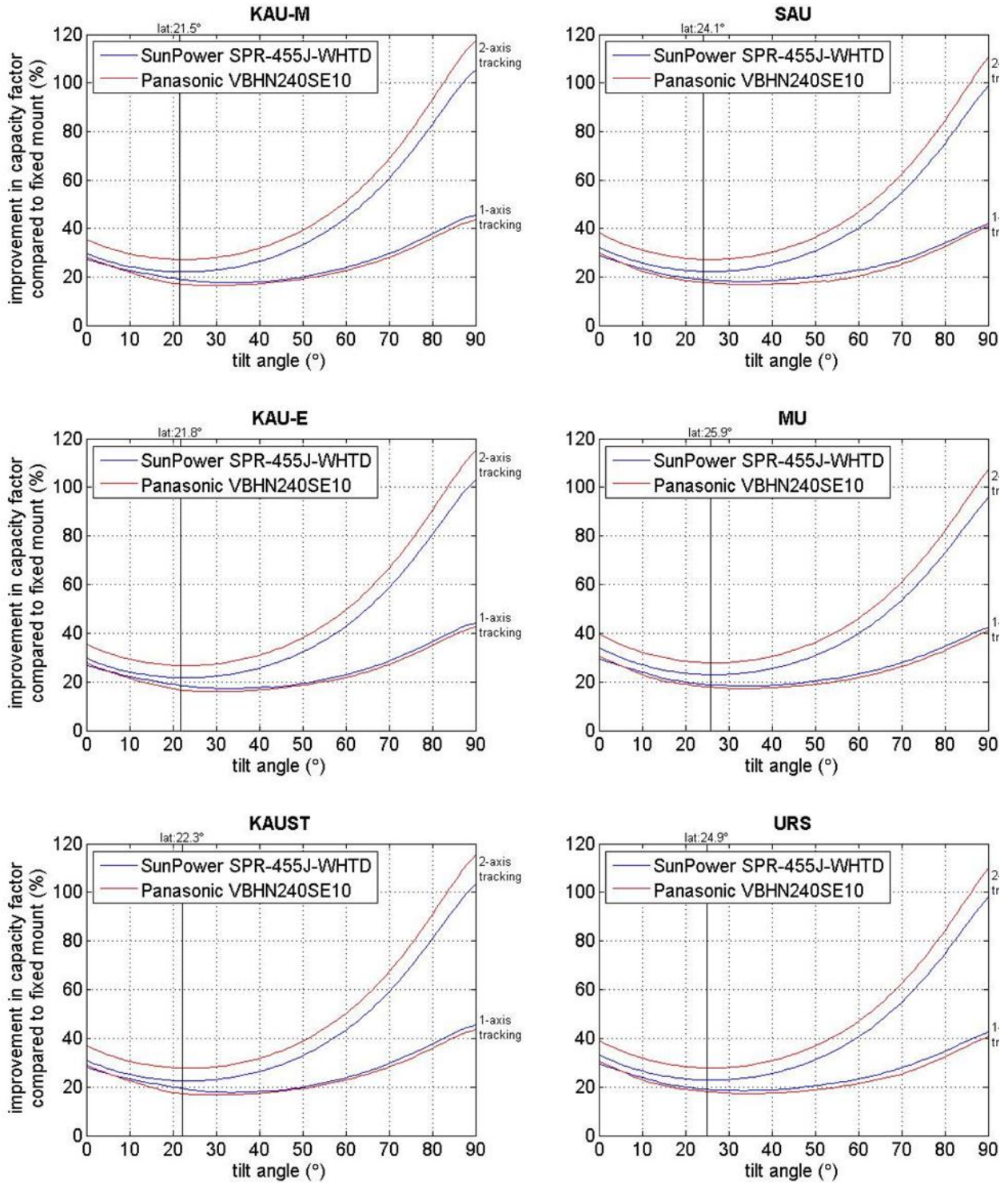


Figure 5-28: POA tilt and axis angle-dependent variation in the relative difference between the simulated capacity factors of fixed mount and tracking systems equipped with the highest-efficiency module types of the MD group in the six lowest-DNI site locations. (Other design-specific user inputs: 20 MWp, 100% loading ratio).

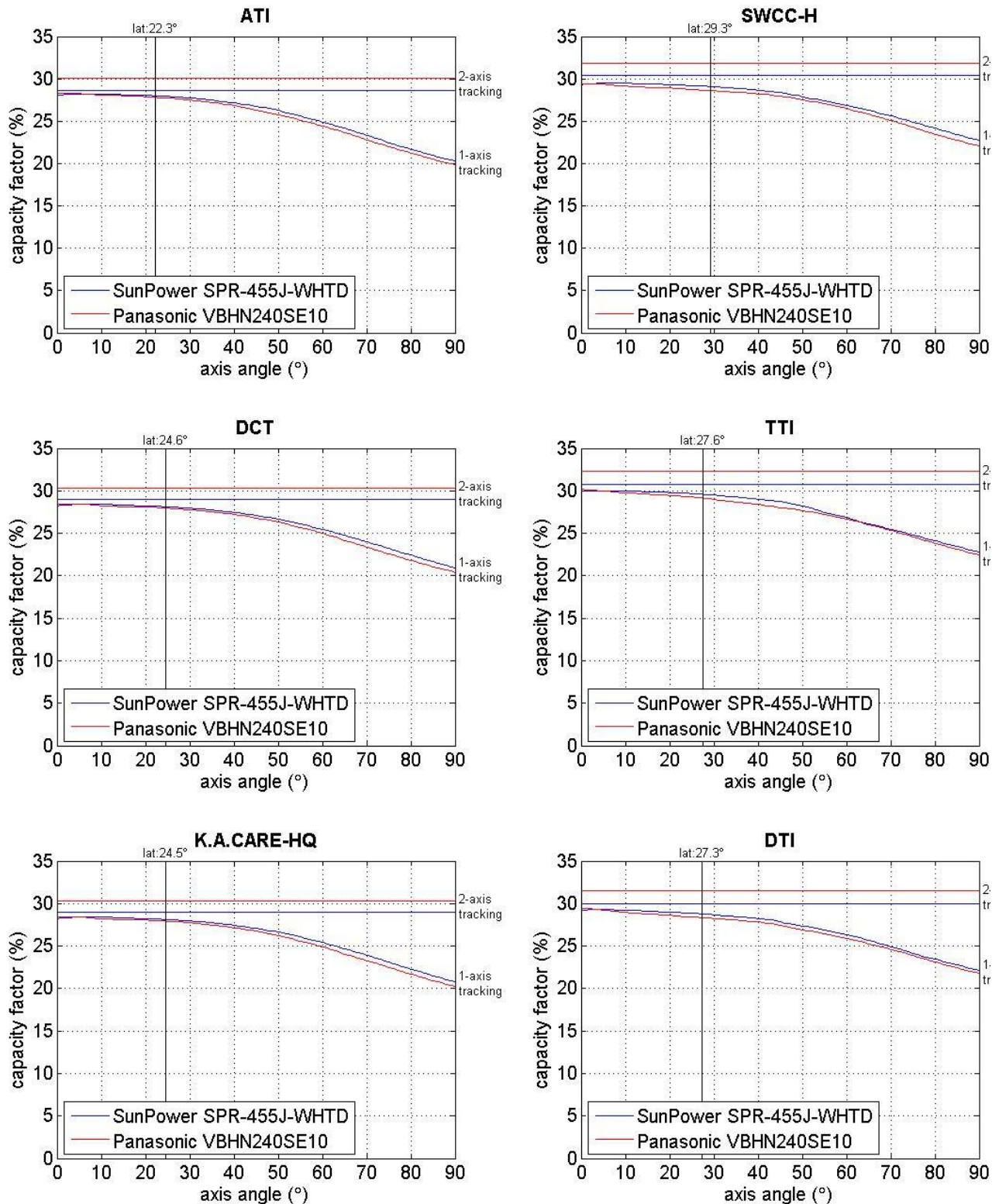


Figure 5-29: Axis angle-dependent variation in the simulated capacity factors of single (and dual) axis tracking systems equipped with the highest-efficiency module types of the MD group in the six highest-DNI site locations. (Other design-specific user inputs: 20 MWp, 100% loading ratio).

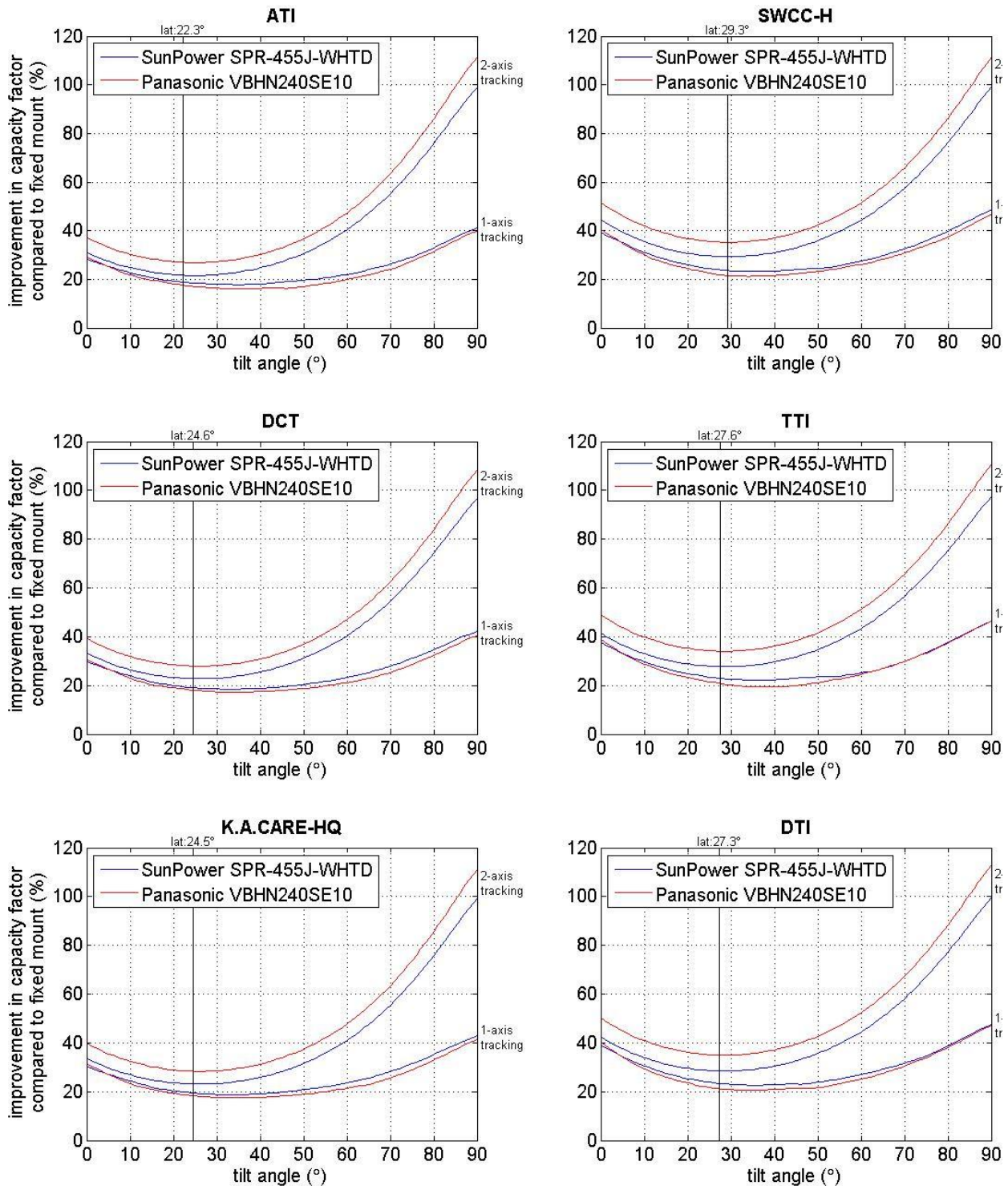


Figure 5-30: POA tilt and axis angle-dependent variation in the relative difference between the simulated capacity factors of fixed mount and tracking systems equipped with the highest-efficiency module types of the MD group in the six highest-DNI site locations. (Other design-specific user inputs: 20 MWp, 100% loading ratio).

The module types of the TPFT group show very similar performance patterns. Though, the c-Si module performs slightly better in most conditions. By contrast, in the case of the MD group, the HIT module performs clearly better in dual-axis tracking systems and, interestingly, the c-Si module somewhat better in single axis tracking systems. The better performance of the HIT module in dual axis tracking systems is caused by its significantly lower temperature coefficient of maximum power. Since in the case of dual axis tracking, effective irradiance levels are comparatively high throughout the day, the module type's thermal

behaviour becomes critical. In the case of single axis tracking however, the importance of the module's low-light behaviour is higher. Panasonic's HIT module belongs to a group of modules that is particularly sensitive to changes in ϑ . This is because of the irradiance-dominated performance variability related to low temperature coefficients mentioned above and the module's relatively poor low-light performance.

Table 5-3: Relative improvement in simulated performance due to tracking for the high-efficiency module types. (Other design-specific user inputs: 20 MWp, 100% loading ratio).

Array design	A	B	C	D	E	F	G	H	I	J	K	L
2- axis												
SunPower SPR-305-WHT	26.8%	26.3%	27.3%	26.8%	27.4%	27.4%	26.3%	27.4%	27.9%	34.8%	33.4%	34.4%
1-axis												
SunPower SPR-305-WHT	20.1%	19.3%	20.1%	19.2%	19.2%	19.5%	19.2%	19.7%	20.1%	24.8%	24.5%	25.5%
2- axis												
Sanyo HIP-200BA19	26.6%	26.1%	27.1%	26.5%	27.1%	27.1%	26.1%	27.2%	27.6%	34.5%	33.2%	34.1%
1-axis												
Sanyo HIP-200BA19	20.0%	19.1%	19.9%	19.0%	19.0%	19.3%	18.9%	19.5%	19.9%	24.6%	24.3%	25.3%
2- axis												
SunPower SPR-455J-WHTD	22.1%	21.7%	22.5%	22.2%	23.0%	22.8%	21.6%	22.8%	23.1%	29.3%	27.7%	28.5%
1-axis												
SunPower SPR-455J-WHTD	20.6%	19.9%	20.7%	19.9%	20.1%	20.3%	19.7%	20.4%	20.7%	25.4%	24.6%	25.6%
2- axis												
Panasonic VBHN240SE10	27.2%	26.7%	27.7%	27.2%	27.8%	27.8%	26.9%	27.9%	28.4%	35.2%	34.0%	35%
1-axis												
Panasonic VBHN240SE10	20.5%	19.7%	20.5%	19.7%	19.7%	20.0%	19.6%	20.2%	20.6%	25.2%	25.0%	25.9%

The relative performance figures show how the lowest points of the relative improvements by single and dual axis tracking systems occur at different tilt angles. This is due to the fact that the performance of a fixed mount system reaches its maximum at a POA tilt angle close to the site latitude whereas a single axis tracking system performs best with a horizontally aligned fixed axis. Table 5-3 can be used to compare the designs with the optimal inclination angles to each other. As predicted in section 5.2, the high DNI levels make Region 3 particularly suitable for tracking systems. The maximum improvements due to a shift from fixed mount to tracking can be reached at Site J, 35.2% for Panasonic's HIT module. Also the other sites of Region 3 experience high gains from tracking: Site L shows the highest improvements for all four single-axis tracking systems. This is because of the high ambient air temperature levels throughout the year (see Figure 5-6) making the performance of a fixed mount system, which is used as a base level for the comparison, relatively poor. Consequently, a single axis tracking system whose performance peaks in the summer's high irradiance period due to its zero axis angle boosts generation at Site L more than at any other site.

5.2.4 Effect of Capacity

Due to the highly modular nature of PV power stations, the effect of plant capacity on the plant's technical performance is known to be minimal. The simulation results are consistent with this common assumption. Figure 5-31 presents the simulated capacity factors for all module types as the function of plant capacity at Site K. The biggest changes in performance occur at capacity levels below 10 MWp where the changes in

array configuration are relatively substantial due to the more likely mismatch with available inverter configurations.

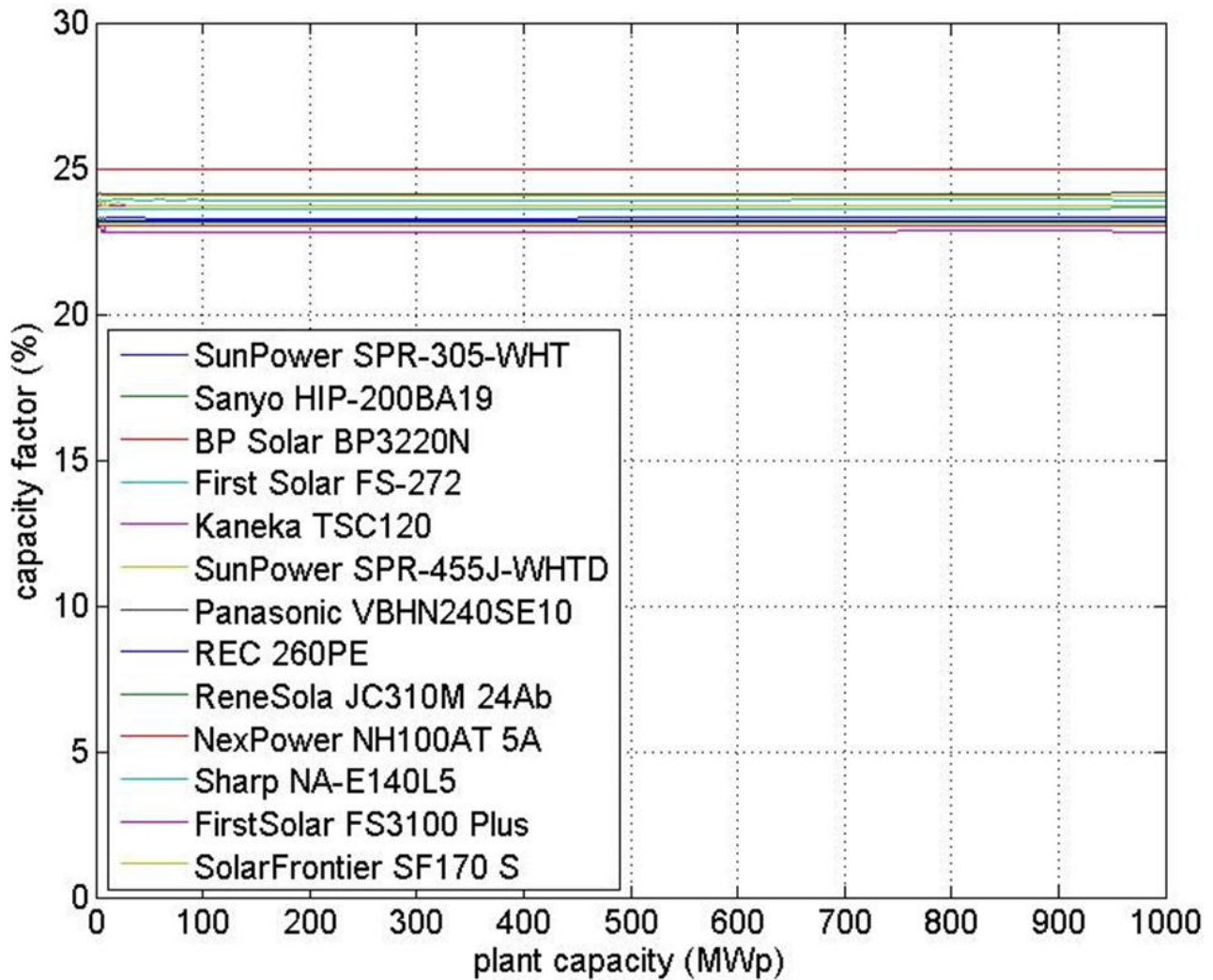


Figure 5-31. Effect of plant capacity on the simulated capacity factors at Site K. (Other design-specific user inputs: fixed mount, latitude tilt, 100% loading ratio).

Because of the architectural modularity of a PV power station, the total plant surface area varies linearly with plant capacity as can be seen from Figure 5-32. The slopes of the lines are dependent on the STC conversion efficiency of the module type used as well as the site latitude due to its impact on row spacing. Due to the latter, Figure 5-32 presents the simulated surface areas for the sites with the highest latitude and the lowest latitude, Site J and Site A.

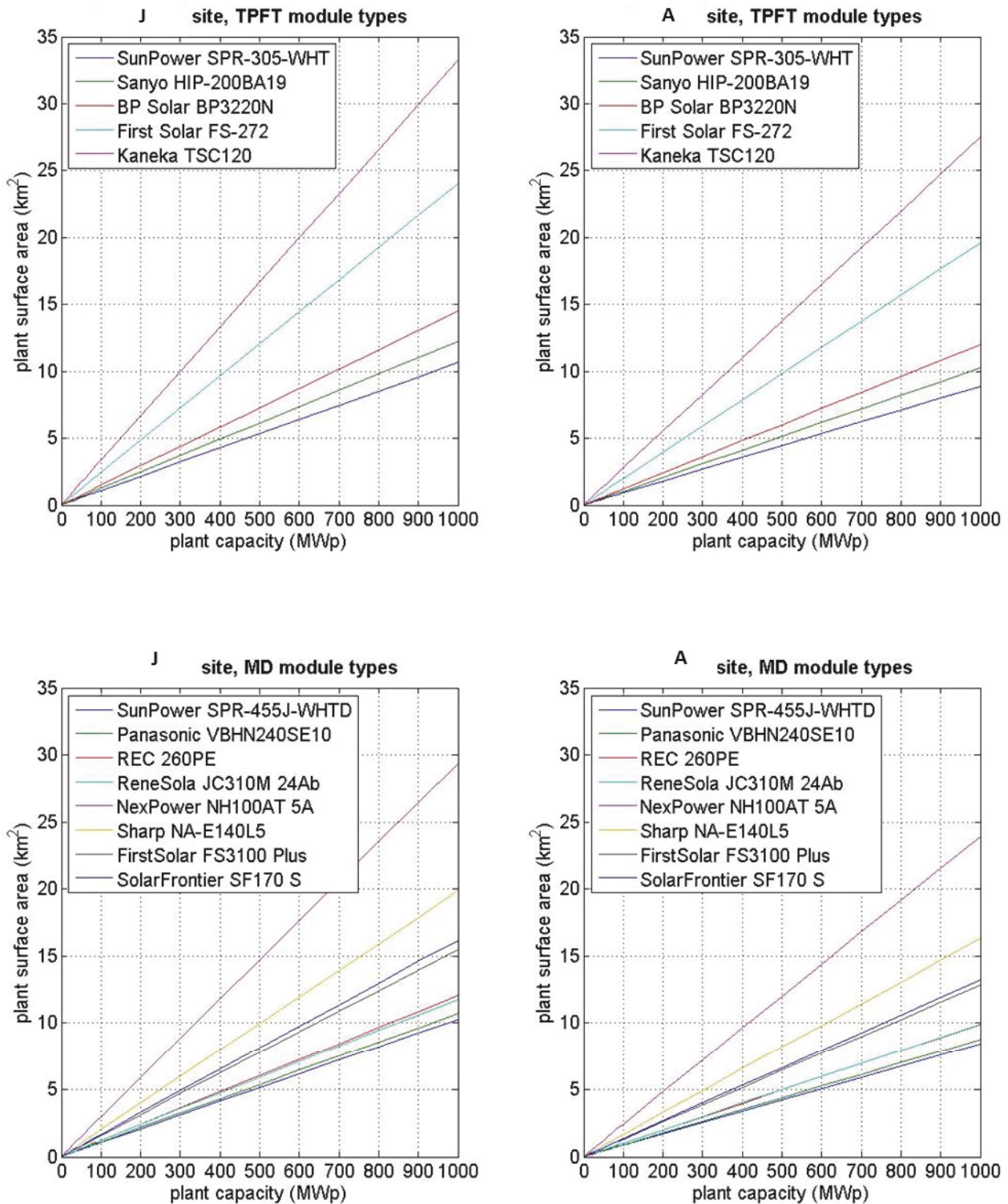


Figure 5-32. Effect of plant capacity on the simulated plant surface areas at the sites of the stations Location J and Location A. (Other design-specific user inputs: fixed mount, latitude tilt, 100% loading ratio).

5.2.5 Effect of Loading Ratio

The ratio of the combined array capacity of a power block to the nominal AC output of the power block's inverter is manipulated by varying the number and capacity of the inverters deployed in the plant. This loading ratio affects plant performance in two ways: through module performance and inverter performance. Module performance is affected via the constraints the inverter sets for its input current and voltage. The ratio determines the maximum level for the current input into the inverter as well as the minimum system voltage at the inlet of the inverter. If array performance slips outside this operational range of the inverter, the arrays are forced to move down on their respective I-V curves in order for the system to raise its voltage level or reduce the current. As the arrays are no longer operated at their MPP, the performance of the power station decreases. A high loading ratio increases the chance of the input current exceeding the maximum, while a low ratio involves a higher probability of below-minimum system voltages.

Ideal sites for PV deployment are the ones characterised by high irradiance levels and low ambient air temperatures and, therefore, have conditions similar to STC. Since average irradiance and temperature levels are highly correlated however, there are few locations on the surface of the Earth where such conditions can be achieved. That is why today's central inverters have been optimised for power ratios ($P_{ac}/P_{ac,0}$) below 50%. Thus, in ideal locations (e.g. sunny high-elevation plateaus in the low latitudes), loading ratios below 100% are required across all PV technologies to avoid frequent overcurrent situations. In the case of the sites in the Arabian Peninsula however, the optimum loading ratio varies on both sides of 100% depending on the particular site conditions and the type of the module used. The plants equipped with modules with high temperature coefficients (low-band gap materials: c-Si, mc-Si, and CIS) perform better on average with high loading ratios (> 105%). In the case of these module types, rising cell temperature decreases system voltage more than what it does with modules made of high-band gap materials (CdTe, a-Si, a-Si/ μ c-Si, and CIGS). As a result, more arrays are required to keep the system voltage within the operational range of the inverter and in that way maximise the output. Consequently, the optimal loading ratio is shifted upwards. Power stations equipped with high-band gap material modules show on average higher system voltage levels and, thus, less frequently operate outside the MPP range due to temperature-induced below-minimum system MPP voltages. As inverter performance goes down with rising voltage, however, the performance of such plants is maximised by lower loading ratios.

Table 5-4. The simulated optimal loading ratios for the considered module types and site locations. (Other design-specific user inputs: fixed mount, latitude tilt, 20 MWp).

Module Type	A	B	C	D	E	F	G	H	I	J	K	L
SunPower SPR-305-WHT	121%	121%	121%	125%	125%	125%	121%	125%	125%	125%	125%	125%
Sanyo HIP-200BA19	126%	126%	126%	120%	104%	104%	104%	104%	104%	104%	104%	120%
BP Solar BP3220N	113%	113%	113%	113%	113%	113%	113%	113%	113%	106%	106%	106%
First Solar FS-272	105%	105%	105%	105%	105%	105%	105%	105%	105%	105%	105%	105%
Kaneka TSC120	84%	84%	84%	84%	84%	84%	84%	84%	84%	84%	84%	84%
SunPower SPR-455J-WHTD	125%	125%	125%	125%	125%	125%	125%	107%	125%	120%	107%	125%
Panasonic VBHN240SE10	121%	121%	121%	121%	121%	121%	121%	121%	121%	121%	121%	121%
REC 260PE	122%	122%	122%	122%	122%	122%	122%	122%	122%	122%	122%	122%
ReneSola JC310M 24Ab	123%	123%	123%	123%	123%	123%	123%	123%	123%	123%	123%	123%
NexPower NH100AT 5A	98%	98%	98%	98%	98%	98%	98%	98%	98%	89%	98%	98%
Sharp NA-E140L5	112%	112%	112%	112%	99%	99%	95%	95%	95%	95%	95%	112%
FirstSolar FS3100 Plus	114%	110%	110%	110%	97%	97%	97%	97%	97%	97%	97%	97%
SolarFrontier SF170 S	97%	96%	96%	90%	90%	90%	90%	90%	90%	89%	90%	90%

The outcome of the optimisation of loading ratios for the sites considered in this study is presented in Table 5-4. The results are mostly consistent with the above discussion. The use of thin-film modules characterised by low temperature coefficients leads to low optimum loading ratios while wafer-based modules perform better with higher ratios. Also, the region's most favourable sites in Region 3 tend to have lower optimum loading ratios than the sites in Region 2. There are exceptions to this general trend, however. Some module types have almost equivalent loading ratios at all sites and in the case of BP Solar's mc-Si module, the optimal ratios are actually the highest in Region 3. These inconsistencies are due to the fact that on annual average, the actual effect of loading ratio on module and inverter performance is so low that the impact of the related changes in system configuration might actually be the dominating effect. This can be seen in Figure 4 26 which shows the effect of loading ratios on the simulated capacity factors at a typical site with a low optimum loading ratio, Location J, and a site characterised by a high optimum ratio, Location A. In both locations, the performance gain from choosing the optimum ratio over the default one of 100% is 1% at most.

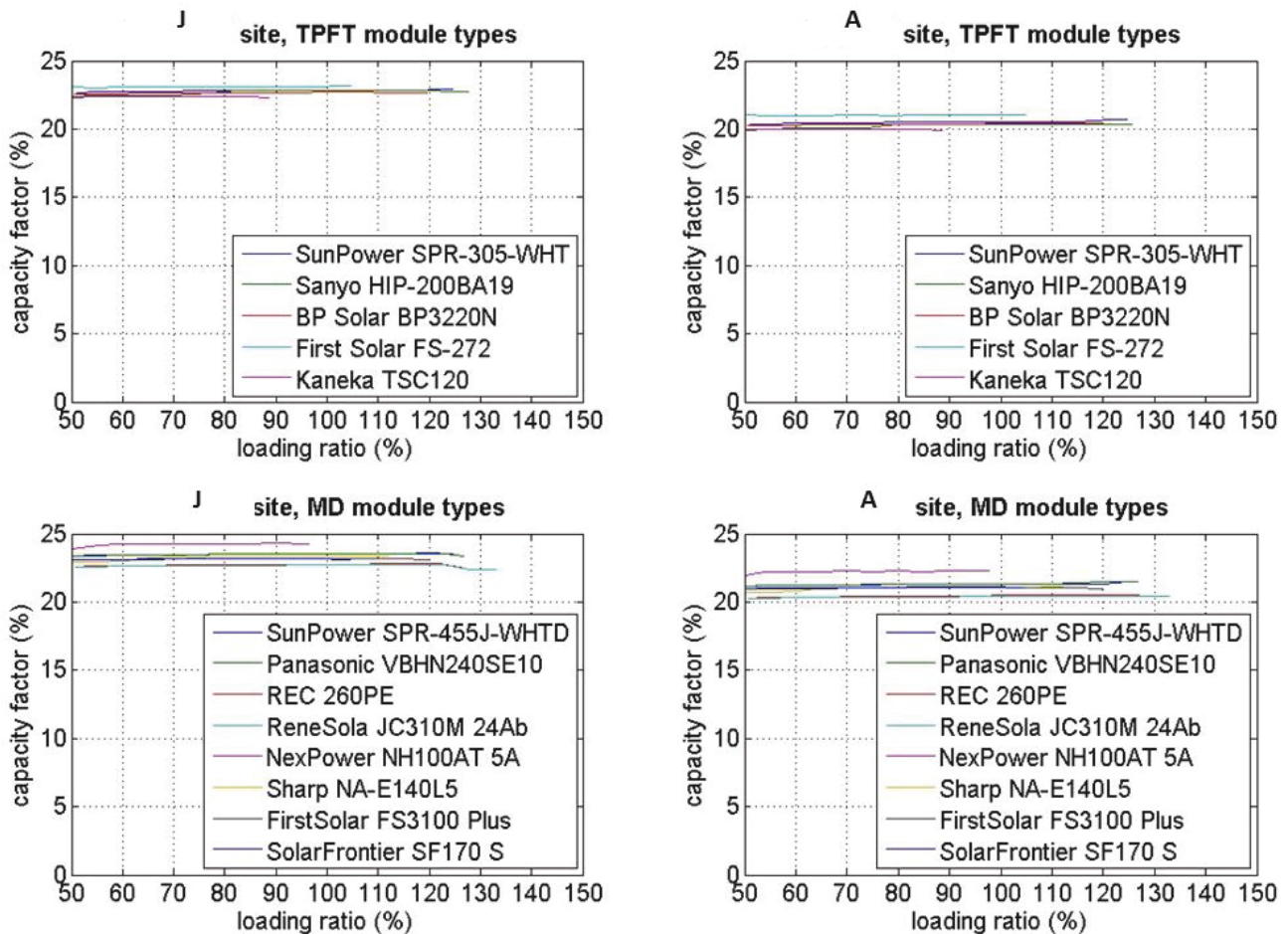


Figure 5-33. Effect of loading ratio on the simulated plant surface areas at Site J and Site A. (Other design-specific user inputs: fixed mount, latitude tilt, 20 MWp).

5.3 Discussion

The primary objective of this case study is to give an overview of the likely technical performance that different kinds of PV power stations would show in three different regions of the Arabian Peninsula. The spread of the monitoring stations can be estimated to be sufficient for region-specific evaluations of the different meteorological parameters relevant for PV performance within the timeframe of the study. Due to the short time period (one year) however, the generalisation of the data's seasonal variability to other years might be problematic. For instance, the time of the vernal peak in DNI might experience annual variation and lead to notable variability in the optimal POA inclination angles of different years.

Since locally measured PV performance data are not available for a sufficiently large sample of different module types, the assessment has to rely on measurements made by SNL and Photon Magazine as well as the manufacturers themselves. This poses some challenges to the credibility of the results, for which reason no conclusions can be made regarding the suitability of single module brands. The general findings related to the best-performing module types are, however, consistent between the two different module samples and can, therefore, be considered reliable. In both cases, thin-film modules with low temperature coefficients of maximum power show the best performances in all locations. Such outcome can be expected when assessing PV performance in hot desert conditions. Also, the results of the assessment of different mounting methods are well aligned with what can be expected based on the spatial variability of the DNI measurements.

In addition to the problems related to data quality, there are issues in the design of the simulator that need to be addressed in order to improve the accuracy of the simulator's output specifically in hot desert conditions. The most significant shortcoming is the insufficient soiling model. Since the effect of dust deposition does not have dependence on any ambient parameter, it is assumed that the soiling loss is either non-existent or constant with time. Due to the strongly variable aerosol loading typical of hot desert conditions, this assumption cannot be regarded as realistic. The other dust-related issue that should be taken into consideration is the effect of atmospheric dust on the spectrum of incident sunlight. This is important as solar cells are spectrally sensitive devices. Currently, there is no spectral model integrated in the simulator. Both these effects might significantly influence PV performance but their quantification is currently difficult due to the lack of appropriate data. In addition to the development of these new models, the local validation of the optical, thermal, and electrical models has to be performed. The two latter require sufficiently diverse samples of test field sites and different solar module types to be tested.

As the thesis specifically addresses the technical performance of PV power stations, economic factors are only considered in system design-related assumptions made for the simulation algorithm and when defining the technological scope for the assessment of the performance effect of tracking. The module types that have the best technical match with the site locations might not give the lowest levelised cost of electricity, which eventually dictates the feasibility of an investment in a PV power station. In addition to the price-per-Wp of a module type, an important economic factor to be considered is the expense of the required balance of system (BOS) equipment. For instance, using a thin-film module whose STC conversion efficiency is half of the efficiency of a c-Si module roughly doubles the required number of arrays and the total plant surface area. This point is getting increasingly important as the BOS share of the total cost of PV power stations is likely to rise with continuously sinking module prices.

6. Conclusion

The Arabian Peninsula is an interesting region from a PV performance modeller's perspective. On one hand, it is characterised by tremendous abundance of solar resource but, on the other hand, influenced by severe aerosol loading and exceptionally high ambient temperatures. While the impacts of temperature and irradiance on PV performance are well-known, there is a lot to be done in improving modelling tools related to both atmospheric dust and the dust deposited on arrays. It can therefore be expected that particularly purely physical optical models face difficulties in producing accurate estimates. It seems clear that the dust-related spectrally sensitive attenuation of sunlight and its dependence on ambient conditions should be the focal point of the future PV performance modelling-related research in the UAE and elsewhere in the Arabian Peninsula.

This thesis specifies modelling tools that are particularly useful in addressing the particularities of both the WebGIS environment and the hot desert conditions. In general, semi-empirical models often turn out to be the best options as they are both flexible with recalibration and computationally light due to analytically solvable steady state-based equations. Through appropriate model selection and computational methods, it has been possible to reduce the time required for country-level simulations from hours to minutes. Through a case study applying actual meteorological measurements, it is shown that the model produces highly plausible results. Though, the only component validated based on locally collected measurements is the thermal model. Without actual performance data however, much cannot be said about the simulator's performance in terms of accuracy. Nevertheless, the model developed as an outcome of this thesis project gives a good starting point for the WebGIS-based PV performance simulator to be integrated in the UAE Solar Atlas.

Bibliography

- Al-Hasan, A.Y., 1998. A new correlation for direct beam solar radiation received by photovoltaic panel with sand dust accumulated on its surface. *Sol. Energy* 63, 323–333. doi:10.1016/S0038-092X(98)00060-7
- Alonso-García, M.C., Ruiz, J.M., Herrmann, W., 2006. Computer simulation of shading effects in photovoltaic arrays. *Renew. Energy* 31, 1986–1993. doi:10.1016/j.renene.2005.09.030
- Anderson, M., 2014. PVSIM Update.
- Arora, J.D., Verma, A.V., Bhatnagar, M., 1986. Variation of series resistance with temperature and illumination level in diffused junction poly- and single-crystalline silicon solar cells. *J. Mater. Sci. Lett.* 5, 1210–1212. doi:10.1007/BF01729367
- ASHRAE, 1978. Methods of Testing to Determine the Thermal Performance of Solar Collectors.
- Badescu, V., 2002. 3D isotropic approximation for solar diffuse irradiance on tilted surfaces. *Renew. Energy* 26, 221–233. doi:10.1016/S0960-1481(01)00123-9
- Banerjee, S., Anderson, W.A., 1986. Temperature dependence of shunt resistance in photovoltaic devices. *Appl. Phys. Lett.* 49, 38–40. doi:10.1063/1.97076
- Bartlett, J.S., Ciotti, Á.M., Davis, R.F., Cullen, J.J., 1998. The spectral effects of clouds on solar irradiance. *J. Geophys. Res. Oceans* 103, 31017–31031. doi:10.1029/1998JC900002
- Bätzner, D.L., Romeo, A., Zogg, H., Tiwari, A.N., 2001. CdTe/CdS solar cell performance under low irradiance. Presented at the 17th EC PVSEC, Munich, Germany.
- Baumgartner, F.P., Schmidt, H., Burger, B., Bründlinger, R., Häberlin, H., Zehner, M., 2007. Status and relevance of the DC voltage dependency of the inverter efficiency, in: Proceedings. Presented at the 22nd European Photovoltaic Solar Energy Conference and Exhibition, Milan, Italy.
- Beegum, S.N., 2014. Personal communication.
- Betts, T.R., Gottschalg, R., Infield, D.G., 2003. ASPIRE - a tool to investigate spectral effects on PV device performance, in: Proceedings of 3rd World Conference on Photovoltaic Energy Conversion, 2003. Presented at the Proceedings of 3rd World Conference on Photovoltaic Energy Conversion, 2003, pp. 2182–2185 Vol.3.
- Bird, R.E., Riordan, C., 1986. Simple Solar Spectral Model for Direct and Diffuse Irradiance on Horizontal and Tilted Planes at the Earth's Surface for Cloudless Atmospheres. *J. Clim. Appl. Meteorol.* 25, 87–97. doi:10.1175/1520-0450(1986)025<0087:SSSMFD>2.0.CO;2
- Blanco-Muriel, M., Alarcón-Padilla, D.C., López-Moratalla, T., Lara-Coira, M., 2001. Computing the solar vector. *Sol. Energy* 70, 431–441. doi:10.1016/S0038-092X(00)00156-0
- Blanc, P., Wald, L., 2012. The SG2 algorithm for a fast and accurate computation of the position of the Sun for multi-decadal time period. *Sol. Energy* 86, 3072–3083. doi:10.1016/j.solener.2012.07.018
- Braun, J.E., Mitchell, J.C., 1983. Solar geometry for fixed and tracking surfaces. *Sol. Energy* 31, 439–444. doi:10.1016/0038-092X(83)90046-4
- Breitenstein, O., Rißland, S., 2013. A two-diode model regarding the distributed series resistance. *Sol. Energy Mater. Sol. Cells* 110, 77–86. doi:10.1016/j.solmat.2012.11.021
- Brendel, R., Queisser, H.J., 1993. On the thickness dependence of open circuit voltages of p-n junction solar cells. *Sol. Energy Mater. Sol. Cells* 29, 397–401. doi:10.1016/0927-0248(93)90098-N
- Bugler, J.W., 1977. The determination of hourly insolation on an inclined plane using a diffuse irradiance model based on hourly measured global horizontal insolation. *Sol. Energy* 19, 477–491. doi:10.1016/0038-092X(77)90103-7
- Bunea, G.E., Wilson, K.E., Meydbray, Y., Campbell, M.P., De Ceuster, D.M., 2006. Low Light Performance of Mono-Crystalline Silicon Solar Cells, in: Conference Record of the 2006 IEEE 4th World Conference on Photovoltaic Energy Conversion. Presented at the Conference Record of the 2006 IEEE 4th World Conference on Photovoltaic Energy Conversion, pp. 1312–1314. doi:10.1109/WCPEC.2006.279655
- Cameron, C.P., Boyson, W.E., Riley, D.M., 2008. Comparison of PV system performance-model predictions with measured PV system performance, in: 33rd IEEE Photovoltaic Specialists Conference, 2008.

BIBLIOGRAPHY

- PVSC '08. Presented at the 33rd IEEE Photovoltaic Specialists Conference, 2008. PVSC '08, pp. 1–6. doi:10.1109/PVSC.2008.4922865
- Carlsson, T., Brinkman, A., 2006. Identification of degradation mechanisms in field-tested CdTe modules. *Prog. Photovolt. Res. Appl.* 14, 213–224. doi:10.1002/pip.663
- Chu, T.L., Chu, S.S., 1995. Thin film II–VI photovoltaics. *Solid-State Electron.* 38, 533–549. doi:10.1016/0038-1101(94)00203-R
- Contreras, M.A., Romero, M., Young, M., 2003. Optimization of CuGaSe/sub 2/ for wide-bandgap solar cells, in: *Proceedings of 3rd World Conference on Photovoltaic Energy Conversion*, 2003. Presented at the *Proceedings of 3rd World Conference on Photovoltaic Energy Conversion*, 2003, pp. 2864–2868 Vol.3.
- Corwine, C.R., Pudov, A.O., Gloeckler, M., Demtsu, S.H., Sites, J.R., 2004. Copper inclusion and migration from the back contact in CdTe solar cells. *Sol. Energy Mater. Sol. Cells* 82, 481–489. doi:10.1016/j.solmat.2004.02.005
- David, M., Lauret, P., Boland, J., 2013. Evaluating tilted plane models for solar radiation using comprehensive testing procedures, at a southern hemisphere location. *Renew. Energy* 51, 124–131. doi:10.1016/j.renene.2012.08.074
- DEGERenergie GmbH & Co. KG, 2014. Open Land [WWW Document]. Open Land. URL <http://www.degerenergie.de/en/open-land.html> (accessed 11.20.14).
- De Soto, W., Klein, S.A., Beckman, W.A., 2006. Improvement and validation of a model for photovoltaic array performance. *Sol. Energy* 80, 78–88. doi:10.1016/j.solener.2005.06.010
- Di Dio, V., La Cascia, D., Miceli, R., Rando, C., 2009. A mathematical model to determine the electrical energy production in photovoltaic fields under mismatch effect, in: *2009 International Conference on Clean Electrical Power*. Presented at the *2009 International Conference on Clean Electrical Power*, pp. 46–51. doi:10.1109/ICCEP.2009.5212083
- Diez-Mediavilla, M., Bilbao, J., de Miguel, A., 2006. Erratum to “Measurement and comparison of diffuse solar irradiance models on inclined surfaces in Valladolid (Spain)” [*Energy Conversion and Management* 46 (2005) 2075–2092]. *Energy Convers. Manag.* 47, 3504–3506. doi:10.1016/j.enconman.2006.02.026
- Diez-Mediavilla, M., de Miguel, A., Bilbao, J., 2005. Measurement and comparison of diffuse solar irradiance models on inclined surfaces in Valladolid (Spain). *Energy Convers. Manag.* 46, 2075–2092. doi:10.1016/j.enconman.2004.10.023
- Ding, J., Cheng, X., Fu, T., 2005. Analysis of series resistance and P–T characteristics of the solar cell. *Vacuum* 77, 163–167. doi:10.1016/j.vacuum.2004.08.019
- Dongaonkar, S., Karthik, Y., Mahapatra, S., Alam, M.A., 2011. Physics and Statistics of Non-Ohmic Shunt Conduction and Metastability in Amorphous Silicon p-n Solar Cells. *IEEE J. Photovolt.* 1, 111–117. doi:10.1109/JPHOTOV.2011.2174030
- Dongaonkar, S., Servaites, J.D., Ford, G.M., Loser, S., Moore, J., Gelfand, R.M., Mohseni, H., Hillhouse, H.W., Agrawal, R., Ratner, M.A., Marks, T.J., Lundstrom, M.S., Alam, M.A., 2010. Universality of non-Ohmic shunt leakage in thin-film solar cells. *J. Appl. Phys.* 108, 124509. doi:10.1063/1.3518509
- Driesse, A., Jain, P., Harrison, S., 2008. Beyond the curves: Modeling the electrical efficiency of photovoltaic inverters, in: *33rd IEEE Photovoltaic Specialists Conference*, 2008. PVSC '08. Presented at the *33rd IEEE Photovoltaic Specialists Conference*, 2008. PVSC '08, pp. 1–6. doi:10.1109/PVSC.2008.4922827
- Dubovik, O., Holben, B., Eck, T.F., Smirnov, A., Kaufman, Y.J., King, M.D., Tanré, D., Slutsker, I., 2002. Variability of Absorption and Optical Properties of Key Aerosol Types Observed in Worldwide Locations. *J. Atmospheric Sci.* 59, 590–608. doi:10.1175/1520-0469(2002)059<0590:VOAAOP>2.0.CO;2
- Duffie, J.A., Beckman, W.A., 2006. *Solar Engineering of Thermal Processes*. John Wiley & Sons.
- E21 Committee, 2014. *Standard Solar Constant and Zero Air Mass Solar Spectral Irradiance Tables*. ASTM International.
- Erbs, D.G., Klein, S.A., Duffie, J.A., 1982. Estimation of the diffuse radiation fraction for hourly, daily and monthly-average global radiation. *Sol. Energy* 28, 293–302. doi:10.1016/0038-092X(82)90302-4

BIBLIOGRAPHY

- Evans, D.L., 1981. Simplified method for predicting photovoltaic array output. *Sol. Energy* 27, 555–560. doi:10.1016/0038-092X(81)90051-7
- Evseev, E.G., Kudish, A.I., 2009. The assessment of different models to predict the global solar radiation on a surface tilted to the south. *Sol. Energy* 83, 377–388. doi:10.1016/j.solener.2008.08.010
- Fonthal, G., Tirado-Mejía, L., Marín-Hurtado, J.I., Ariza-Calderón, H., Mendoza-Alvarez, J.G., 2000. Temperature dependence of the band gap energy of crystalline CdTe. *J. Phys. Chem. Solids* 61, 579–583. doi:10.1016/S0022-3697(99)00254-1
- Freeman, J., Whitmore, J., Kaffine, L., Blair, N., Dobos, A.P., 2013. System Advisor Model: Flat Plate Photovoltaic Performance Modeling Validation Report (No. NREL/TP-6A20-60204). National Renewable Energy Laboratory (NREL), Golden, CO.
- G03 Committee, 2012. Tables for Reference Solar Spectral Irradiances: Direct Normal and Hemispherical on 37 Tilted Surface. ASTM International.
- Geiger, M., Diabaté, L., Ménard, L., Wald, L., 2002. A web service for controlling the quality of measurements of global solar irradiation. *Sol. Energy* 73, 475–480. doi:10.1016/S0038-092X(02)00121-4
- Gherboudj, I., Ghedira, H., 2014. Spatiotemporal assessment of dust loading over the United Arab Emirates. *Int. J. Climatol.* 34, 3321–3335. doi:10.1002/joc.3909
- Gracia, A.M., Huld, T., 2013. Performance comparison of different models for the estimation of global irradiance on inclined surfaces. Joint Research Centre, European Commission, Ispra, Italy.
- Green, M.A., 1984. Limits on the open-circuit voltage and efficiency of silicon solar cells imposed by intrinsic Auger processes. *IEEE Trans. Electron Devices* 31, 671–678. doi:10.1109/T-ED.1984.21588
- Grena, R., 2008. An algorithm for the computation of the solar position. *Sol. Energy* 82, 462–470. doi:10.1016/j.solener.2007.10.001
- Griffith, J.S., Rathod, M.S., Paslaski, J., 1981. Some tests of flat plate photovoltaic module cell temperatures in simulated field conditions, in: Conference Record. Presented at the Photovoltaic Specialists Conference, NASA, Kissimmee, FL, USA, pp. 822–830.
- Gueymard, C., 1986. RADIATION ON TILTED PLANES : A PHYSICAL MODEL ADAPTABLE TO ANY COMPUTATIONAL TIME-STEP, in: HOLLANDS, E.B.G.T. (Ed.), *Intersol Eighty Five*. Pergamon, Oxford, pp. 2463–2467.
- Gueymard, C., 1987. An anisotropic solar irradiance model for tilted surfaces and its comparison with selected engineering algorithms. *Sol. Energy* 38, 367–386. doi:10.1016/0038-092X(87)90009-0
- Gueymard, C., 1995. SMARTS2: a simple model of the atmospheric radiative transfer of sunshine: algorithms and performance assessment. Florida Solar Energy Center Cocoa, FL.
- Gueymard, C.A., 2001. Parameterized transmittance model for direct beam and circumsolar spectral irradiance. *Sol. Energy* 71, 325–346. doi:10.1016/S0038-092X(01)00054-8
- Guggenheim, E.A., 1949. *Thermodynamics: an advanced treatment for chemists and physicists*. North-Holland Pub. Co.
- Gustav Hensel GmbH & Co. KG, 2014. Mi PV 3941 [WWW Document]. Mi PV 3941. URL <http://www.hensel-electric.de/de/produkte/index.php?IdTreeGroup=6903&IdProduct=7885> (accessed 11.21.14).
- Hacke, P., Terwilliger, K., Smith, R., Glick, S., Pankow, J., Kempe, M., Bennett, S.K.I., Kloos, M., 2011. System voltage potential-induced degradation mechanisms in PV modules and methods for test, in: 2011 37th IEEE Photovoltaic Specialists Conference (PVSC). Presented at the 2011 37th IEEE Photovoltaic Specialists Conference (PVSC), pp. 000814–000820. doi:10.1109/PVSC.2011.6186079
- Hay, J.E., Davies, J.A., 1978. Calculations of the solar radiation incident on an inclined surface, in: *Proceedings. Presented at the First Canadian Solar Radiation Data Workshop, Ministry of Supply and Services, Toronto, ON, Canada*, p. 59.
- Honsberg, C., Bowden, S., 2014. Degradation and Failure Modes.
- Hottel, H.C., Woertz, B.B., 1942. Evaluation of flat-plate solar heat collector. *Trans. ASME* 64, 91–104.
- Igalson, M., Zabierowski, P., Prządo, D., Urbaniak, A., Edoff, M., Shafarman, W.N., 2009. Understanding defect-related issues limiting efficiency of CIGS solar cells. *Sol. Energy Mater. Sol. Cells* 93, 1290–1295. doi:10.1016/j.solmat.2009.01.022

BIBLIOGRAPHY

- Institution of Engineering & Technology, 2008. IEE Wiring Regulations 17th Edition : (BS 7671: 2008) (With BS7671: 2008 Corrigendum, 17th Ed. ed. The Institution of Engineering and Technology, Stevenage, UK.
- Ishaque, K., Salam, Z., Taheri, H., Syafaruddin, 2011. Modeling and simulation of photovoltaic (PV) system during partial shading based on a two-diode model. *Simul. Model. Pract. Theory* 19, 1613–1626. doi:10.1016/j.simpat.2011.04.005
- Jimenez, J.I., Castro, Y., 1986. . Presented at the National assembly of geophysics and geodesy, p. 805.
- Jones, A.D., Underwood, C.P., 2001. A thermal model for photovoltaic systems. *Sol. Energy* 70, 349–359. doi:10.1016/S0038-092X(00)00149-3
- Jordan, D.C., Wohlgemuth, J.H., Kurtz, S.R., 2012. Technology and Climate Trends in PV Module Degradation, in: *Proceedings of the 27th European Photovoltaic Solar Energy Conference and Exhibition*. Presented at the 27th European Photovoltaic Solar Energy Conference and Exhibition, Frankfurt am Main, Germany, pp. 3118–3124. doi:10.4229/27thEUPVSEC2012-4DO.5.1
- Kamali, G.A., Moradi, I., Khalili, A., 2006. Estimating solar radiation on tilted surfaces with various orientations: a study case in Karaj (Iran). *Theor. Appl. Climatol.* 84, 235–241. doi:10.1007/s00704-005-0171-y
- Karatepe, E., Boztepe, M., Çolak, M., 2007. Development of a suitable model for characterizing photovoltaic arrays with shaded solar cells. *Sol. Energy* 81, 977–992. doi:10.1016/j.solener.2006.12.001
- Khalil, S.A., Shaffie, A.M., 2013. A comparative study of total, direct and diffuse solar irradiance by using different models on horizontal and inclined surfaces for Cairo, Egypt. *Renew. Sustain. Energy Rev.* 27, 853–863. doi:10.1016/j.rser.2013.06.038
- Khan, F., Singh, S.N., Husain, M., 2010. Effect of illumination intensity on cell parameters of a silicon solar cell. *Sol. Energy Mater. Sol. Cells, PVSEC* 18 94, 1473–1476. doi:10.1016/j.solmat.2010.03.018
- Khoo, Y.S., Singh, J.P., Walsh, T.M., Aberle, A.G., 2014. Comparison of Angular Reflectance Losses Between PV Modules With Planar and Textured Glass Under Singapore Outdoor Conditions. *IEEE J. Photovolt.* 4, 362–367. doi:10.1109/JPHOTOV.2013.2284544
- Kimber, A., Mitchell, L., Nogradi, S., Wenger, H., 2006. The Effect of Soiling on Large Grid-Connected Photovoltaic Systems in California and the Southwest Region of the United States, in: *Conference Record of the 2006 IEEE 4th World Conference on Photovoltaic Energy Conversion*. Presented at the Conference Record of the 2006 IEEE 4th World Conference on Photovoltaic Energy Conversion, pp. 2391–2395. doi:10.1109/WCPEC.2006.279690
- King, D.L., 1996. Photovoltaic module and array performance characterization methods for all system operating conditions, in: *AIP Conference Proceedings*. Presented at the National renewable energy laboratory and sandia national laboratories photovoltaics program review meeting, Lakewood, CO, USA.
- King, D.L., Boyson, W.E., Kratochvill, J.A., 2004. Photovoltaic Array Performance Model (Sandia report No. SAND2004-3535). Sandia National Laboratories, Albuquerque, NM, USA.
- King, D.L., Gonzalez, S., Galbraith, G.M., Boyson, W.E., 2007. Performance Model for Grid-Connected Photovoltaic Inverters (No. SAND2007-5036). Sandia National Laboratories, Albuquerque, NM, USA.
- King, D.L., Kratochvill, J.A., Boyson, W.E., 1998. Field Experience with a New Performance Characterization Procedure for Photovoltaic Arrays, in: *Proceedings of the Second World Conference and Exhibition on Photovoltaic Solar Energy Conversion*. Presented at the Second world conference and exhibition on photovoltaic solar energy conversion, Vienna, Austria.
- Klucher, T.M., 1979. Evaluation of models to predict insolation on tilted surfaces. *Sol. Energy* 23, 111–114. doi:10.1016/0038-092X(79)90110-5
- Kokhanovsky, A., 2004. Optical properties of terrestrial clouds. *Earth-Sci. Rev.* 64, 189–241. doi:10.1016/S0012-8252(03)00042-4
- Kopp, G., Lean, J.L., 2011. A new, lower value of total solar irradiance: Evidence and climate significance. *Geophys. Res. Lett.* 38, L01706. doi:10.1029/2010GL045777
- Koronakis, P.S., 1986. On the choice of the angle of tilt for south facing solar collectors in the Athens basin area. *Sol. Energy* 36, 217–225. doi:10.1016/0038-092X(86)90137-4

BIBLIOGRAPHY

- Lárez, C., Bellabarba, C., Rincón, C., 1994. Alloy composition and temperature dependence of the fundamental absorption edge in $\text{CuGaIn}_{1-x}\text{Se}_2$. *Appl. Phys. Lett.* 65, 1650–1652. doi:10.1063/1.112944
- Lasnier, F., Gan Ang, T., 1990. Photovoltaic engineering handbook. A. Hilger, Bristol, England; New York.
- Leckner, B., 1978. The spectral distribution of solar radiation at the earth's surface—elements of a model. *Sol. Energy* 20, 143–150. doi:10.1016/0038-092X(78)90187-1
- Littmann, B., 2014. PV Plant Performance and Prediction.
- Liu, B., Jordan, R., 1961. Daily Insolation on Surfaces Tilted Towards Equator. *ASHRAE J U. S.* 10.
- Li, W., Yang, R., Wang, D., 2014. CdTe solar cell performance under high-intensity light irradiance. *Sol. Energy Mater. Sol. Cells* 123, 249–254. doi:10.1016/j.solmat.2014.01.021
- Lorenzo, E., 2003. Energy Collected and Delivered by PV Modules, in: *Handbook of Photovoltaic Science and Engineering*. John Wiley & Sons Ltd, Chichester, England, UK, pp. 905–970.
- Loutzenhiser, P.G., Manz, H., Felsmann, C., Strachan, P.A., Frank, T., Maxwell, G.M., 2007. Empirical validation of models to compute solar irradiance on inclined surfaces for building energy simulation. *Sol. Energy* 81, 254–267. doi:10.1016/j.solener.2006.03.009
- Ma, C.C.Y., Iqbal, M., 1983. Statistical comparison of models for estimating solar radiation on inclined surfaces. *Sol. Energy* 31, 313–317. doi:10.1016/0038-092X(83)90019-1
- Mailutha, J.T., Murase, H., Inoti, I.K., 1994. Knowledge Engineering-based Studies on Solar Energy Utilization in Kenya (Part II). *Agric. Mech. Asia Afr. Lat. Am.* 25, 13–16.
- Manoogian, A., Woolley, J.C., 1984. Temperature dependence of the energy gap in semiconductors. *Can. J. Phys.* 62, 285–287. doi:10.1139/p84-043
- Marion, W.F., Dobos, A.P., 2013. Rotation Angle for the Optimum Tracking of One-Axis Trackers (Research Report No. TP-6A20-58891). National Renewable Energy Laboratory, Golden, CO, USA.
- Markvart, T., 2008a. Solar cell as a heat engine: energy–entropy analysis of photovoltaic conversion. *Phys. Status Solidi A* 205, 2752–2756. doi:10.1002/pssa.200880460
- Markvart, T., 2008b. The thermodynamics of optical étendue. *J. Opt. Pure Appl. Opt.* 10, 015008. doi:10.1088/1464-4258/10/01/015008
- Markvart, T., 2010. Counting Sunrays: From Optics to the Thermodynamics of Light, in: *Physics of Nanostructured Solar Cells*. Nova Science Publishers, pp. 43–68.
- Martín, N., Chenlo, F., Mejuto, E., Soriano, F., Temprano, S., Alonso-García, M.C., 2012. Validating an angular of incidence losses model with different PV technologies and soiling conditions, in: *EU PVSEC Proceedings*. Presented at the 27th EU PVSEC, Frankfurt am Main, Germany, pp. 3436–3438. doi:10.4229/27thEUPVSEC2012-4BV.3.5
- Martín, N., Ruiz, J.M., 1999. A new method for the spectral characterisation of PV modules. *Prog. Photovolt. Res. Appl.* 7, 299–310. doi:10.1002/(SICI)1099-159X(199907/08)7:4<299::AID-PIP260>3.0.CO;2-0
- Martín, N., Ruiz, J.M., 2001. Calculation of the PV modules angular losses under field conditions by means of an analytical model. *Sol. Energy Mater. Sol. Cells* 70, 25–38. doi:10.1016/S0927-0248(00)00408-6
- Martín, N., Ruiz, J.M., 2002. A new model for PV modules angular losses under field conditions. *Int. J. Sol. Energy* 22, 19–31. doi:10.1080/01425910212852
- Martín, N., Ruiz, J.M., 2005. Annual angular reflection losses in PV modules. *Prog. Photovolt. Res. Appl.* 13, 75–84. doi:10.1002/pip.585
- Maxwell, E.L., Energy, U.S.D. of, Institute, S.E.R., 1987. A Quasi-physical Model for Converting Hourly Global Horizontal to Direct Normal Insolation. Solar Energy Research Institute.
- Meyer, E.L., Van Dyk, E., 2004. Assessing the reliability and degradation of photovoltaic module performance parameters. *IEEE Trans. Reliab.* 53, 83–92. doi:10.1109/TR.2004.824831
- Michalsky, J.J., 1988. The Astronomical Almanac's algorithm for approximate solar position (1950–2050). *Sol. Energy* 40, 227–235. doi:10.1016/0038-092X(88)90045-X
- Muneer, T., 1990. Solar radiation model for Europe. *Build. Serv. Eng. Res. Technol.* 11, 153–163. doi:10.1177/014362449001100405
- Narvarte, L., Lorenzo, E., 2008. Tracking and ground cover ratio. *Prog. Photovolt. Res. Appl.* 16, 703–714. doi:10.1002/pip.847

BIBLIOGRAPHY

- Noorian, A.M., Moradi, I., Kamali, G.A., 2008. Evaluation of 12 models to estimate hourly diffuse irradiation on inclined surfaces. *Renew. Energy* 33, 1406–1412. doi:10.1016/j.renene.2007.06.027
- Notton, G., Poggi, P., Cristofari, C., 2006. Predicting hourly solar irradiations on inclined surfaces based on the horizontal measurements: Performances of the association of well-known mathematical models. *Energy Convers. Manag.* 47, 1816–1829. doi:10.1016/j.enconman.2005.10.009
- Orgill, J.F., Hollands, K.G.T., 1977. Correlation equation for hourly diffuse radiation on a horizontal surface. *Sol. Energy* 19, 357–359. doi:10.1016/0038-092X(77)90006-8
- Patel, H., Agarwal, V., 2008. MATLAB-Based Modeling to Study the Effects of Partial Shading on PV Array Characteristics. *IEEE Trans. Energy Convers.* 23, 302–310. doi:10.1109/TEC.2007.914308
- Perez, R., Ineichen, P., Seals, R., Michalsky, J., Stewart, R., 1990. Modeling daylight availability and irradiance components from direct and global irradiance. *Sol. Energy* 44, 271–289. doi:10.1016/0038-092X(90)90055-H
- Perez, R., Seals, R., Ineichen, P., Stewart, R., Menicucci, D., 1987. A new simplified version of the perez diffuse irradiance model for tilted surfaces. *Sol. Energy* 39, 221–231. doi:10.1016/S0038-092X(87)80031-2
- Petrone, G., Spagnuolo, G., Vitelli, M., 2007. Analytical model of mismatched photovoltaic fields by means of Lambert W-function. *Sol. Energy Mater. Sol. Cells* 91, 1652–1657. doi:10.1016/j.solmat.2007.05.021
- Powalla, M., Hariskos, D., Jackson, P., Kessler, F., Paetel, S., Wischmann, W., Witte, W., Würz, R., 2011. CIGS Solar Cells with Efficiencies > 20 %: Current Status and New Developments, in: *Proceeding of the 26th European Photovoltaic Solar Energy Conference and Exhibition*. Presented at the 26th European Photovoltaic Solar Energy Conference and Exhibition, Hamburg, Germany, pp. 2416–2420.
- Priyanka, Lal, M., Singh, S.N., 2007. A new method of determination of series and shunt resistances of silicon solar cells. *Sol. Energy Mater. Sol. Cells* 91, 137–142. doi:10.1016/j.solmat.2006.07.008
- PVsyst SA, 2014a. PVsyst. PVsyst SA, Satigny, Switzerland.
- PVsyst SA, 2014b. http://files.pvsyst.com/help/pvmodule_model.htm [WWW Document]. Charact. PV Module Model Descr. URL http://files.pvsyst.com/help/pvmodule_model.htm (accessed 11.19.14).
- Rabl, A., 1986. Prediction of Annual Electricity Production By Photovoltaic Cells, in: *The Handbook of Photovoltaic Applications: Building Applications and System Design Considerations*. Fairmont Press.
- Ramaprabha, R., Mathur, B.L., 2008. Modelling and simulation of Solar PV Array under partial shaded conditions, in: *IEEE International Conference on Sustainable Energy Technologies*, 2008. ICSET 2008. Presented at the IEEE International Conference on Sustainable Energy Technologies, 2008. ICSET 2008, pp. 7–11. doi:10.1109/ICSET.2008.4746963
- Ransome, S., Sutterlueti, J., Sellner, S., 2012. PV technology differences and discrepancies in modelling between simulation programs and measurements, in: *2012 38th IEEE Photovoltaic Specialists Conference (PVSC)*. Presented at the 2012 38th IEEE Photovoltaic Specialists Conference (PVSC), pp. 003061–003066. doi:10.1109/PVSC.2012.6318228
- Reda, I., Andreas, A., 2008. Solar Position Algorithm for Solar Radiation Applications (Technical Report No. NREL/TP-560-34302). National Renewable Energy Laboratory (NREL), Golden, CO, USA.
- Regulation and Supervision Bureau, 2009. The Electricity Wiring Regulations 2007 (Revision 1).
- Reich, N.H., van Sark, W.G.J.H.M., Alsema, E.A., Lof, R.W., Schropp, R.E.I., Sinke, W.C., Turkenburg, W.C., 2009. Crystalline silicon cell performance at low light intensities. *Sol. Energy Mater. Sol. Cells* 93, 1471–1481. doi:10.1016/j.solmat.2009.03.018
- Reindl, D.T., Beckman, W.A., Duffie, J.A., 1990a. Evaluation of hourly tilted surface radiation models. *Sol. Energy* 45, 9–17. doi:10.1016/0038-092X(90)90061-G
- Reindl, D.T., Beckman, W.A., Duffie, J.A., 1990b. Diffuse fraction correlations. *Sol. Energy* 45, 1–7. doi:10.1016/0038-092X(90)90060-P
- Risser, V.V., Fuentes, M.K., 1984. Linear regression analysis of flat-plate photovoltaic system performance data, in: *5th Photovoltaic Solar Energy Conference Proceedings*. Presented at the 5th Photovoltaic Solar Energy Conference, pp. 623–627.

BIBLIOGRAPHY

- Ross, R.G., 1976. Interface design considerations for terrestrial solar cell modules, in: Photovoltaic Specialists Conference Record. Presented at the Photovoltaic Specialists Conference, Los Angeles, CA, USA, pp. 801–806.
- Rummel, S.R., McMahon, T.J., 1996. Effect of cell shunt resistance on PV module performance at reduced light levels, in: AIP Conference Proceedings. Presented at the The 13th NREL photovoltaics program review meeting, AIP Publishing, pp. 581–586. doi:10.1063/1.49388
- Sabry, M., Ghitas, A.E., 2007. Influence of Temperature on Methods for Determining Silicon Solar Cell Series Resistance. *J. Sol. Energy Eng.* 129, 331–335. doi:10.1115/1.2735350
- Sandia National Laboratories, 2014a. Sandia National Laboratories Modules.
- Sandia National Laboratories, 2014b. Sandia National Laboratories Inverters.
- Santbergen, R., 2008. Optical Absorption Factor of Solar Cells for PVT Systems (PhD thesis). Eindhoven University of Technology, Eindhoven, Netherlands.
- Schmidt, J., 2004. Light-Induced Degradation in Crystalline Silicon Solar Cells. *Solid State Phenom.* 95-96, 187–196. doi:10.4028/www.scientific.net/SSP.95-96.187
- Schott, T., 1985. Operation temperatures of PV modules, in: Proceedings of the Sixth E.C. Photovoltaic Solar Energy Conference. Presented at the E.C. photovoltaic solar energy conference, London, United Kingdom, pp. 392–396.
- Sellner, S., Sutterlueti, J., Ransome, S., Schreier, L., Allet, N., 2012a. Understanding PV module performance: Further validation of the novel loss factors model and its extension to AC arrays 3199–3204. doi:10.4229/27thEUPVSEC2012-4EO.3.5
- Sellner, S., Sutterluti, J., Schreier, L., Ransome, S., 2012b. Advanced PV module performance characterization and validation using the novel Loss Factors Model, in: 2012 38th IEEE Photovoltaic Specialists Conference (PVSC). Presented at the 2012 38th IEEE Photovoltaic Specialists Conference (PVSC), pp. 002938–002943. doi:10.1109/PVSC.2012.6318201
- Servant, J.M., 1985. Calculation of the cell temperature for photovoltaic modules from climatic data, in: Proceedings of the Ninth Biennial Congress of the International Solar Energy Society. Presented at the INTERSOL 85 - the Ninth Biennial Congress of the International Solar Energy, Pergamon Press, Montréal, Québec, Canada, p. 370.
- Siegel, D.A., Westberry, T.K., Ohlmann, J.C., 1999. Cloud Color and Ocean Radiant Heating. *J. Clim.* 12, 1101–1116. doi:10.1175/1520-0442(1999)012<1101:CCAORH>2.0.CO;2
- Singh, P., Singh, S.N., Lal, M., Husain, M., 2008. Temperature dependence of I–V characteristics and performance parameters of silicon solar cell. *Sol. Energy Mater. Sol. Cells* 92, 1611–1616. doi:10.1016/j.solmat.2008.07.010
- Skartveit, A., Olseth, J.A., 1986. Modelling slope irradiance at high latitudes. *Sol. Energy* 36, 333–344. doi:10.1016/0038-092X(86)90151-9
- Skoplaki, E., Palyvos, J.A., 2009. Operating temperature of photovoltaic modules: A survey of pertinent correlations. *Renew. Energy* 34, 23–29. doi:10.1016/j.renene.2008.04.009
- SMA Solar Technology AG, 2014. SUNNY CENTRAL 500MV / 630MV / 800MV / 1000MV / 1250MV / 1600MV [WWW Document]. URL <http://files.sma.de/dl/15986/SC500MV-1600MV-DEN114310W.pdf> (accessed 11.21.14).
- Smirnov, A., Holben, B.N., Dubovik, O., O'Neill, N.T., Eck, T.F., Westphal, D.L., Goroch, A.K., Pietras, C., Slutsker, I., 2002. Atmospheric Aerosol Optical Properties in the Persian Gulf. *J. Atmospheric Sci.* 59, 620.
- Souka, A.F., Safwat, H.H., 1966. Determination of the optimum orientations for the double-exposure, flat-plate collector and its reflectors. *Sol. Energy* 10, 170–174. doi:10.1016/0038-092X(66)90004-1
- Staebler, D.L., Wronski, C.R., 1980. Optically induced conductivity changes in discharge-produced hydrogenated amorphous silicon. *J. Appl. Phys.* 51, 3262–3268. doi:10.1063/1.328084
- Stammes, P., Acarreta, J.R., Knap, W.H., Tilstra, L.G., 2004. Earth reflectance spectra from 300-1750 nm measured by SCIAMACHY, in: Current Problems in Atmospheric Radiation. Presented at the International Radiation Symposium, Hampton, Busan, Korea, pp. 215–218.

BIBLIOGRAPHY

- Stein, J.S., Hansen, C.W., King, B.H., Sutterlueti, J., Ransome, S., 2013. Outdoor Pv Performance Evaluation of Three Different Models: Single-Diode Sapm and Loss Factor Model. (No. SAND2013-7913C). Sandia National Laboratories (SNL-NM), Albuquerque, NM (United States).
- Stein, J.S., Klise, G.T., 2009. Models Used to Assess the Performance of Photovoltaic Systems. (No. SAND2009-8258). Sandia National Laboratories.
- Steven, M.D., Unsworth, M.H., 1980. The angular distribution and interception of diffuse solar radiation below overcast skies. *Q. J. R. Meteorol. Soc.* 106, 57–61. doi:10.1002/qj.49710644705
- Sutterlueti, J., Ransome, S., Kravets, R., Schreier, L., 2011. Characterising PV Modules Under Outdoor Conditions: What's Most Important for Energy Yield, in: EU PVSEC Proceedings. Presented at the 26th European Photovoltaic Solar Energy Conference and Exhibition, Hamburg, Germany, pp. 3608–3614. doi:10.4229/26thEUPVSEC2011-4AV.2.41
- Swanson, R.M., 2009. Back side contact solar cell with doped polysilicon regions. US7633006 B1.
- Sze, S.M., Ng, K.K., 2006. Physics of Semiconductor Devices. John Wiley & Sons.
- Temps, R.C., Coulson, K.L., 1977. Solar radiation incident upon slopes of different orientations. *Sol. Energy* 19, 179–184. doi:10.1016/0038-092X(77)90056-1
- Tian, Y.Q., Davies-Colley, R.J., Gong, P., Thorrold, B.W., 2001. Estimating solar radiation on slopes of arbitrary aspect. *Agric. For. Meteorol.* 109, 67–74. doi:10.1016/S0168-1923(01)00245-3
- Tucci, M., Serenelli, L., De Iuliis, S., Izzi, M., de Cesare, G., Caputo, D., 2011. Contact Formation on aSi:H/c-Si Heterostructure Solar Cells, in: Physics and Technology of Amorphous-Crystalline Heterostructure Silicon Solar Cells. Springer.
- Tuomiranta, A., Marpu, P., Munawwar, S., Ghedira, H., 2013. Validation of thermal models for photovoltaic cells under hot desert climates, in: Energy Procedia. Presented at the ISES Solar World Congress 2013, Cancún, Mexico. doi:10.1016/j.egypro.2014.10.017
- Utrillas, M.P., Martinez-Lozano, J.A., 1994. Performance evaluation of several versions of the Perez tilted diffuse irradiance model. *Sol. Energy* 53, 155–162. doi:10.1016/0038-092X(94)90476-6
- Van Dyk, E.E., Meyer, E.L., 2004. Analysis of the effect of parasitic resistances on the performance of photovoltaic modules. *Renew. Energy* 29, 333–344. doi:10.1016/S0960-1481(03)00250-7
- Virtuani, A., Lotter, E., Powalla, M., 2003. Performance of Cu(In,Ga)Se₂ solar cells under low irradiance. Thin Solid Films, Proceedings of Symposium B, Thin Film Chalcogenide Photovoltaic Materials, E-MRS Spring Meeting 431–432, 443–447. doi:10.1016/S0040-6090(03)00184-6
- Weiser, G., Mell, H., 1989. Temperature dependence of the optical absorption edge in a-Si:H. *J. Non-Cryst. Solids*, Proceedings of the Thirteenth International Conference on Amorphous and Liquid Semiconductors 114, Part 1, 298–300. doi:10.1016/0022-3093(89)90143-9
- Willmott, C.J., 1982. On the climatic optimization of the tilt and azimuth of flat-plate solar collectors. *Sol. Energy* 28, 205–216. doi:10.1016/0038-092X(82)90159-1
- Wilson, A., Ross, R.G., 1983. Angle of Incidence Effects on Module Power Performance and Energy, in: Progress Report 21 and Proceedings of the 21 St Project Integration Meeting. Presented at the 21 st Project Integration Meeting, JPL Publication, Pasadena, California, USA, pp. 423–426.
- Wu, C.-Y., Chen, J.-F., 1982. Temperature coefficients of the open-circuit voltage of p-n junction solar cells. *J. Appl. Phys.* 53, 3852–3858. doi:10.1063/1.331129
- Würfel, P., 2005. Physics of Solar Cells: From Principles to New Concepts. Wiley.
- Yang, D., Dong, Z., Nobre, A., Khoo, Y.S., Jirutitijaroen, P., Walsh, W.M., 2013. Evaluation of transposition and decomposition models for converting global solar irradiance from tilted surface to horizontal in tropical regions. *Sol. Energy* 97, 369–387. doi:10.1016/j.solener.2013.08.033